The Novel Hydroxylated Tetraether Index RI-OH' as a Sea Surface Temperature Proxy for the 160–45 ka BP Period Off the Iberian Margin

Nina Davtian, Edouard Bard, Sophie Darfeuil, Guillemette Ménot, Frauke Rostek

Paleoceanography and Paleoclimatology

RESEARCH ARTICLE
10.1029/2020PA004077

Key Points:

- RI-OH′ not only responds to Dansgaard-Oeschger and Heinrich events but also better resembles $U^{K'}_{37}$ than TEX_{86}
- RI-OH′ gives realistic sea surface temperatures and latitudinal gradients consistent with those from independent paleothermometers
- Relationships with Greenland temperatures further support RI-OH′-based paleothermometry

Supporting Information:

- Supporting Information S1
- Data Set S1
- Data Set S2
- Data Set S3
- Data Set S4

Correspondence to:
N. Davtian,
Nina.Davtian@uab.cat

Citation:
Davtian, N., Bard, E., Darfeuil, S., Ménot, G., & Rostek, F. (2021). The novel hydroxylated tetraether index RI-OH′ as a sea surface temperature proxy for the 160-45 ka BP period off the Iberian Margin. *Paleoceanography and Paleoclimatology*, *36*, e2020PA004077. https://doi.org/10.1029/2020PA004077

Received 31 JUL 2020
Accepted 17 FEB 2021

The Novel Hydroxylated Tetraether Index RI-OH′ as a Sea Surface Temperature Proxy for the 160-45 ka BP Period Off the Iberian Margin

Nina Davtian[1,2], Edouard Bard[1], Sophie Darfeuil[1,3], Guillemette Ménot[4], and Frauke Rostek[1]

[1]CEREGE, Aix-Marseille University, CNRS, IRD, INRAE, Coll France, Aix-en-Provence, France, [2]Now at Institut de Ciència i Tecnologia Ambientals (ICTA-UAB), Universitat Autònoma de Barcelona, Bellaterra, Spain, [3]Now at Univ Grenoble Alpes, CNRS, IRD, Grenoble Institute of Engineering and Management Univ Grenoble Alpes, IGE, Grenoble, France, [4]Univ Lyon, ENS de Lyon, Université Lyon 1, CNRS, UMR 5276 LGL-TPE, Lyon, France

Abstract RI-OH′ and RI-OH (ring index of hydroxylated tetraethers) are two novel organic paleothermometers which could either complement or replace more established paleothermometric proxies, such as $U^{K'}_{37}$ (C_{37} ketone unsaturation ratio) and TEX_{86} (TetraEther indeX of tetraethers consisting of 86 carbon atoms). Despite a few promising attempts, the paleothermometric potential of RI-OH′ and RI-OH is not fully constrained. Here we present new high-resolution temperature records over the 160-45 ka BP (before present = year 1950 CE) period using four organic proxies (RI-OH′, RI-OH, TEX_{86}, and $U^{K'}_{37}$) from three deep sea sediment cores located in a north-south transect along the Iberian Margin. We analyzed all organic proxies from a single set of lipid extracts to optimize proxy-proxy comparisons and phase relationship studies. RI-OH′ responds to Dansgaard-Oeschger and Heinrich events, better resembles $U^{K'}_{37}$ than TEX_{86}, and better records the influence of (sub)polar waters during Heinrich events than does RI-OH. While RI-OH′ gives realistic sea surface temperatures and latitudinal gradients coherent with those from independent paleothermometers, a more extensive RI-OH′-temperature calibration for the North Atlantic is clearly needed. However, the absence of a significant warm bias in RI-OH′-based temperatures compared to a shallow sea site suggests that endemic, deep-dwelling archeal communities affect TEX_{86} but not RI-OH′ in the Iberian Margin. TEX_{86} leads RI-OH′ and $U^{K'}_{37}$ during four Heinrich-like events, potentially due to background fluxes from deep waters for nonhydroxylated tetraethers summed with primary productivity dependent fluxes from surface waters for all investigated lipid classes. Relationships with Greenland temperatures further support RI-OH′-based paleothermometry.

1. Introduction

Sea surface temperature (SST) records from the southern Iberian Margin (Figure 1a) are typically cited as reference signals for North Atlantic climate variations (Bard, Arnold, Maurice, et al., 1987; Bard et al., 2000; Cayre et al., 1999; Martrat et al., 2007; Pailler & Bard, 2002; Shackleton et al., 2000). Iberian Margin SST records not only have a clear glacial-interglacial variability, but they also show characteristic Heinrich (Bond & Lotti, 1995; Bond et al., 1992; Heinrich, 1988) and Dansgaard-Oeschger events (Dansgaard et al., 1993). Sedimentary archives from the Iberian Margin are thus particularly useful to validate SST proxies and to study climate system dynamics between high and middle latitudes in the Northern Hemisphere (e.g., Bard, Arnold, Maurice, et al., 1987; Bard et al., 2000; Cayre et al., 1999; Darfeuil et al., 2016; Datema et al., 2019; de Abreu et al., 2003; Martrat et al., 2007; Pailler & Bard, 2002; Voelker & de Abreu, 2011).

Several existing SST proxies are based on organic biomarkers. The first organic SST proxy is $U^{K'}_{37}$ (C_{37} ketone unsaturation ratio; Prahl & Wakeham, 1987), which is based on di-unsaturated ($C_{37:2}$) and tri-unsaturated ($C_{37:3}$) alkenones produced by haptophyte algae (Marlowe et al., 1984; Volkman et al., 1980, 1995). The first validation of alkenones as SST proxies in sedimentary archives dates from several decades ago (Brassell et al., 1986) and subsequent core top and culture studies have confirmed that $U^{K'}_{37}$ increases with increasing SST (e.g., Conte et al., 2006; Müller et al., 1998; Prahl & Wakeham, 1987; Prahl et al., 1988; Tierney & Tingley, 2018).

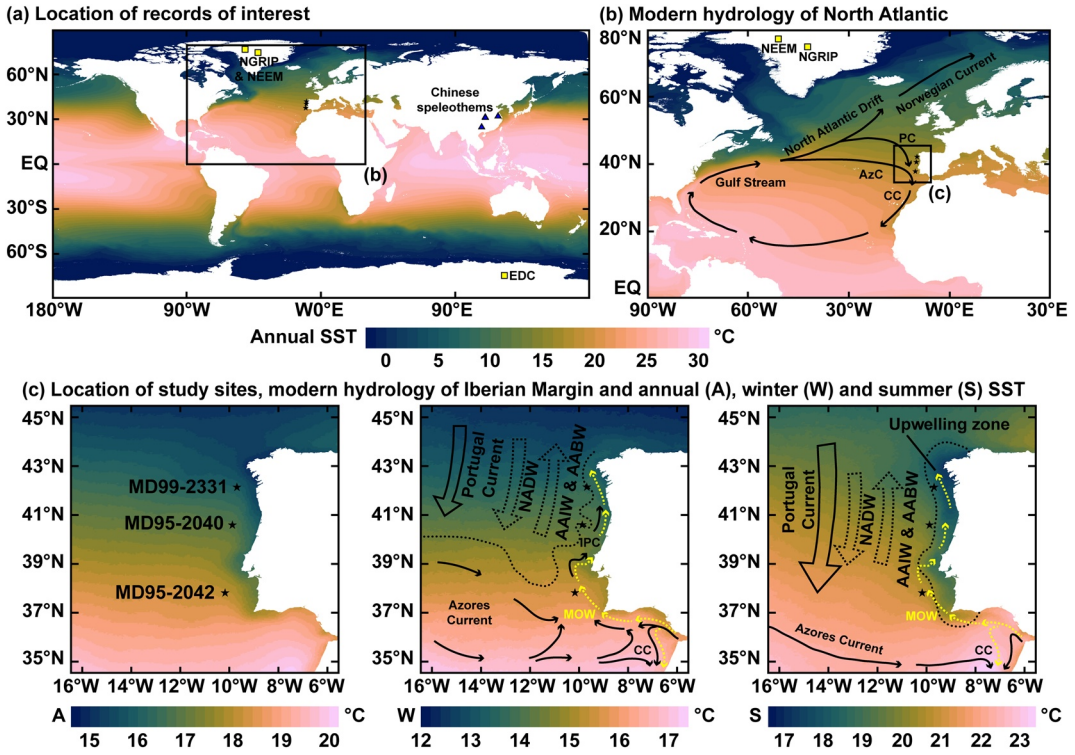

Figure 1. Location and modern hydrology of the Iberian Margin. (a) Location of records mentioned in the text. The located Chinese speleothem records are those compiled by Cheng et al. (2016). NGRIP, North Greenland Ice Core Project (NGRIP members, 2004); NEEM, North Greenland Eemian Ice Drilling (NEEM community members, 2013), and EDC, European Project for Ice Coring in Antarctica Dome C (EPICA Community Members, 2004). (b) Close-up of the North Atlantic from (a). (c) Close-up of the Iberian Margin from (b) with study site names. Solid arrows represent surface currents whereas dashed arrows represent deep currents. PC, Portugal Current; AzC, Azores Current; CC; Canary Current; IPC; Iberian Poleward Current; MOW, Mediterranean Outflow Waters; NADW; North Atlantic Deep Waters; AAIW, Antarctic Intermediate Waters; and AABW, Antarctic Deep Waters. The colored sea surface temperature (SST) gradients represent Pathfinder SST V5 climatology for the 1982–2010 period (4 km resolution; Casey et al., 2010). These data were provided by the Group for High Resolution Sea Surface Temperature and the US National Oceanographic Data Center. This project was supported in part by a grant from the National Oceanic and Atmospheric Administration Climate Data Record Program for satellites. Perceptually uniform color maps are used in this study to prevent visual distortion of the data (Crameri, 2018a, 2018b).

Another organic SST proxy is TEX_{86} (TetraEther indeX of tetraethers consisting of 86 carbon atoms; Schouten et al., 2002), which is based on nonhydroxylated isoprenoid glycerol dialkyl glycerol tetraethers (iGDGTs; Figure S1) produced by *Thaumarchaeota*—formerly Group I *Crenarchaeota* (Schouten, Hopmans, & Sinninghe Damsté, 2013, and references therein; Sinninghe Damsté et al., 2002). *Thaumarchaeota* is a major group of ammonia oxidizing archaea (Herndl et al., 2005; Ingalls et al., 2006; Karner et al., 2001; Könneke et al., 2005; Wuchter et al., 2006) which substantially if not majoritarily contributes to iGDGT and TEX_{86} signals in open oceans (Besseling et al., 2020; Zeng et al., 2019). Core top and mesocosm studies have shown that TEX_{86} increases with increasing SST (e.g., Kim et al., 2008, 2010; Schouten et al., 2002, 2007; Tierney & Tingley, 2015; Wuchter et al., 2004) and the first applications of TEX_{86} as an SST proxy date from more than a decade ago (Huguet, Kim, et al., 2006; Schouten et al., 2003).

Two examples of novel organic SST proxies are RI-OH and RI-OH′ (ring index of hydroxylated tetraethers; Lü et al., 2015), which are based on hydroxylated isoprenoid glycerol dialkyl glycerol tetraethers (OH-GDGTs; Figure S1) produced by ammonia oxidizing Group I.1a *Thaumarchaeota* (Elling et al., 2014, 2015, 2017; Sinninghe Damsté et al., 2012; Liu et al., 2012; Sollai et al., 2019; Xu et al., 2020). In temperate and polar oceans, the only two global core top studies to date have shown that RI-OH and RI-OH′ increase with increasing SST (Fietz et al., 2020; Lü et al., 2015). Only a few recent studies have used RI-OH (Davtian

et al., 2019; de Bar et al., 2019) and RI-OH′ (Allaart et al., 2020; Fietz et al., 2020; Kremer et al., 2018; Vorrath et al., 2020; J. Wu et al., 2020) as SST proxies in sedimentary archives.

Despite their paleothermometric potential, $U^{K'}_{37}$, TEX_{86}, RI-OH, and RI-OH′ have their own shortcomings, as do other SST proxies based on isotopes and on microfossil assemblages. Light and nutrient availability (Epstein et al., 1998; Prahl et al., 2003; Sikes et al., 2005; Versteegh et al., 2001), lateral transport (Benthien & Müller, 2000; Kim et al., 2009; Mollenhauer et al, 2006, 2007; Rühlemann & Butzin, 2006), and differential degradation (Rontani et al., 2013, and references therein) are examples of biases for $U^{K'}_{37}$. Terrigenous inputs (Weijers et al., 2006), methanotrophic interferences (Blaga et al., 2009; Weijers et al., 2011; Zhang et al., 2011), and depth dependent *Thaumarchaeota* communities and iGDGT distributions (e.g., Basse et al., 2014; Besseling et al., 2019; Kim et al., 2015, 2016) are examples of biases for TEX_{86}. Seasonal maximal producer abundance or biomarker production can bias $U^{K'}_{37}$ and TEX_{86} (e.g., Ceccopieri et al., 2018; Galand et al., 2010; Herfort et al., 2006, 2007; Leider et al., 2010; Lü et al., 2014; Pitcher et al., 2011; Prahl et al., 1993, 2001, 2010; Sicre et al., 1999; Sikes et al., 1997; Zhang et al., 2013). Biomarker production may also occur below surface waters, especially for GDGTs as their producers do not need light to thrive (e.g., Chen et al., 2014, 2016; Huguet et al., 2007; Hurley et al., 2018; Lee et al., 2008; Park et al., 2018, 2019; Prahl et al., 2001, 2005; Richey & Tierney, 2016; Ternois et al., 1997). RI-OH and RI-OH′ seem to share several biases with TEX_{86} (Chen et al., 2020; Kang et al., 2017; Lü et al., 2015, 2019; Wei et al., 2020; Yang et al., 2019; Zhu et al., 2016; see also Fietz et al., 2020 for a review). However, only a few *Thaumarchaeota* groups produce both iGDGTs and OH-GDGTs (Elling et al., 2017; Sinninghe Damsté et al., 2012) and both archeal GDGT groups can generate drastically different SST records from a single site (Davtian et al., 2019; Vorrath et al., 2020; see also Fietz et al., 2020). It is thus useful to conjointly test $U^{K'}_{37}$, TEX_{86}, RI-OH, and RI-OH′ as SST proxies under several contrasting environmental contexts.

In this study, we present new high-resolution temperature records over the 160–45 ka BP (before present = year 1950 CE) period using RI-OH′, RI-OH, TEX_{86}, and $U^{K'}_{37}$ from three deep sea sediment cores located in a north-south transect along the Iberian Margin (Figure 1). We first assess the novel RI-OH′ and RI-OH indices as SST proxies by correlating them with $U^{K'}_{37}$ and TEX_{86} which are more established SST proxies. We also assess OH-GDGT-based SSTs by comparing them with alkenone-based and iGDGT-based SSTs as well as SST latitudinal gradients. Then, we perform phase relationship analyses and comparisons with inorganic proxies such as the isotopic composition of oxygen ($\delta^{18}O$) of planktic foraminifers to further validate the novel RI-OH′ and RI-OH paleothermometers, especially at the millennial scale.

The Iberian Margin is located in an open ocean setting with limited terrigenous inputs, high sedimentation rates, and successful $U^{K'}_{37}$ and TEX_{86} paleothermometries (Bard et al., 2000; Darfeuil et al., 2016; Martrat et al., 2007; Pailler & Bard, 2002). The Iberian Margin thus constitutes a much more favorable sedimentary setting to validate the novel RI-OH′ and RI-OH paleothermometers than the Gulf of Lions (Davtian et al., 2019). Contrary to Davtian et al. (2019) and similarly to other multiproxy studies (e.g., Fietz et al., 2013, 2016, 2020; de Bar et al., 2018, 2019; Jonas et al., 2017; Lattaud et al., 2018; Lopes dos Santos et al., 2013; Smith et al., 2020), we studied all organic proxies using a single set of lipid extracts to facilitate comparisons between novel and established paleothermometers. The deep sea study sites also offer an opportunity to assess whether, in the Iberian Margin, Mediterranean deepwater archeal communities bias RI-OH′ and RI-OH to the same extent as TEX_{86}, a bias that is likely insignificant at the shallow sea study site of Davtian et al. (2019).

2. Stratigraphic Sequences as Complements to Modern Samples for Proxy Validation

In theory, it would be more appropriate to fully validate the proxy calibration using culture experiments or modern sediments before applying the proxy in stratigraphic sequences. In practice, such a scenario rarely occurs and both calibration and stratigraphic studies are performed in parallel. This has been the case for the TEX_{86} SST proxy with core top calibrations (e.g., Kim et al., 2008, 2010; Schouten et al., 2002; Tierney & Tingley, 2015), mesocosm experiments (Schouten et al., 2007; Wuchter et al., 2004), and stratigraphic studies (e.g., Castañeda et al., 2010; Darfeuil et al., 2016; Hollis et al., 2019, and references therein; Huguet, Kim, et al., 2006; Schouten et al., 2003; Seki et al., 2009).

Furthermore, the history of the fields of paleoclimatology and paleoceanography includes many examples for which geochemical proxies were first or mainly studied in a stratigraphic context, before reaching a better understanding with a proper calibration of observed variations versus the climatic parameter of interest. This has been the case for $\delta^{18}O$ variations measured in foraminifera from deep sea cores (e.g., Emiliani, 1957, 1966) as it took many years to realize that these stratigraphic variations were largely due to changes in the volume of continental ice sheets and that the SST component was much smaller than initially thought (e.g., Shackleton, 1967).

A second prominent example is the first study using alkenones as a paleothermometer. It was based on the direct comparison of $\delta^{18}O$ in foraminifera with alkenone unsaturation measured in a deep sea core (Brassell et al., 1986) which complemented very preliminary and scarce comparisons between temperature or latitude and alkenone unsaturation measured in modern samples. The seminal study by Brassell et al. (1986) then motivated subsequent calibration studies (e.g., Prahl & Wakeham, 1987; Prahl et al., 1988).

For decades since the 1970s, the $\delta^{18}O$ variations measured in Greenland ice cores were shown in their stratigraphic context (e.g., Dansgaard et al., 1993; Grootes et al., 1993). It was realized only in the mid-1990s that early calibrations based on $\delta^{18}O$ in modern precipitation were leading to serious under-estimation of the glacial cooling, as implied by the temperature profiles directly measured in the boreholes (Cuffey et al., 1995; Johnsen et al., 1995).

These three examples of now recognized paleothermometers illustrate that proxy development and validation not only rely on modern samples, but also on stratigraphic sequences, notably the direct comparison of novel and established proxies in the same archives. These studies are key to foster calibration studies by other research groups.

3. Study Area

The Iberian Margin is presently under the influence of the North Atlantic subtropical gyre via two branches, the Portugal Current and the Azores Current (Figure 1b; Martins et al., 2002; Pérez et al., 2001). The Eastern North Atlantic Central Waters bathe the surface and reach a water depth of roughly 500–600 m (Fiúza et al., 1998; Jenkins et al., 2015; Kim et al., 2016). The Iberian Margin is part of the Canary Current upwelling ecosystem, with higher primary productivity in late spring/summer (late May to late September/early October) associated with colder temperatures along the coast (Figure 1c; Arístegui et al., 2009; Fiúza et al., 1982, 1998; Mazé et al., 1997; Navarro & Ruiz, 2006; Relvas et al., 2007; Sánchez & Relvas, 2003). In winter, the Iberian Poleward Current flows along the coast from the eastern branch of the Azores Current (Figure 1c; Haynes & Barton, 1990; Peliz et al., 2003, 2005).

Beneath the water masses affected by seasonal contrasts, the Antarctic Intermediate Waters mixed with the Mediterranean Outflow Waters flow poleward roughly between 500–600 and 1,500 m water depth (Figure 1c; Ambar, 1983; Ambar et al., 2002; Cabeçadas et al., 2002, 2003, 2010; Fiúza et al., 1998; Jenkins et al., 2015; Kim et al., 2016; Louarn & Morin, 2011; van Aken, 2000b). The Mediterranean Outflow Waters are saltier and warmer than the surrounding Atlantic water masses (Ambar, 1983; Ambar et al., 2002; Baringer & Price, 1997; Fiúza et al., 1998; Kim et al., 2016; Kinder & Parrilla, 1987; Mazé et al., 1997; van Aken, 2000b). Between 1,500 and 3,500 m water depth, the North Atlantic Deep Waters flow southward (Figure 1c; Fiúza et al., 1998; Kim et al., 2016; van Aken, 2000a) while the underlying Antarctic Bottom Waters flow poleward through Discovery Gap (Figure 1c; Jenkins et al., 2015; Saunders, 1987).

During the last glacial cycle, the surface hydrology was generally similar to the modern one, with a stronger summer upwelling (e.g., Voelker & de Abreu, 2011, and references therein; Voelker et al., 2009). However, during Heinrich events, the Polar Front reached the southern Iberian Margin (Bard, Arnold, Maurice, et al., 1987; Eynaud et al., 2009), leading to a potential cessation of the upwelling (Ausín et al., 2020; Incarbona et al., 2010; Pailler & Bard, 2002) and hydrological conditions similar to modern winter ones (Eynaud et al., 2009).

Several deepwater masses existing today were also present during the last glacial cycle, but occupied different water depths. During cold periods such as the Last Glacial Maximum and Heinrich events, the North Atlantic Deep Waters reached up to 2,000 m water depth only whereas the underlying Antarctic waters

occupied a larger portion of the water column (Lynch-Stieglitz, 2017, and references therein; Lynch-Stieglitz et al., 2007; Rahmstorf, 2002). The Mediterranean Outflow Waters were also present during the last glacial cycle, but at deeper water depths, between 1,600 and 2,200 m, given their higher density (Kaboth et al., 2016; Llave et al., 2006; Schönfeld & Zahn, 2000; Voelker et al., 2006; Zahn et al., 1987). The Antarctic Intermediate Waters reached the Gulf of Cadiz during Heinrich events and may have reached the Iberian Margin as well during these events (Dubois-Dauphin et al., 2016; Montero-Serrano et al., 2011).

4. Materials and Methods

4.1. Sediment Cores

Cores MD99-2331 (42°09′N, 9°41′W, 2,120 m water depth), MD95-2040 (40°35′N, 9°52′W, 2,465 m water depth), and MD95-2042 (37°45′N, 10°10′W, 3,146 m water depth) were retrieved from the distal part of the Iberian Margin continental talus during the IMAGES I (1995; Bassinot & Labeyrie, 1996) and V (1999; Labeyrie, 1999) cruises of R/V Marion Dufresne using a Calypso corer. The three deep sea sediment cores mainly consist in calcareous silty clay and follow a north-south transect (Figure 1c), directly below the pathways of the Iberian Poleward Current in winter (Peliz et al., 2005) and of the northern branch of the Mediterranean Outflow Waters (Mazé et al., 1997). During summer, the three study sites are at the edge of the upwelling area where they are fed by upwelling filaments (Figure 1c; Fiúza et al., 1982). Cores MD99-2331 and MD95-2040 are located roughly 100 km away from the modern coastline whereas core MD95-2042 is located roughly 150 km away from the modern coastline.

Cores MD99-2331, MD95-2040, and MD95-2042 are 3,720-cm, 3,840-cm, and 3,140-cm long, respectively. The three sediment cores cover at least the last 160 kyrs, and thus comprise the last interglacial period and the last glacial cycle. In this study, we will focus on the 160-45 ka BP period as well as the 1-0 ka BP period for proxy validation.

4.2. Age Model

We tuned the new Iberian Margin records covering the 160-45 ka BP period to the raw composite Chinese speleothem $\delta^{18}O$ record provided by Cheng et al. (2016)—herein the SpeleoAge timescale (Figures S2a–S2c and S3b–S3e, Table S1) following Darfeuil et al. (2016). For cores MD95-2040 and MD95-2042, we tuned the calcium carbonate content derived from X-ray fluorescence (XRF-%$CaCO_3$) records to the reference record. Calcium XRF measurements and conversions into XRF-%$CaCO_3$ with measured %$CaCO_3$ (Pailler & Bard, 2002; Thomson et al., 1999) are described in Texts S1 and S3 of Darfeuil et al. (2016). For core MD99-2331, we tuned the %$CaCO_3$ record (Gouzy et al., 2004) to the core MD95-2042 XRF-%$CaCO_3$ record on SpeleoAge. We manually tuned the records with the QAnalySeries software version 1.4.2 (Kotov & Pälike, 2018) that reimplements the major functionality of the AnalySeries software developed by Paillard et al. (1996). In addition to the motivation provided in Text S2 of Darfeuil et al. (2016), the generally synchronous abrupt $\delta^{18}O$ transitions within dating uncertainties between the Chinese speleothem record by Cheng et al. (2016) and the NALPS19 speleothem record from the northern rim of the Alps by Moseley et al. (2020) support our synchronization.

We also used updated Greenland and Antarctic ice core chronologies with the year 1950 CE as the reference datum for comparison with Iberian Margin records (Figures S2d and S3e–S3g, Table S2). We first synchronized the 120–60 ka BP period on the SpeleoAge timescale. For the portion after 60 ka BP, we used the Antarctic Ice Core Chronology 2012 (AICC2012) × 1.0063 timescale (linear scaling after Buizert et al., 2015 for alignment with the U/Th dated Chinese speleothem records by Cheng et al., 2016). For the portion before 120 ka BP, we used the AICC2012 timescale (Bazin et al., 2013; Veres et al., 2013). After synchronizing the North Greenland Ice Core Project (NGRIP) $\delta^{18}O$ record (NGRIP members, 2004) on the SpeleoAge timescale, we established a transfer function from AICC2012 to SpeleoAge for the 120-60 ka BP period (Figure S2d). Our transfer function confirms that the linear scalings of AICC2012 (Bazin et al., 2013; Veres et al., 2013) and Greenland Ice Core Chronology $05_{modelext}$ (Wolff et al., 2010) timescales by 1.0063 proposed by Buizert et al. (2015) are not applicable for the 120-60 ka BP period.

4.3. Sample Preparation and Biomarker Analysis

In this study, we used 149, 90, and 338 sediment samples from cores MD99-2331, MD95-2040, and MD95-2042, respectively. We took one sediment sample every 10 cm from cores MD99-2331 and MD95-2040 and one sediment sample every 5 cm from core MD95-2042. The sampling resolutions correspond to averaged temporal resolutions of roughly 830, 1,300, and 360 years over the 160-45 ka BP period for cores MD99-2331, MD95-2040, and MD95-2042, respectively. We then freeze dried the sediment samples before grinding and homogenization.

We extracted 2 g of each dried sediment sample with dichloromethane (DCM):methanol (9:1, v:v) using an accelerated solvent extractor ASE 200 (Dionex) at 120°C and 80 bars (8×10^6 Pa) at CEREGE. Before extraction, we added known amounts of ethyl-triacontanoate (C_{32}) and C_{46} glycerol trialkyl glycerol tetraether (C_{46}-GTGT) as internal standards. Thereafter, we subdivided the lipid extracts into two identical aliquots for alkenone analysis and for subsequent purification before GDGT analysis.

We analyzed alkenones with a Thermo Scientific Trace gas chromatograph equipped with a flame ionization detector installed at CEREGE, using analytical conditions similar to those described by Sonzogni et al. (1997). We then manually integrated alkenone peaks. We determined summed di-unsaturated and tri-unsaturated C_{37} alkenone concentrations in μg/g of dry weight sediment by relating chromatogram peak areas to the concentration of the internal standard C_{32}, assuming the same response factor for analytes as for the internal standard.

Prior to GDGT analysis, we operated a Gilson GX-271 ASPEC™ system with the TRILUTION™ LH software and used Al_2O_3 columns to elute apolar and polar fractions with 3.5 mL of hexane:DCM (1:1, v:v) and 5 mL of methanol:DCM (1:1, v:v), respectively (Sanchi et al., 2013). We analyzed the polar fractions with an Agilent 1260 Infinity high performance liquid chromatograph coupled to an Agilent 6120 single quadrupole mass spectrometer installed at CEREGE, following Hopmans et al. (2016) and Davtian et al. (2018, 2019) with two additional modifications: nebulizer pressure, 60 psi and dwell time, 97 ms. We then extracted the mass/charge (m/z) 743.7, 1,022.0, 1,036.0, 1,050.0, 1,292.3, 1,296.3, 1,298.3, 1,300.3, and 1,302.4 scans for manual GDGT peak integration. Contrary to Darfeuil et al. (2016), we used an analytical method with improved GDGT isomer separation (Hopmans et al., 2016) and mass accuracy for GDGT analyses (Davtian et al., 2018) as well as possible OH-GDGT quantification. Indeed, Hopmans et al. (2016) and Elling et al. (2019) found small changes in TEX_{86} values due to improved GDGT isomer separation. We determined individual GDGT concentrations by relating chromatogram peak areas to the concentration of the internal standard C_{46}-GTGT (Huguet, Hopmans, et al., 2006). During running time, we regularly determined the relative response factor between the synthetic internal standard (C_{46}-GTGT) and natural GDGTs (GDGT-0) to correct the calculated individual GDGT concentrations, given in μg/g of dry weight sediment (Huguet, Hopmans, et al., 2006).

We identified and integrated OH-GDGT peaks as described by Davtian et al. (2019) and also integrated the same peaks in the m/z 1,318.3, 1,316.3, and 1,314.3 scans. We confirm that the late eluting peaks identified by Davtian et al. (2019) in the m/z 1,300.3, 1,298.3, and 1,296.3 scans correspond to abundant in-source fragmentation products of OH-GDGTs (e.g., Liu et al., 2012). We thus quantified OH-GDGTs as $[M + H–18]^+$ ions rather than as $[M+H]^+$ ions (protonated molecular ions) to calculate RI-OH and RI-OH′ values.

4.4. Alkenone-Based and GDGT-Based Proxies and Temperature Estimates

We calculated $U^{K'}{}_{37}$ (Equation 1; Prahl & Wakeham, 1987), RI-OH (Equation 2; Lü et al., 2015), RI-OH′ (Equation 3; Lü et al., 2015), and TEX_{86} values (Equation 4; Schouten et al., 2002). In Equations 1–4, $C_{37:X}$ is the C_{37} alkenone with X unsaturations, OH-GDGT-X is the OH-GDGT with X pentacycles, and GDGT-X is the iGDGT with X pentacycles:

$$U_{37}^{K'} = \frac{C_{37:2}}{C_{37:2} + C_{37:3}} \left(\text{range between 0 and 1}\right), \tag{1}$$

$$\text{RI} - \text{OH} = \frac{\text{OH} - \text{GDGT} - 1 + 2 \times \text{OH} - \text{GDGT} - 2}{\text{OH} - \text{GDGT} - 1 + \text{OH} - \text{GDGT} - 2} \left(\text{range between 1 and 2}\right), \tag{2}$$

$$\mathrm{RI-OH'} = \frac{\mathrm{OH-GDGT-1} + 2 \times \mathrm{OH-GDGT-2}}{\mathrm{OH-GDGT-0} + \mathrm{OH-GDGT-1} + \mathrm{OH-GDGT-2}} \left(\text{range between 0 and 2}\right), \quad (3)$$

$$\mathrm{TEX_{86}} = \frac{\mathrm{GDGT-2} + \mathrm{GDGT-3} + \text{Crenarchaeol isomer}}{\mathrm{GDGT-1} + \mathrm{GDGT-2} + \mathrm{GDGT-3} + \text{Crenarchaeol isomer}} \left(\text{range between 0 and 1}\right). \quad (4)$$

For biomarker-based SST estimates, we used the linear global calibration by Conte et al. (2006) for $U^{K'}_{37}$ (Equation 5), the global calibration by Lü et al. (2015) for RI-OH (Equation 6), the global calibration by Fietz et al. (2020) for RI-OH′ (Equation 7), and the regional paleocalibration by Darfeuil et al. (2016) for TEX_{86}^{H} (Equation 8), with $TEX_{86}^{H} = \log(TEX_{86})$ as defined by Kim et al. (2010):

$$\mathrm{SST} = 29.876 \times U_{37}^{K'} - 1.334 \left(R^2 = 0.97, n = 592, \text{standard deviation of residuals} = 1.1\,^{\circ}\mathrm{C}\right), \quad (5)$$

$$\mathrm{SST} = \frac{\mathrm{RI-OH} - 1.11}{0.018} \left(R^2 = 0.74, n = 107, p < 0.01, \text{standard deviation of residuals} = 6\,^{\circ}\mathrm{C}\right), \quad (6)$$

$$\mathrm{SST} = \frac{\mathrm{RI-OH'} + 0.029}{0.0422} \left(R^2 = 0.76, n = 167, p < 0.01, \text{standard deviation of residuals} = 6\,^{\circ}\mathrm{C}\right), \quad (7)$$

$$\mathrm{SST} = 68.4 \times \mathrm{TEX_{86}^{H}} + 33.0 \left(R^2 = 0.79, n = 400, \text{standard deviation of residuals} = 2.5\,^{\circ}\mathrm{C}\right). \quad (8)$$

For comparison purposes, we also used for $U^{K'}_{37}$-SST estimates the Bayesian calibration by Tierney and Tingley (2018), BAYSPLINE, with a prior standard deviation (SD) set to 10°C. The 1σ uncertainty in BAYSPLINE $U^{K'}_{37}$-SSTs for temperate and polar oceans is 1.4°C (Tierney & Tingley, 2018). For comparison with TEX_{86}^{H}-SST estimates, we used for TEX_{86}-SST estimates the Bayesian, spatially varying calibration by Tierney and Tingley (2014, 2015), BAYSPAR, with a prior SD set to 6°C. The 1σ uncertainty in BAYSPAR TEX_{86}-SSTs for the Iberian Margin is 2.7°C (Tierney & Tingley, 2014, 2015). We use Bayesian calibrations for $U^{K'}_{37}$ and TEX_{86} to assess the validity of the non-Bayesian calibrations by Conte et al. (2006) for $U^{K'}_{37}$ and by Darfeuil et al. (2016) for TEX_{86}^{H} in the Iberian Margin.

We selected the homogenized core catcher sample from core MD95-2042 as an in-house standard sediment to check the absence of instrumental drift. For alkenones, the SD of 40 replicates was 0.01 (0.26°C) for $U^{K'}_{37}$, while the uncertainty in total C_{37} alkenone concentrations was 15%. Our SDs are more precise than the repeatability of 1.6°C in $U^{K'}_{37}$-SSTs and of 24% in total C_{37} alkenone concentrations obtained from the international alkenone intercomparison (Rosell-Melé et al., 2001). For GDGTs, the SD of 17 replicate analyses of a single lipid extract was 0.008 (0.5°C) for RI-OH, 0.007 (0.2°C) for RI-OH′, and 0.003 (0.1°C) for TEX_{86}, while the uncertainty in total iGDGT and total OH-GDGT concentrations was 4% and 3%, respectively. Our SDs in GDGT-based SSTs are either below or within the repeatability range of TEX_{86}–SSTs (0.4–0.9°C) obtained from the latest international GDGT intercomparison (Schouten, Hopmans, Rosell-Melé, et al., 2013). We will use the SD and percentage values obtained on the in-house standard sediment as 1σ analytical uncertainties.

4.5. Correlation Tests for Serially Correlated Data and Phase Relationship Analyses

We estimated the significance of correlations between serially correlated data following the same approach as Davtian et al. (2019). In short, we used the "surrogateCor" function of the astrochron *R* package (Meyers, 2014) to compute 10,000 Monte Carlo simulations using phase-randomized surrogates (Baddouh et al., 2016; Ebisuzaki, 1997). We considered that correlations were significant if $p < 0.05$.

For phase relationship analyses, we first resampled the relevant records every 10 years with the "linterp" function of the astrochron *R* package (Meyers, 2014). We then centered the resampled records and extracted their millennial variability using a fourth-order Butterworth band-pass filter (500–10,000-years window). We applied the band-pass filter with the "butterworth.wge" function of the tswge *R* package

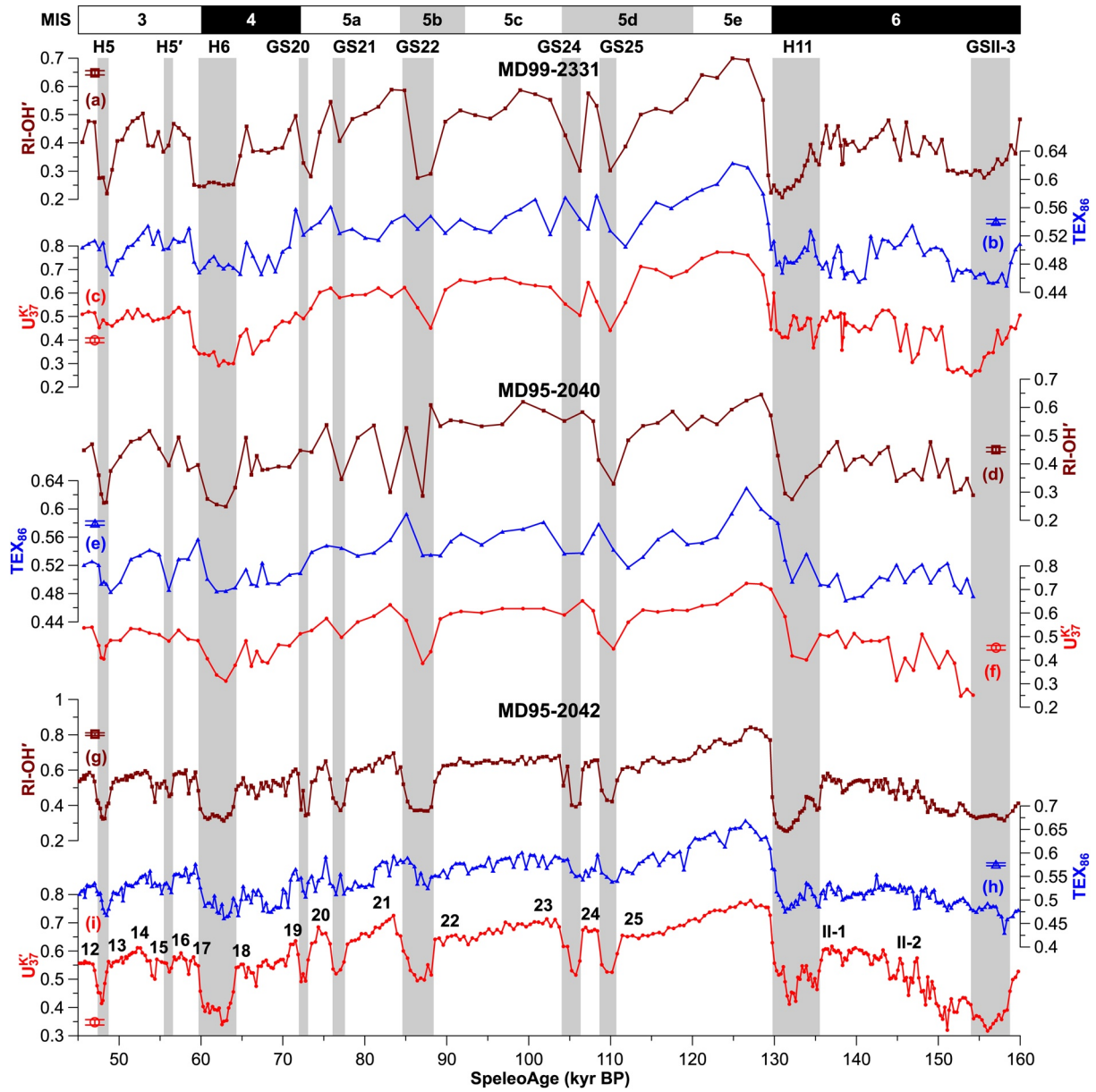

Figure 2. Organic paleothermometer results from Iberian Margin cores MD99-2331, MD95-2040, and MD95-2042 during the 160–45 ka BP period. RI-OH′ (ring index of hydroxylated tetraethers; Lü et al., 2015) records are in dark red, TEX_{86} (TetraEther indeX of tetraethers consisting of 86 carbon atoms; Schouten et al., 2002) records are in blue, and $U^{K'}{}_{37}$ (C_{37} ketone unsaturation ratio; Prahl & Wakeham, 1987) records are in red. (a–c) Records from core MD99-2331. (d–f) Records from core MD95-2040. (g–i) Records from core MD95-2042. Core MD95-2040 $U^{K'}{}_{37}$ data are from Pailler and Bard (2002) and core MD95-2042 $U^{K'}{}_{37}$ data covering the 70–45 ka BP period are from Darfeuil et al. (2016). Open symbols with colored error bars are 1σ analytical uncertainties. Black labels in (i) correspond to Dansgaard-Oeschger events. Labeled gray bars correspond to Greenland stadials (GS) and Heinrich events (H). Marine isotope stages (MIS) are named according to Railsback et al. (2015) and defined based on the core MD95-2042 benthic foraminifer $\delta^{18}O$ record in Figure S3a.

(Woodward, 2016; Woodward et al., 2017). Finally, we generated cross-correlograms with the "ccf" *R* function (R Core Team, 2020).

5. Results

5.1. Organic Paleothermometers and Associated Biomarker Concentrations

Organic paleothermometer results for the 160–45 ka BP period are shown in Figures 2 and S4 (see also Data Sets S1–S3). Averaged proxy values for selected periods and climatic modes—see the column "Data

points for averaged values" in Data Sets S1–S3—are shown in Table S3. Three GDGT-based data points from core MD95-2042 during the 162-158 ka BP period were excluded from any subsequent description and analysis due to their unexpectedly low TEX_{86} values (<0.4). Iberian Margin proxy value ranges during the 160-45 ka BP period are 0.21–0.84 for RI-OH′ (Figures 2a, 2d, and 2g), 1.26–1.47 for RI-OH (Figures S4a, S4d, and S4g), 0.43–0.67 for TEX_{86} (Figures 2b, 2e, and 2h), and 0.25–0.78 for $U^{K'}_{37}$ (Figures 2c, 2f, and 2i).

All four organic paleothermometers—in particular RI-OH′ and $U^{K'}_{37}$—respond to the penultimate deglaciation as well as Dansgaard-Oeschger and Heinrich events, with associated amplitudes generally exceeding at least twice the 1σ analytical uncertainties: 0.007 for RI-OH′, 0.008 for RI-OH, 0.003 for TEX_{86}, and 0.010 for $U^{K'}_{37}$ (Figures 2 and S4). The highest and lowest averaged proxy values for the 160–45 ka BP period occur during marine isotope stage (MIS) 5e—defined as the benthic foraminifer $\delta^{18}O$ "plateau" related to a sea level highstand in this study, see Figure S3a and Shackleton et al. (2002)—and Heinrich events at all three Iberian Margin sites, respectively (Table S3). MIS 5e also has higher averaged proxy values than the other MIS 5 warm periods, which themselves have higher averaged proxy values than MIS 5 cold periods and glacial MIS (MIS 6, 4, and 3). MIS 5e has higher averaged proxy values than the 1-0 ka BP period, except for core MD95-2040 GDGT-based proxies (Table S3).

Biomarker concentration results for the 160–45 ka BP period are shown in Figures 3 and S5. Iberian Margin biomarker concentration ranges during the 160–45 ka BP period are 0.01–1.43 μg/g for OH-GDGTs (Figures 3a, 3d, and 3g), 0.20–20.97 μg/g for iGDGTs (Figures 3b, 3e, and 3h), and 0.03–2.06 μg/g for C_{37} alkenones (Figures 3c, 3f, and 3i).

Biomarker concentrations generally decrease synchronously in response to cold millennial climatic events at the three Iberian Margin sites (Figures 3 and S5). Biomarker concentrations, especially those of OH-GDGT-0, peak at the three Iberian Margin sites during the end of Heinrich event H11, albeit less clearly for core MD95-2040 (Figures 3 and S5).

RI-OH′ and RI-OH versus $U^{K'}_{37}$ and TEX_{86} relationships are shown in Figures 4 and S6. To take full advantage of the use of a single set of lipid extracts, we omitted samples with only alkenone-based or GDGT-based data. All reported RI-OH′ and RI-OH versus $U^{K'}_{37}$ and TEX_{86} relationships are significant, with *r* values between 0.44 and 0.91 during the 160-45 ka BP period (Table S4).

During the 115-55 ka BP period, TEX_{86} has somewhat contrasting behaviors compared to RI-OH′, RI-OH, and $U^{K'}_{37}$ (Figures 2 and S4). We thus also consider the 115-55 ka BP period separately when quantifying RI-OH′ and RI-OH versus $U^{K'}_{37}$ and TEX_{86} relationships (Figures 4 and S6). During the 115-55 ka BP period, *r* values vary between 0.50 and 0.92 for all RI-OH′ and RI-OH versus $U^{K'}_{37}$ and TEX_{86} relationships (Table S4).

During the 160-45 ka BP period, RI-OH′ versus $U^{K'}_{37}$ relationships have higher *r* values than RI-OH′ versus TEX_{86} relationships, whereas the opposite occurs for RI-OH (Figure S6). Differences in *r* values between RI-OH′ versus $U^{K'}_{37}$ and RI-OH′ versus TEX_{86} relationships are even larger when focusing on the 115-55 ka BP period (Figures S6a–S6f). RI-OH versus $U^{K'}_{37}$ relationships also have higher *r* values than RI-OH versus TEX_{86} relationships during the 115–55 ka BP period (Figures S6g–S6l), but the differences are not as large as for RI-OH′.

5.2. Biomarker-Based SSTs and SST Latitudinal Gradients

Biomarker-based SSTs for the 160-45 ka BP period are shown in Figures 5 and S7–S9. Averaged biomarker-based SSTs for the 1-0 ka BP period are shown in Table 1. For all subsequent biomarker-based SST comparisons, we omit samples with only alkenone-based or GDGT-based data to take full advantage of the use of a single set of lipid extracts. Given that RI-OH′ and RI-OH do not have any Bayesian calibration to date, we describe non-Bayesian SST estimates (Figures 5 and S7). Iberian Margin biomarker-based SST ranges during the 160-45 ka BP period are 5.6–20.6°C for RI-OH′-SSTs (Figure 5; after Fietz et al., 2020), 8.2–20.0°C for RI-OH-SSTs (Figure S7; after Lü et al., 2015), 7.9–21.1°C for TEX_{86}^{H}-SSTs (Figure 5; after Darfeuil et al., 2016), and 6.0–21.9°C for $U^{K'}_{37}$-SSTs (Figure 5; after the linear calibration by Conte et al., 2006).

Biomarker-based SST latitudinal gradients along the Iberian Margin for selected time periods and climatic modes are shown in Figures 6, S10, and S11, as well as in Table S5. We allow the number of data points to

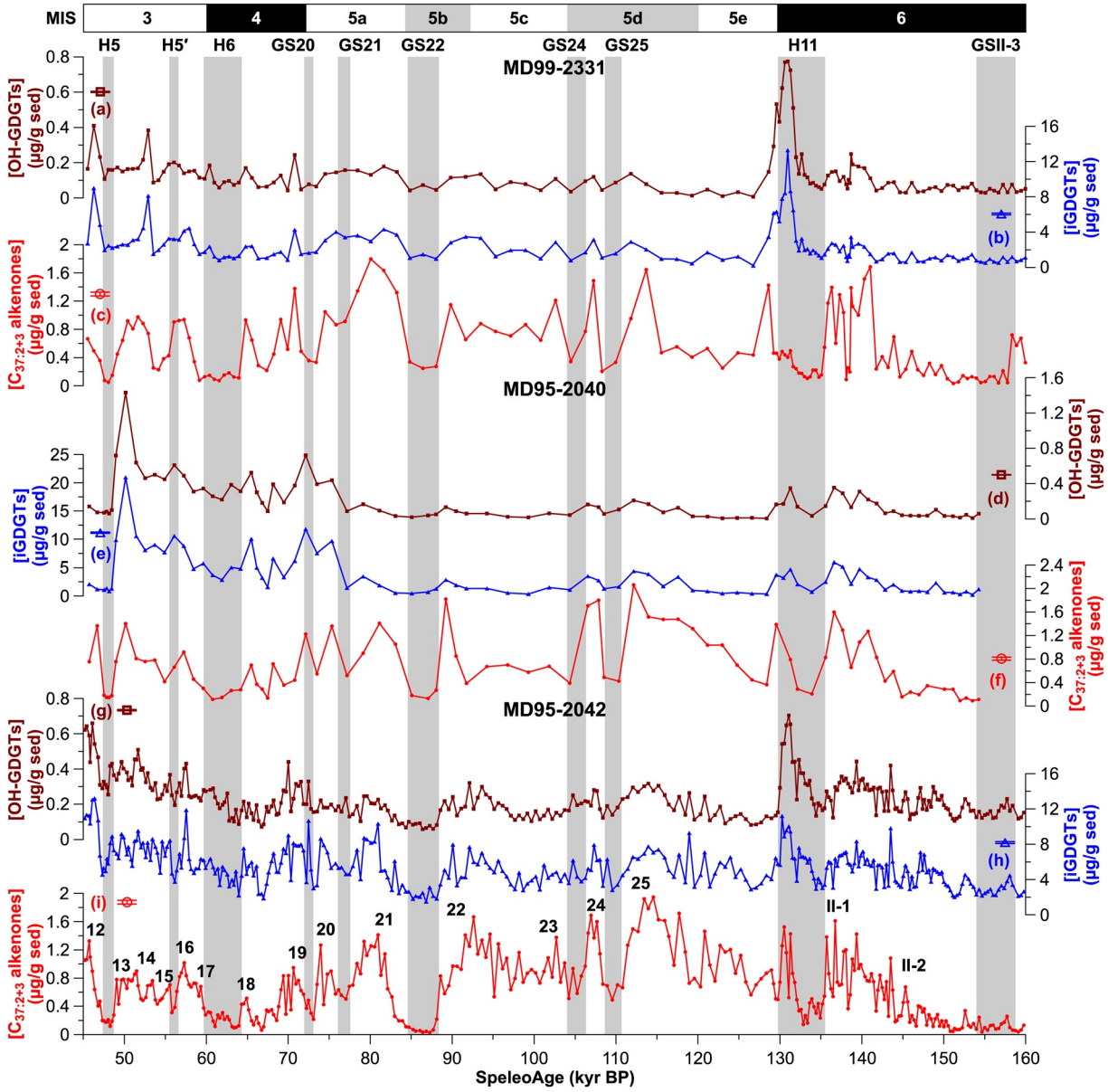

Figure 3. Biomarker concentration results from Iberian Margin cores MD99-2331, MD95-2040, and MD95-2042 during the 160-45 ka BP period. Total OH-GDGT (hydroxylated isoprenoid tetraether) concentration records are in dark red, total iGDGT (nonhydroxylated isoprenoid tetraether) concentration records are in blue, and summed di-unsaturated and tri-unsaturated C_{37} alkenone concentration records are in red. (a–c) Records from core MD99-2331. (d–f) Records from core MD95-2040. (g–i) Records from core MD95-2042. Core MD95-2040 C_{37} alkenone concentration data are from Pailler and Bard (2002) and core MD95-2042 C_{37} alkenone concentration data covering the 70-45 ka BP period are from Darfeuil et al. (2016). Open symbols with colored error bars are 1σ analytical uncertainties. Black labels in (i) correspond to Dansgaard-Oeschger events. Labeled gray bars correspond to Greenland stadials (GS) and Heinrich events (H). Marine isotope stages (MIS) are named according to Railsback et al. (2015) and defined based on the core MD95-2042 benthic foraminifer $\delta^{18}O$ record in Figure S3a.

vary between alkenone-based and GDGT-based paleothermometers, but exclude individual climatic events represented by only one point as well as data points within transitions between climatic events—see the column "Data points for SST latitudinal gradients" in Data Sets S1–S3. Based on differences between cores MD99-2331 and MD95-2042, biomarker-based SST latitudinal gradients per time period and climatic mode vary between −1.0 and 0.0°C/°latitude (Table S5).

Averaged differences between BAYSPLINE $U^{K'}_{37}$-SSTs (after Tierney & Tingley, 2018) and $U^{K'}_{37}$-SSTs (after the linear calibration by Conte et al., 2006) for the 160–45 ka BP period are of roughly −0.4°C with SDs of

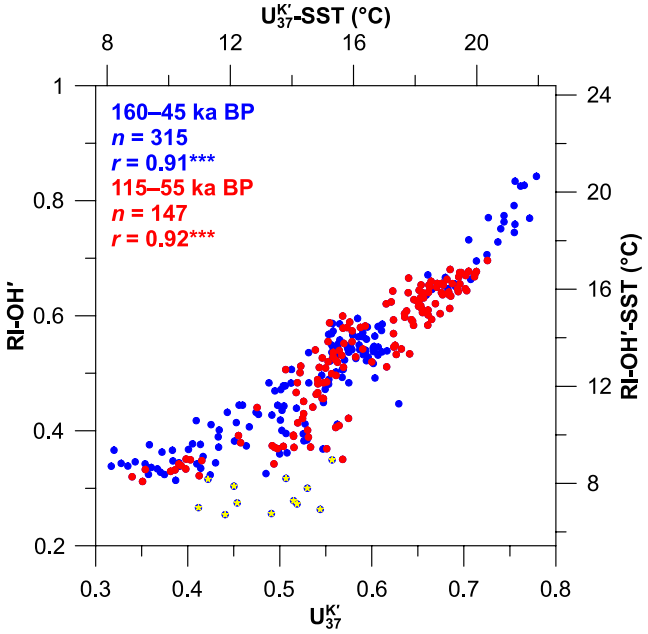

Figure 4. Correlation between RI-OH′ (ring index of hydroxylated tetraethers; Lü et al., 2015) and $U^{K'}_{37}$ (C_{37} ketone unsaturation ratio; Prahl & Wakeham, 1987) for the Iberian Margin core MD95-2042. Proxy value scales are shown with their conversions into sea surface temperature (SST) scales based on the following global calibrations: SST = (RI-OH′ + 0.029)/0.0422 (Fietz et al., 2020) and SST = 29.876 × $U^{K'}_{37}$ − 1.334 (Conte et al., 2006). The complete picture is provided in Figures S6, S8, and S9. Blue and red symbols refer to the 160–45 and 115–55 ka BP periods, respectively. Blue symbols with a yellow star refer to the 133–130 ka BP period, which corresponds to the primary productivity peak during the end of Heinrich event H11. The statistical significance level of $p < 0.001$ (from a nonparametric method that accounts for serial correlation; Ebisuzaki, 1997) is coded as ***.

less than 0.1°C for the three Iberian Margin cores (Data Sets S1–S3). The BAYSPLINE calibration by Tierney and Tingley (2018) does not change $U^{K'}_{37}$-SST latitudinal gradients (Table S5). Averaged differences between BAYSPAR TEX_{86}-SSTs (after Tierney & Tingley, 2014, 2015) and TEX_{86}^{H}-SSTs (after Darfeuil et al., 2016) for the 160-45 ka BP period are of −0.5, −0.4, and less than 0.1°C for cores MD99-2331 (n = 138, SD of 0.2 °C), MD95-2040 (n = 82, SD of 0.1°C), and MD95-2042 (n = 315, SD of 0.2°C), respectively (Data Sets S1–S3). The BAYSPAR calibration by Tierney and Tingley (2014, 2015) gives TEX_{86}-SST latitudinal gradients larger by up to nearly 0.2°C/°latitude than TEX_{86}^{H}-SST latitudinal gradients (Table S5). The averaged differences between Bayesian and non-Bayesian SST estimates for the 160–45 ka BP period are similar to those for the 1-0 ka BP period (Table 1). All averaged differences between Bayesian and non-Bayesian SST estimates are of the same order of magnitude as 1σ analytical uncertainties—0.2, 0.5, 0.1, and 0.3°C in RI-OH′-SSTs, RI-OH-SSTs, TEX_{86}-SSTs, and $U^{K'}_{37}$-SSTs, respectively—and are much smaller than 1σ standard deviations of regression residuals—1.1°C for $U^{K'}_{37}$ after Conte et al. (2006), 2.5°C for TEX_{86}^{H} after Darfeuil et al. (2016), and roughly 6°C for RI-OH′ and RI-OH after Fietz et al. (2020) and Lü et al. (2015).

5.3. Phase Relationships Between Organic Paleothermometers and Between Biomarker Concentrations

The paleothermometric records considered for visual phase relationship analyses and cross-correlograms are shown in Figures 7 and S12. The phase relationship analyses focus on core MD95-2042 because we obtained the best temporally resolved biomarker-based records from this Iberian Margin sediment core. Visually, RI-OH′ and RI-OH are in phase with $U^{K'}_{37}$ but lag TEX_{86} during several cold climatic events such as GS25, GS24, GS22, and H5 (Figures 7a–7c and S12a–S12c).

For cross-correlations between band-pass filtered records (500–10,000-years window), we considered phase relationships relative to RI-OH′ (Figure 7f), RI-OH (Figure S12f), and OH-GDGT concentrations (Figures 7g and S12g). As for proxy-proxy relationships, we not only considered the 156-50 ka BP period, taking into account the edge effect, but also the 115-55 ka BP period when TEX_{86} most clearly disagrees with RI-OH′, RI-OH, and $U^{K'}_{37}$ (Data Set S4). The band-pass filtering preserves the stronger RI-OH′ versus $U^{K'}_{37}$ relationships compared to RI-OH′ versus TEX_{86} and RI-OH versus $U^{K'}_{37}$ and TEX_{86} relationships (section 5.1). During the 156-50 and 115-55 ka BP periods, RI-OH′ and RI-OH lead $U^{K'}_{37}$ by less than 100 years on average (Figures 7f and S12f). During the 156-50 ka BP period, RI-OH′ and RI-OH lag TEX_{86} by 140 and 70 years on average, respectively. During the 115-55 ka BP period, RI-OH′ and RI-OH averaged lags relative to TEX_{86} increase to 190 and 100 years, respectively (Figures 7f and S12f). During the 156-50 and 115-55 ka BP periods, OH-GDGT concentrations have phase differences with C_{37} alkenone and iGDGT concentrations of less than 100 years on average (Figures 7g and S12g).

6. Discussion

6.1. Paleothermometric Potential of OH-GDGTs

6.1.1. Better Paleothermometric Potential for RI-OH′ than for TEX_{86} and RI-OH in the Iberian Margin

RI-OH′ not only responds to characteristic North Atlantic climatic events but also better resembles $U^{K'}_{37}$ (r values of 0.77–0.91 for the 160–45 ka BP period) than TEX_{86} (r values of 0.70–0.80 for the 160–45 ka BP period) at the three Iberian Margin study sites (Figures 2 and S6a–S6f; Section 5.1). While our results are

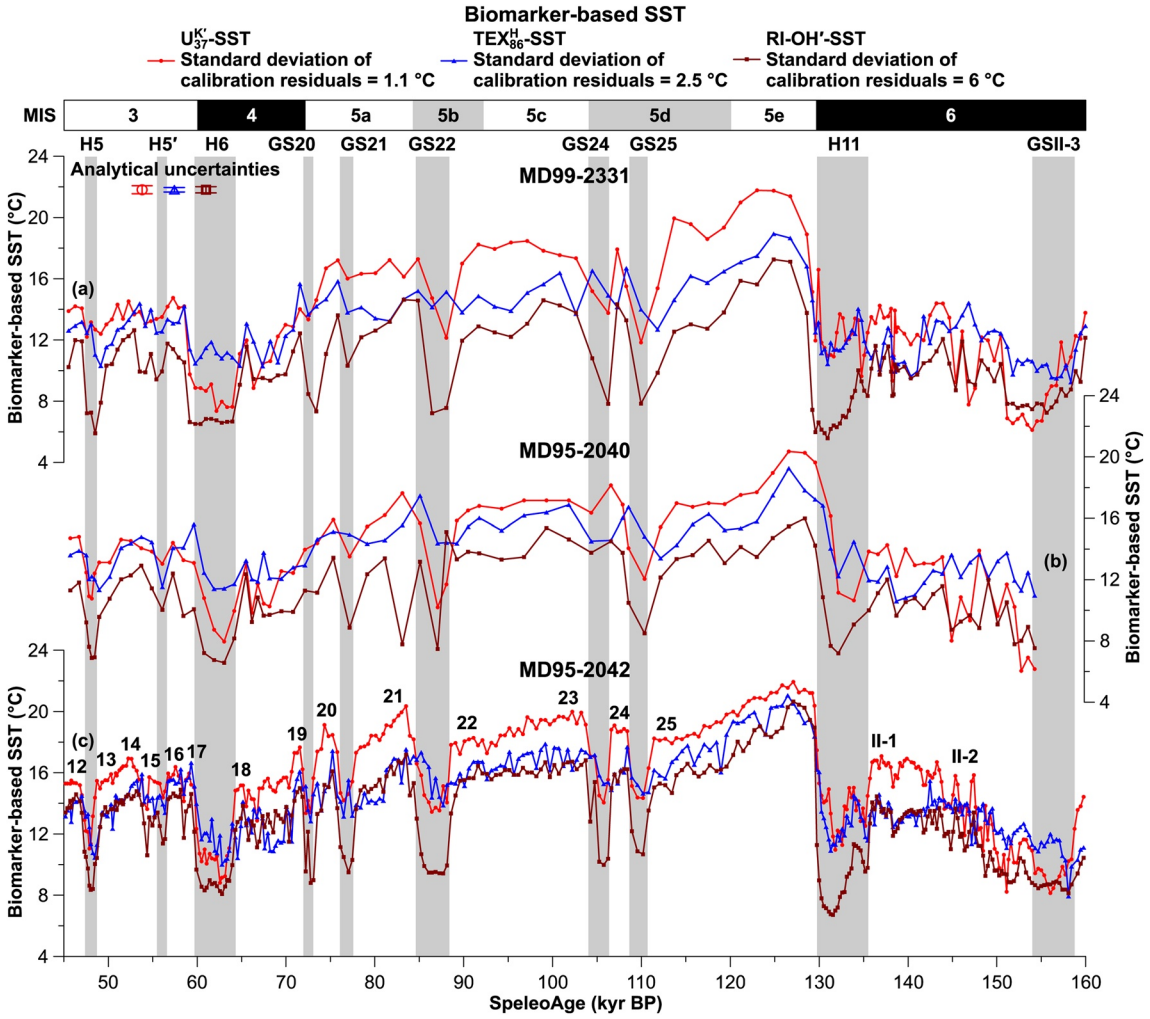

Figure 5. Same as Figure 2, but with biomarker-based sea surface temperature (SST) results from Iberian Margin cores MD99-2331, MD95-2040, and MD95-2042 during the 160-45 ka BP period. (a) Records from core MD99-2331. (b) Records from core MD95-2040. (c) Records from core MD95-2042. RI-OH′-SST estimates are based on the following global calibration: SST = (RI-OH′ + 0.029)/0.0422 (Fietz et al., 2020). $U^{K'}_{37}$-SST estimates are based on the following global calibration: SST = 29.876 × $U^{K'}_{37}$ − 1.334 (Conte et al., 2006). TEX_{86}^{H}-SST estimates are based on the following regional paleocalibration: SST = 68.4 × TEX_{86}^{H} + 33.0 (Darfeuil et al., 2016).

unsurprising for $U^{K'}_{37}$ (e.g., Darfeuil et al., 2016; Martrat et al., 2007; Pailler & Bard, 2002), they seem less predictable for a GDGT-based paleothermometer such as RI-OH′ in the Iberian Margin. Off this margin, surface sediments contain iGDGTs not only from Atlantic surface waters but also from Mediterranean Outflow Waters (presently at 500–1,600 m water depth; Kim et al., 2016; Figure 1c). Even if TEX_{86} resembles $U^{K'}_{37}$ in core MD95-2042 during the last 70 kyrs, Iberian Margin downcore sediments likely contain iGDGTs produced by endemic archaea within the Mediterranean Outflow Waters (Darfeuil et al., 2016). A global study of the archeal lipidome in suspended particles has found that not only iGDGTs but also OH-GDGTs are produced in both surface and deep waters (boundary at 100 m water depth; Zhu et al., 2016), with likely variable relative contributions from different water depths through time (e.g., Fietz et al., 2016; Hertzberg et al., 2016; Huguet et al., 2007; Y. Wu et al., 2020). However, a study of archeal GDGTs in suspended particles from the Yangtze River Estuary found higher OH-GDGT/iGDGT ratios in surface waters than in deep waters (boundary at roughly 30 m water depth), suggesting that OH-GDGT production is essentially restricted to surface waters (Lü et al., 2019). Given that the novel RI-OH′ paleothermometer best resembles the established $U^{K'}_{37}$ SST proxy, our results tend to support OH-GDGT production restricted to Atlantic surface waters, though with a possible and variable relative contribution from subsurface waters at most 200 m

Table 1
Comparison of Averaged Biomarker-Based Sea Surface Temperature (SST) Estimates for the Last Millenium With Observed SSTs

	Observed SST (°C)[a]		Biomarker-based SST 1–0 ka BP (°C)[b]					
Core	Annual	Range	RI-OH′	RI-OH	TEX_{86}^{H}	BAY-TEX_{86}	$U^{K'}_{37}$	BAY-$U^{K'}_{37}$
MD99-2331	16.0	13.5–18.8	15.4	14.1	17.3	16.6	16.2	15.7
(n = 4)			(0.6)	(0.7)	(0.8)	(0.8)	(0.5)	(0.5)
MD95-2040	16.8	14.1–19.9	16.7	16.2	18.9	18.5	17.7	17.2
(n = 4[c])			(0.5)	(0.6)	(0.5)	(0.6)	(1.1)	(1.1)
MD95-2042	18.1	15.5–21.1	17.9	17.3	18.9	18.9	19.0	18.6
(n = 7)			(0.2)	(0.5)	(0.2)	(0.2)	(0.2)	(0.2)

Note. TEX_{86}^{H} = log(TEX_{86}) with TEX_{86} = TetraEther indeX of tetraethers consisting of 86 carbon atoms (Kim et al., 2010; Schouten et al., 2002), $U^{K'}_{37}$ = C_{37} ketone unsaturation ratio (Prahl & Wakeham, 1987), and RI-OH and RI-OH′ = ring index of hydroxylated tetraethers (Lü et al., 2015).

[a]Pathfinder SST V5 climatologies for the 1982–2010 period (Casey et al., 2010). The SST ranges correspond to February (minimum) and August (maximum). [b]Averaged biomarker-based SST estimates are presented with their standard deviations in brackets. RI-OH′-SST estimates are from the following global calibration: SST = (RI-OH′ + 0.029)/0.0422 (Fietz et al., 2020). RI-OH-SST estimates are from the following global calibration: SST = (RI-OH−1.11)/0.018 (Lü et al., 2015). TEX_{86}^{H}-SST estimates are from the following regional paleocalibration: SST = 68.4 × TEX_{86}^{H} + 33.0 (Darfeuil et al., 2016). BAY-TEX_{86}-SST estimates are from the BAYSPAR calibration (Tierney & Tingley, 2014, 2015). $U^{K'}_{37}$-SST estimates are from the following global calibration: SST = 29.876 × $U^{K'}_{37}$−1.334 (Conte et al., 2006). BAY-$U^{K'}_{37}$-SST estimates are from the BAYSPLINE calibration (Tierney & Tingley, 2018). [c]Core MD95-2040 has two missing data points for $U^{K'}_{37}$.

deep (Zhang & Liu, 2018)—an idea further discussed in Sections 6.1.2, 6.2.2, 6.2.3 and 6.3.4. Accordingly, we suggest that RI-OH′ records SST better than TEX_{86} does in the Iberian Margin.

RI-OH does not respond to characteristic North Atlantic climatic events as clearly as does RI-OH′ (Figures 2 and S4). In particular, RI-OH values do not decrease during H6 for cores MD99-2331 and MD95-2042. RI-OH versus $U^{K'}_{37}$ relationships (r values of 0.44–0.66 for the 160–45 ka BP period) are also less linear than RI-OH′ versus $U^{K'}_{37}$ relationships (Figures S6a–S6c and S6g–S6i; Section 5.1). Our results differ with those reported by Davtian et al. (2019), as both RI-OH′ and RI-OH systematically and coherently respond to well-known climatic events in the Gulf of Lions. Following their global core top compilation, Lü et al. (2015) found the smallest RI-OH′ and largest RI-OH residuals at the lowest SSTs and recommended to use RI-OH′ rather than RI-OH for polar oceans. Consequently, all subsequent validations of the RI-OH′ paleothermometer focused on polar oceans (Allaart et al., 2020; Kremer et al., 2018; Liu et al., 2020; Park et al., 2019; Vorrath et al., 2020; J. Wu et al., 2020; see also Fietz et al., 2020 for a review). While the Iberian Margin is not presently under the influence of (sub)polar waters, it was during Heinrich events when the Polar Front reached this margin (Bard, Arnold, Maurice, et al., 1987; Eynaud et al., 2009). We thus suggest that RI-OH′ better reflects the influence of (sub)polar waters during Heinrich events than does RI-OH in the Iberian Margin.

6.1.2. Detailed Contrasts in RI-OH′ and $U^{K'}_{37}$ Behaviors

Despite its general resemblance with $U^{K'}_{37}$, RI-OH′ better resembles TEX_{86} than $U^{K'}_{37}$ during H11 in cores MD99-2331 and MD95-2042 (Figures 2a–2c and 2g–2i). $U^{K'}_{37}$ records from cores MD99-2331 and MD95-2042 have a “double-u” shaped H11—a structure first described by Martrat et al. (2014) and also visible in the lower-resolution MD95-2042 $U^{K'}_{37}$ record by Pailler and Bard (2002)—and the second H11 cooling is synchronous with the biomarker concentration peak at these Iberian Margin study sites (Figures 3a–3c, 3g–3i, S5a–S5c, and S5g–S5i; Section 5.1). The biomarker concentration peak at the end of H11 is related to a peak in primary productivity within the Iberian Margin, interpreted as an enhanced summer upwelling (Hodell et al., 2013; Pailler & Bard, 2002; Thomson et al., 2000). Contrary to $U^{K'}_{37}$, RI-OH′, RI-OH, and TEX_{86} either reach or get close to their lowest values during the end of H11 in cores MD95-2331 and MD95-2042 (Figures 2 and S4, see also Figure S6). One potential mechanism related to the enhanced summer upwelling is a bias toward the warm season for $U^{K'}_{37}$, though the increase in C_{37} alkenone concentrations

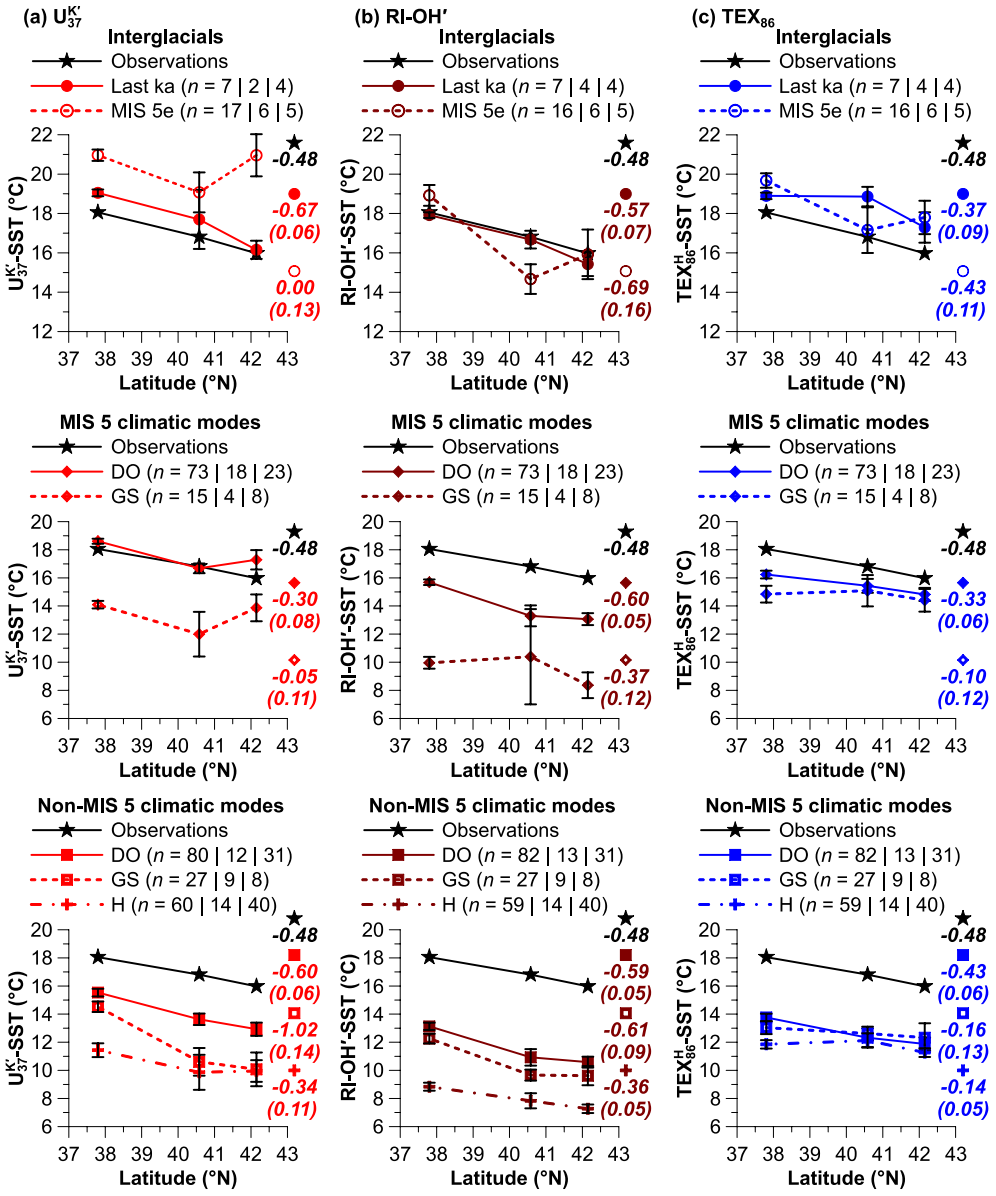

Figure 6. Sea surface temperature (SST) latitudinal gradients for different climatic modes along Iberian Margin cores MD99-2331, MD95-2040, and MD95-2042. (a) $U^{K'}_{37}$-SST estimates from the following global calibration: $SST = 29.876 \times U^{K'}_{37} - 1.334$ (Conte et al., 2006). (b) RI-OH′-SST estimates from the following global calibration: $SST = (RI\text{-}OH' + 0.029)/0.0422$ (Fietz et al., 2020). (c) TEX_{86}^{H}-SST estimates from the following regional paleocalibration: $SST = 68.4 \times TEX_{86}^{H} + 33.0$ (Darfeuil et al., 2016). Error bars correspond to 2σ standard errors of the mean SSTs per core and per climatic mode. For each core, individual climatic events represented by only one point for all proxies are excluded as well as data points within transitions between climatic events—see the column "Data points for SST latitudinal gradients" in Data Sets S1–S3. SST latitudinal gradients based on differences between cores MD99-2331 and MD95-2042 are also shown with their propagated 1σ standard errors in brackets. Observed SSTs are based on Pathfinder SST V5 climatologies for the 1982–2010 period (Casey et al., 2010). MIS 5e corresponds to the thermal optimum during the 129–121, 130–121, and 129.5–120.3 ka BP periods for cores MD99-2331, MD95-2040, and MD95-2042, respectively. MIS 5e is excluded from MIS 5 DO. MIS, marine isotope stage; DO, Dansgaard-Oeschger events; GS, Greenland stadials, and H, Heinrich events. $TEX_{86}^{H} = \log(TEX_{86})$ with TEX_{86} = TetraEther indeX of tetraethers consisting of 86 carbon atoms (Kim et al., 2010; Schouten et al., 2002), $U^{K'}_{37} = C_{37}$ ketone unsaturation ratio (Prahl & Wakeham, 1987), and RI-OH′ = ring index of hydroxylated tetraethers (Lü et al., 2015).

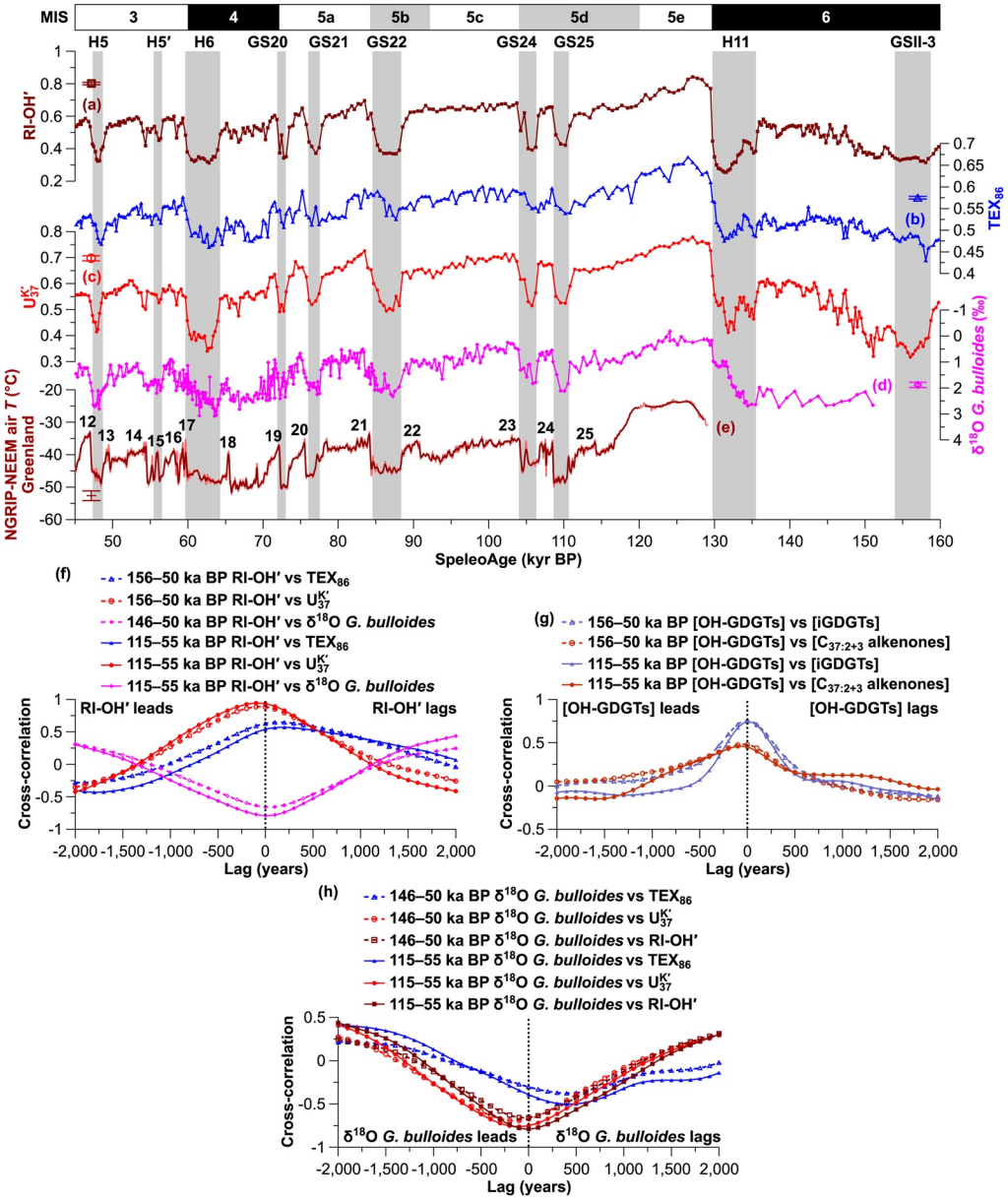

Figure 7. Phase relationships between Iberian Margin core MD95-2042 paleothermometric proxies and Greenland temperature. (a) RI-OH′ (ring index of hydroxylated tetraethers; Lü et al., 2015). (b) TEX_{86} (TetraEther indeX of tetraethers consisting of 86 carbon atoms; Schouten et al., 2002). (c) $U^{K'}{}_{37}$ (C_{37} ketone unsaturation ratio; Prahl & Wakeham, 1987). (d) Isotopic composition of oxygen ($\delta^{18}O$) of *G. bulloides* tests (planktic foraminifers; Shackleton et al., 2000): note the reversed axis. (e) North Greenland Ice Core Project (NGRIP; Kindler et al., 2014) and North Greenland Eemian Ice Drilling (NEEM; NEEM community members, 2013) air temperature with 11-point moving averages (thick curves): NEEM temperature anomaly values are shifted by −31°C. (f) Cross-correlations between RI-OH′ and other paleothermometric proxies in core MD95-2042. (g) Cross-correlations between total OH-GDGT concentration and total concentration of other lipid classes in core MD95-2042. (h) Cross-correlations between $\delta^{18}O$ of *G. bulloides* tests (planktic foraminifers; Shackleton et al., 2000) and other paleothermometric proxies in core MD95-2042. Open symbols with colored error bars are 1σ analytical uncertainties, except for the record in (e) where the error bar corresponds to temperature amplitude uncertainties. Black labels in (e) correspond to Dansgaard-Oeschger events. Labeled gray bars correspond to Greenland stadials (GS) and Heinrich events (H). Marine isotope stages (MIS) are named according to Railsback et al. (2015) and defined based on the core MD95-2042 benthic foraminifer $\delta^{18}O$ record in Figure S3a. Prior to cross-correlation analyses, a fourth-order Butterworth band-pass filter (500–10,000-years window) was applied to all evenly resampled (every 10 years) core MD95-2042 records. GDGT, glycerol dialkyl glycerol tetraether.

is relatively modest (Figures 3c, 3f, and 3i), whereas archeal producers may be more competitive for nutrients at the end of the upwelling, which may bias GDGT-based proxies toward the cold season or larger export depths (Darfeuil et al., 2016). Alternatively, increased ammonia oxidation rates related to stronger upwelling could generate cold biases for at least TEX_{86} and TEX_{86}^{H} (Hurley et al., 2016; Lawrence et al., 2020; Lü et al., 2019). A third possibility is that the particularly pronounced OH-GDGT-0 concentration peak compared to other archeal GDGTs (Figures 3 and S5) is partly due to archaea other than *Thaumarchaeota* (Liu et al., 2012; Ma et al., 2020; Yang et al., 2019). Assuming that seasonal biomarker production, larger export depths, increased ammonia oxidation rates, and shifts in archeal communities related to stronger upwelling generate cold biases for all archeal GDGT-based indices and warm biases for $U^{K'}_{37}$, we suggest that alkenones and archeal GDGTs record somewhat different signals during H11.

Contrary to $U^{K'}_{37}$, RI-OH′ suggests barely colder Heinrich events (H11, H6, and H5) than MIS 5 stadials (GS25, GS24, and GS22–GS20) in core MD95-2042 (Figures 2g and 2i; Section 5.1). Such a contrast is also relevant for RI-OH to a lesser extent (Figures S4g and S4i). During Heinrich events H6-H1, primary productivity dropped and the nutricline deepened (e.g., Ausín et al., 2020; Incarbona et al., 2010; Pailler & Bard, 2002). Similarly, biomarker concentrations dropped during all MIS 5 stadials (Figures 3 and S5) which Eynaud et al. (2000) described as Heinrich-like events. Assuming that the nutricline deepened not only during Heinrich events but also during MIS 5 stadials, Atlantic shallow water *Thaumarchaeota* may have migrated toward deeper, colder waters (Hertzberg et al., 2016; Park et al., 2018). Alternatively, shifts in *Thaumarchaeota* communities (Polik et al., 2018) may have biased RI-OH′ and RI-OH values. However, most studies suggesting ecological effects and other nonthermal effects on archeal GDGT distributions are restricted to iGDGTs and their derived TEX_{86} paleothermometer (e.g., Elling et al., 2014, 2015; Evans et al., 2018; Hurley et al., 2016, 2018; Junium et al., 2018; Lawrence et al., 2020; Lü et al., 2019; Ma et al., 2020; Park et al., 2018; Polik et al., 2018; Qin et al., 2015; Wei et al., 2020; Xie et al., 2014). In principle, bioturbation could also be invoked to explain the contrasts between RI-OH′ and $U^{K'}_{37}$, notably during the Heinrich-like event GS22 which has particularly contrasting relative decreases in OH-GDGT and C_{37} alkenone concentrations (Figure S13). However, as shown in Section 6.3.1, it is unlikely that bioturbation is the cause of the observed differences. In all cases, more studies involving both OH-GDGTs and iGDGTs are needed to assess to what extent biases for TEX_{86} are also relevant for RI-OH′ and RI-OH.

6.2. OH-GDGT-Based Temperature Assessments

6.2.1. Offsets Between OH-GDGT-Based Temperatures and Other Biomarker-Based Temperatures

Given the small differences between Bayesian and non-Bayesian SST estimates (Section 5.2), we focus on the latter only in order not to mix different types of uncertainties for biomarker-based SST comparisons (Table S4). Averaged differences between RI-OH′-SSTs and other biomarker-based SSTs range between −3.1 and −1.5°C (Figure 5). Averaged differences between RI-OH-SSTs and other biomarker-based SSTs range between −1.9 and −0.7°C (Figure S7).

Individual differences between OH-GDGT-based SSTs and SST estimates from $U^{K'}_{37}$ and TEX_{86} are smaller than the 1σ standard deviations of single pairs based on propagated non-Bayesian regression residuals, which range between 6.1 ($\sigma = \sqrt{[1.1^2 + 6.0^2]}$) and 6.5°C ($\sigma = \sqrt{[2.5^2 + 6.0^2]}$). However, most individual differences are negative and the 1σ standard errors ($\sigma/\sqrt{n}$) of the averaged differences range between 0.1°C and 0.3°C, which is close to 1σ analytical uncertainties of 0.1°C–0.5°C. We thus consider that the averaged differences between OH-GDGT-based SSTs and other biomarker-based SSTs are systematic, especially for RI-OH′-$U^{K'}_{37}$ and RI-OH′-TEX_{86}^{H} SST offsets.

While RI-OH′-$U^{K'}_{37}$ and RI-OH′-TEX_{86}^{H} SST offsets are larger than RI-OH-$U^{K'}_{37}$ and RI-OH-TEX_{86}^{H} SST offsets, RI-OH′-SSTs and $U^{K'}_{37}$-SSTs have nearly 1:1 relationships, which is not the case for RI-OH-SST versus $U^{K'}_{37}$-SST relationships (Figures S8a–8c and S8g–8i). Conversely, RI-OH′-SSTs and RI-OH-SSTs both tend to have 1:1 relationships with TEX_{86}^{H}-SSTs (Figures S8d–8f and S8j–8l). The nearly 1:1 relationships between biomarker-based SSTs reflect similar warmings during the penultimate deglaciation as well as similar SST amplitudes during millennial climatic events, especially between RI-OH′-SSTs and $U^{K'}_{37}$-SSTs (Figures 5 and S7). Given that RI-OH′-SSTs systematically have 1:1 relationships with $U^{K'}_{37}$-SSTs and

TEX_{86}^{H}-SSTs and that those relationships are all linear (Section 6.1.1), we consider that RI-OH′-SSTs are more plausible than RI-OH-SSTs even though the former look less realistic in absolute values than the latter, so the remainder of the discussion focuses only on RI-OH′ and RI-OH′-SSTs.

6.2.2. Imperfect Existing Core Top Calibration as the Most Plausible Reason for OH-GDGT Temperature Underestimation in the Iberian Margin

While Davtian et al. (2019) suggested that the global calibration by Lü et al. (2015) could be invalid for the semi-enclosed Mediterranean Sea, this shortcoming may also apply for the Iberian Margin despite its location in an open ocean. One third of the core top sediments compiled by Fietz et al. (2020)—54 out of 167—are from the Chinese coastal seas, whereas only three and two core top sediments are from the Mediterranean Sea and the North Atlantic excluding the Nordic seas, respectively. When the South Atlantic is included, the number of Atlantic core top sediments increases to seven and this number further increases to 23 when the Fram Strait is added (Fietz et al., 2013; Huguet et al., 2013), which corresponds to only 13.8% of the global core top data set compiled by Fietz et al. (2020). The standard deviation of regression residuals of roughly 6°C further illustrate the weaknesses of the global RI-OH′ calibration established by Fietz et al. (2020) for SST estimates in the Iberian Margin, as well as nonthermal effects to be explored. Given that the North Atlantic is poorly represented in the available OH-GDGT core top data set, a North Atlantic core top calibration for OH-GDGT-based paleothermometers would be premature at this stage.

We also evaluate systematic biases toward the cold season for OH-GDGT-based paleothermometers and their possibility to record sea temperatures at 0- to 200-m rather than SSTs, as previously suggested by Davtian et al. (2019) for the Gulf of Lions. Based on Pathfinder SST V5 climatologies at 4 km resolution for the 1982–2010 period, winter (January–March) and annual SSTs differ by −2.3°C, −2.5°C, and −2.4°C at the MD99-2331, MD95-2040, and MD95-2042 sites, respectively (Casey et al., 2010). Based on World Ocean Atlas 2018 statistical means on 1/4° grids for the 1981–2010 period, sea temperatures at 0- to 200-m and annual SSTs differ by −2.0°C, −2.4°C, and −2.4°C at the MD99-2331, MD95-2040, and MD95-2042 sites, respectively (Locarnini et al., 2019). Differences of −2.5°C to −2.0°C represent at least two thirds of RI-OH′-$U^{K'}_{37}$ SST offsets at the three Iberian Margin study sites, while RI-OH′-SSTs have smaller averaged differences with TEX_{86}-derived sea temperatures at 0- to 200-m (gamma function probability distribution for target temperatures with $a = 4.5$ and $b = 15$; Tierney & Tingley, 2015) than with TEX_{86}-SSTs and TEX_{86}^{H}-SSTs (Table S4), which seemingly supports the systematic biases suggested by Davtian et al. (2019). However, the negative RI-OH′-TEX_{86}^{H} SST offsets (Figure 5), including during the 1–0 ka BP period (Table 1) do not support a systematic bias toward the cold season or signal export from deep waters for all archeal GDGT-based paleothermometers, even if such biases may occur during specific periods (Section 6.1.2). During the 1–0 ka BP period, RI-OH′-SSTs are similar to modern annual SSTs at the three Iberian Margin study sites (Table 1; Casey et al., 2010), which further suggests an insignificant seasonal bias for RI-OH′, at least during the last millenium. In addition, regional simulations by Darfeuil et al. (2016) and Atlantic core top data set analyses by Zhang and Liu (2018) suggest that archeal GDGTs record SSTs rather than sea temperatures at 0- to 200-m when the influence of iGDGTs from the Mediterranean Outflow Waters in the Iberian Margin is excluded. Given that we cannot unambiguously attribute the negative RI-OH′-$U^{K'}_{37}$ and RI-OH′-TEX_{86}^{H} SST offsets to systematic seasonal and export depth biases for OH-GDGTs in the Iberian Margin, such possibilities should be investigated in a future North Atlantic or Iberian Margin regional core top calibration.

Davtian et al. (2019) provisionally suggested that their RI-OH-SSTs from the Gulf of Lions could either represent winter SSTs or sea temperatures at 0- to 200-m rather than annual SSTs. However, we cannot trustfully make similar conclusions for Iberian Margin RI-OH′-SSTs, even though the better agreement of RI-OH′-SSTs with TEX_{86}^{H}-SSTs than with $U^{K'}_{37}$-SSTs, especially during DO events and MIS 5e (Figure 5) may support a contribution from subsurface waters (<200 m water depth), which may have increased during H11 (Section 6.1.2). The imperfection of the existing global calibration could thus be the most plausible reason for the reported RI-OH′-$U^{K'}_{37}$ SST offsets in the Iberian Margin.

6.2.3. No Evidence of OH-GDGTs From the Mediterranean Outflow Waters in the Iberian Margin

Putting our study and that of Davtian et al. (2019) into perspective allows to tentatively assess the influence of OH-GDGTs from the Mediterranean Outflow Waters in the Iberian Margin (Figure 1c). Mediterranean

deepwater *Thaumarchaeota* (presently 500–1,600 m water depth in the Iberian Margin and > 100 m water depth in the Mediterranean Sea) generates a warm bias by roughly 5°C–6°C in TEX_{86}^{H}-SSTs from Mediterranean Sea and Iberian Margin sediments (Besseling et al., 2019; Darfeuil et al., 2016; Kim et al., 2015, 2016) and a similar bias could also occur for RI-OH′ (Zhu et al., 2016). The warm biases in GDGT-based SSTs generated by Mediterranean deepwater *Thaumarchaeota* are attributable to different GDGT-temperature relationships between shallow water and deepwater *Thaumarchaeota* (Zhu et al., 2016). However, when considering Bayesian $U^{K'}_{37}$-SST estimates after Tierney and Tingley (2018) for the Gulf of Lions and the Iberian Margin, RI-OH′-$U^{K'}_{37}$ SST offsets are more negative at the deep sea Iberian Margin (averages between −2.7°C and −2.2°C; Figure S9) than at the shallow sea Gulf of Lions (−0.8°C on average during the 160–45 ka BP period, SD of 1.7°C, $n = 216$; Davtian et al., 2019). The larger negative RI-OH′-$U^{K'}_{37}$ SSTs offsets at deep sea sites compared to a shallow sea site do not support a warm bias in OH-GDGT-based SSTs due to Mediterranean deepwater *Thaumarchaeota* off Portugal. In addition, we used a regional paleocalibration for TEX_{86}^{H} (Darfeuil et al., 2016) and a spatially varying calibration for TEX_{86} (Tierney & Tingley, 2014, 2015) that both address the influence of iGDGTs from the Mediterranean Outflow Waters in the Iberian Margin. For RI-OH′, we used the latest global calibration available to date (Fietz et al., 2020) and do not expect this calibration to address local influences of OH-GDGTs from the Mediterranean Outflow Waters. The more negative RI-OH′-$U^{K'}_{37}$ offsets at three deep sea sites compared to a shallow sea site do not support a similar bias on iGDGT-based and OH-GDGT-based SSTs due to Mediterranean deepwater *Thaumarchaeota* in the Iberian Margin, which further suggests different origins for both archeal GDGT groups.

6.2.4. Plausible and Coherent Temperature Latitudinal Gradients Between Novel and Established Organic Paleothermometers

As was the case for absolute biomarker-based SSTs, we also focus on non-Bayesian SST latitudinal gradients (Figure 6, Table S5), but the discussion varies little when Bayesian SST latitudinal gradients are considered instead (Section 5.2). For the 1–0 ka BP period, organic paleothermometers give SST latitudinal gradients between −0.7°C and −0.4 °C/°latitude, which is reasonably consistent with the modern SST latitudinal gradient of −0.5°C/°latitude (Table 1; Casey et al., 2010) and with foraminifer-based SST latitudinal gradients (Martins et al., 2015; Salgueiro et al., 2010, 2014). With SST latitudinal gradients between −0.6°C and −0.3°C/°latitude, all organic paleothermometers support a past hydrology during Dansgaard-Oeschger interstadials which is similar to the modern one (Salgueiro et al., 2010; Voelker & Abreude, 2011, and references therein; Voelker et al., 2009). All biomarker-based SST latitudinal gradients tend to flatten during MIS 5 Greenland stadials and Heinrich events compared to Dansgaard-Oeschger interstadials, whereas those gradients either steepen (RI-OH′-SSTs and $U^{K'}_{37}$-SSTs) or flatten (TEX_{86}^{H}-SSTs) during glacial Greenland stadials. In general, RI-OH′ gives SST latitudinal gradients consistent with those from independent paleothermometers, which validates this novel proxy.

The only clear disagreement between alkenone-based and GDGT-based SST latitudinal gradients occurs during MIS 5e, as $U^{K'}_{37}$-SSTs depict a latitudinal gradient of 0.0 °C/°latitude whereas RI-OH′-SSTs and TEX_{86}^{H}-SSTs depict latitudinal gradients of −0.7°C and −0.4°C/°latitude, respectively (Figure 6). MIS 5e thus seems to have a different hydrology compared to the modern one. Strengthened Iberian Poleward Current influence at the MD99-2331 site may have occurred during MIS 5e (Figure 1c), a possibility to be further investigated with more sediment core records, as was undertaken by Salgueiro et al. (2014) and Martins et al. (2015) for the last 40 kyrs. Alternatively, lateral advection may have occurred during MIS 5e and affected more severely alkenones than archeal GDGTs, assuming that iGDGTs and OH-GDGTs behave similarly (Ausín et al., 2019; Mollenhauer et al., 2008; Shah et al., 2008). However, the lack of a clear phase difference between C_{37} alkenone and archeal GDGT concentrations as well as between their derived paleothermometers during MIS 5e (Figures 2 and 3) detracts from the idea of a differential lateral advection between these lipid classes. Whatever the hydrographic mechanism(s), a better understanding of OH-GDGT-based proxies is necessary for further discussion.

Our averaged SST latitudinal gradients of between −0.4°C and −0.1°C/°latitude for Heinrich events best agree with those of H2a (−0.2°C/°latitude), H1 (−0.6°C/°latitude), and H3 (−0.7°C/°latitude) from Salgueiro et al. (2014) when considering the same three Iberian Margin sediment cores (Figure 6). During H1 and H3, which were the coldest Heinrich events in the Iberian Margin during the last 35 kyrs (Salgueiro et al., 2014), (sub)polar waters reached all three study sites (Eynaud et al., 2009; Salgueiro et al., 2010,

2014) while a paleo-Iberian Poleward Current seems to have influenced the MD99-2331 site during H2a (Figure 1c; Salgueiro et al., 2014). Given that we considered particularly cold Heinrich events such as H6, the scenario that best applies to our data appears to be the influence of (sub)polar waters, although this possibility requires further investigation with more sediment cores covering a longer period than the last 35–40 kyrs.

6.3. Within-Site, Hemispheric, and Inter-Hemispheric Phase Relationships Between Paleothermometric Proxies

6.3.1. No Evidence of a Differential Bioturbation Effect on Paleothermometric Proxies

The measurements of the very same lipid extracts for the three cores strengthen our investigation of phase relationships between biomarker-based proxies. The phase relationships were assessed visually and quantified with cross-correlograms calculated after resampling on an even grid (every 10 years) prior to band-pass filtering. Our analysis supports nearly synchronous RI-OH′ and $U^{K'}_{37}$ responses to millennial climatic events, given the phase differences of less than one century (Figures 7a, 7c, and 7f). Conversely, TEX_{86} seems to lead RI-OH′ and $U^{K'}_{37}$ by roughly one century, especially during the 115–55 ka BP period (Figure 7f). Such phase relationships are apparent at all three Iberian Margin study sites, despite this being difficult to evaluate for cores MD99-2331 and MD95-2040, given their lower temporal resolutions (Figure 2).

Bioturbation may generate attenuation and phase differences between paleothermometric proxies, especially when relative changes in proxy-carrier abundances are contrasting (Bard, Arnold, Duprat, et al., 1987). We thus investigated the bioturbation effect on RI-OH′ and $U^{K'}_{37}$ during GS22 as an extreme case (Figure S13), given that C_{37} alkenone concentrations almost reach zero only during this Heinrich-like event for the 115–55 ka BP period (Figures 3c, 3f, and 3i). Using the bioturbation model by Bard, Arnold, Duprat, et al. (1987) and assuming a bioturbation depth of 10 cm, we were able to mimic the contrasting decreases between RI-OH′-SSTs and $U^{K'}_{37}$-SSTs from a single initial decrease in biomarker-based SSTs (Figures S13b and S13d; Section 6.1.2). However, the same bioturbation model makes RI-OH′ clearly lead $U^{K'}_{37}$ during GS22 (Figures S13c and S13d), a prominent phase difference which is absent in the real data (Figures S13a and S13b). A bioturbation depth of 3 cm or less would drastically reduce the RI-OH′ versus $U^{K'}_{37}$ asynchrony (Figures S13c and S13d). However, in that case, the simulated SST amplitude would be the same for RI-OH′ and $U^{K'}_{37}$ (Figure S13d). This shows that bioturbation coupled to carrier-abundance changes is not responsible for the observed difference in SST amplitude even for the extreme case of GS22 (Figure S13b). Similarly, the absence of a clear systematic phase difference between RI-OH′ and $U^{K'}_{37}$ during any of the Heinrich-like events, notably during GS22 characterized with the lowest alkenone concentrations, indicates that bioturbation coupled to proxy-carrier changes only has a small effect on paleothermometric proxies, at least for the Iberian Margin core MD95-2042.

Another possibility is that grain-size dependent bioturbation makes biomarker-based proxies lead foraminifer-based proxies (Bard, 2001). We thus also considered the core MD95-2042 planktic foraminifer $\delta^{18}O$ record for phase relationship analyses (Figure 7d; Shackleton et al., 2000). While planktic foraminifer $\delta^{18}O$ not only depends on SST but also on global seawater $\delta^{18}O$ and on local salinity, among other factors (see Malevich et al., 2019, and references therein for further details), we can reasonably assume that the millennial planktic foraminifer $\delta^{18}O$ variability reflects millennial SST changes. Visually, planktic foraminifer $\delta^{18}O$ responds almost synchronously with RI-OH′ and $U^{K'}_{37}$ to millennial climatic events (Figures 7a, 7c, and 7d). During the 146-50 and 115-55 ka BP periods, the RI-OH′ phase difference with planktic foraminifer $\delta^{18}O$ is of less than 100 years on average (Figures 7f and 7h), which we consider to be insignificant. In addition, planktic foraminifer $\delta^{18}O$ leads $U^{K'}_{37}$ by roughly 100–150 years on average (Figure 7h), a phase difference opposite to the theoretical effect of grain-size dependent bioturbation (Bard, 2001). The nearly synchronous biomarker-based and foraminifer-based proxy responses to millennial climatic events detract from the idea of grain-size dependent bioturbation for core MD95-2042 sediments.

Darfeuil et al. (2016) concluded that there is no clear evidence of biomarker lateral advection at the MD95-2042. However, one could also hypothesize a grain-size dependent bioturbation effect between organic paleothermometers (Bard, 2001). Indeed, Magill et al. (2018) hypothesized that organic carbon-rich fine particles (<6 μm) would carry alkenones (Pedrosa-Pàmies et al., 2015) while different, coarser particles

(6–32 μm) would carry archeal GDGTs (Mollenhauer et al., 2015; Park et al., 2014). Bard (2001) has shown that grain-size dependent bioturbation could make the fine fraction lead the coarse fraction and thus make alkenones lead archaeal GDGTs. However, this effect heavily depends on the sedimentation rate, which, in the case of core MD95-2042, shows a mean of 15 cm/kyr (n = 320, SD of 4 cm/kyr) during the 160-45 ka BP period. In addition, there is no quantification of the hypothetical difference in bioturbation parameters between alkenones and GDGTs. Assuming a ratio of two between bioturbation depths for alkenones and GDGTs, $U^{K'}_{37}$ would lead RI-OH′ and TEX_{86} by 72 years for events of roughly three millennia of duration in a section with the mean sedimentation rate of 15 cm/kyr (Bard, 2001). This theoretical phase difference is as small as the observed ones. Indeed, all biomarker concentrations as well as RI-OH′ and $U^{K'}_{37}$ have phase differences of less than one century (Figure 7g). Nevertheless, TEX_{86} slightly leads RI-OH′ and $U^{K'}_{37}$ by 140 years on average (Figure 7f), which is opposite to the hypothetical effect of bioturbation (Bard, 2001). Given the nearly synchronous biomarker concentration responses to millennial climatic events, there is no evidence that grain-size dependent bioturbation contributes to the observed phase relationships between core MD95-2042 organic paleothermometers.

Another effect of grain-size dependent bioturbation is differential smoothing, an issue that Bard (2001) found to be more serious than differential phase shift, especially for millennial events. With the mean sedimentation rate of 15 cm/kyr and an hypothetical ratio of two between bioturbation depths for the fractions carrying alkenones and GDGTs, a differential signal attenuation by roughly 13% would occur for $U^{K'}_{37}$ versus RI-OH′ and TEX_{86} for events of roughly three millennia of duration (Bard, 2001). However, the imperfect existing proxy-SST calibrations, especially for the novel RI-OH′ paleothermometer (Section 6.2.3) prevent us from properly evaluating grain-size dependent smoothing. A thorough assessment of grain-size dependent bioturbation with data on bioturbation parameters for the different biomarkers and with model simulations is beyond the scope of our study.

6.3.2. Relationship Between Iberian Margin SST Proxies and Greenland $\delta^{18}O$ and Temperature

Given their responses to Dansgaard-Oeschger events (Sections 5.1 and 6.1.1), RI-OH′ and $U^{K'}_{37}$ support a relationship between Iberian Margin SST and Greenland temperature (Figures 7a, 7c, and 7e; Kindler et al., 2014). Shackleton et al. (2000) were the first to demonstrate a relationship between core MD95-2042 and Greenland $\delta^{18}O$ ice core records using their planktic foraminifer $\delta^{18}O$ record (Figure 7d). However, raw $\delta^{18}O$ of ice does not only reflect local temperature, but also $\delta^{18}O$ of moisture source and sea water, local elevation, and upstream origin among other factors (e.g., Kindler et al., 2014; Stenni et al., 2010). The Greenland temperature record proposed by Kindler et al. (2014) and shown in Figure 7e thus relies on both $\delta^{18}O$ of ice and nitrogen isotopes entrapped in air bubbles. Our consideration of temperature rather than $\delta^{18}O$ of ice for Greenland and the nearly synchronous millennial variability between biomarker-based and foraminifer-based proxies (Section 6.3.1) strengthen the hemispheric relationship. The near synchronicity with $U^{K'}_{37}$ and planktic foraminifer $\delta^{18}O$ and hemispheric relationships further support the use of RI-OH′ as an organic paleothermometer in the Iberian Margin.

6.3.3. Phase Relationships During Four Heinrich-Like Events

We make a multiproxy analysis for core MD95-2042 focusing on four Heinrich-like events (GS25, GS24, GS22, and H5; Figure 8), when TEX_{86} most clearly leads RI-OH′ and $U^{K'}_{37}$ (Figures 7a–7c). We assume that $\delta^{18}O$ of planktic foraminifers (Figure 8b; Shackleton et al., 2000), RI-OH′ (Figure 8c), $U^{K'}_{37}$ (Figure 8d), and relative abundance of *B. tepikiense* dinocysts (Figure 8k; Eynaud et al., 2000) record SST changes. We follow the hypothesis of Shackleton et al. (2000) that their benthic foraminifer $\delta^{18}O$ record (Figure 8o) reflects bottom water temperature and ice volume changes. We consider XRF-%$CaCO_3$ (Figure 8f; Darfeuil et al., 2016), biomarker concentrations (Figures 8g–8i), and total organic carbon content (Figure 8j; Pailler & Bard, 2002) for primary productivity changes. For coarse grain occurrences and decreases in themohaline circulation speed related to Heinrich-like events, we use magnetic susceptibility (Figure 8m; Thouveny et al., 2000) and isotopic composition of carbon ($\delta^{13}C$) of benthic foraminifers (Figure 8n; Shackleton et al., 2000), respectively. We also complement the core MD95-2042 multiproxy analysis with air temperature records from Greenland (Figure 8a; Kindler et al., 2014) and Antarctica (Figure 8p; Jouzel et al., 2007) on our new chronology (Section 4.2).

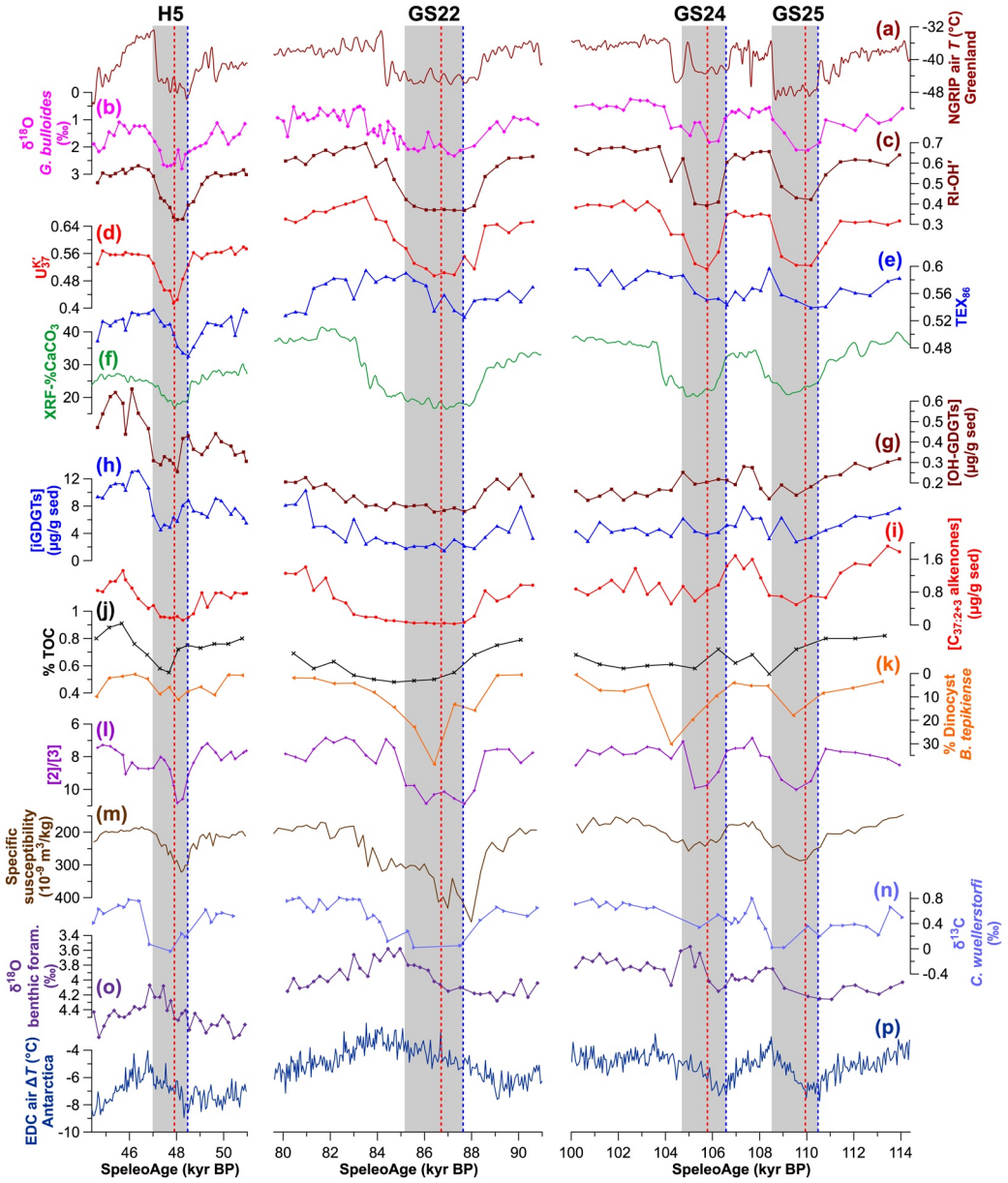

Figure 8. Phase relationships between Iberian Margin core MD95-2042 records and Greenland and Antarctic temperatures during H5, GS22, GS24, and GS25. (a) North Greenland Ice Core Project (NGRIP) air temperature (Kindler et al., 2014). (b) Isotopic composition of oxygen ($\delta^{18}O$) of *G. bulloides* tests (planktic foraminifers; Shackleton et al., 2000). (c) RI-OH′ (ring index of hydroxylated tetraethers; introduced by Lü et al., 2015; this study). (d) $U^{K'}_{37}$ (C_{37} ketone unsaturation ratio; introduced by Prahl & Wakeham, 1987; this study; Darfeuil et al., 2016). (e) TEX_{86} (TetraEther indeX of tetraethers consisting of 86 carbon atoms; introduced by Schouten et al., 2002; this study). (f) XRF-derived calcium carbonate ($CaCO_3$) content (Darfeuil et al., 2016). (g) Total OH-GDGT concentration (this study). (h) Total iGDGT concentration (this study). (i) Summed di-unsaturated and tri-unsaturated C_{37} alkenone concentration (this study; Darfeuil et al., 2016). (j) Total organic carbon content (Pailler & Bard, 2002). (k) Relative abundance of cold species *B. tepikense* dinocysts (Eynaud et al., 2000). (l) GDGT-2/GDGT-3 ([2]/[3]) ratio (introduced by Taylor et al., 2013; this study), with higher values reflecting increased deepwater *Thaumarchaeota* contributions to iGDGT signals (e.g., Besseling et al., 2019; Kim et al., 2015, 2016). (m) Specific susceptibility (Thouveny et al., 2000). (n) Isotopic composition of carbon ($\delta^{13}C$) of *C. wuellerstorfi* tests (benthic foraminifers; Shackleton et al., 2000) as an indicator of deep North Atlantic circulation intensity. (o) $\delta^{18}O$ of benthic foraminifers (Shackleton et al., 2000) as a surrogate of Antarctic temperature. (p) European Project for Ice Coring in Antarctica Dome C (EDC) air temperature anomaly (Jouzel et al., 2007). Note the reversed axes in (b), (k–m), and (o). Dashed red and blue lines indicate the timings of $U^{K'}_{37}$ and TEX_{86} minimum values, respectively. Gray bars indicate the timings of TEX_{86} increases during cold events. GDGT, glycerol dialkyl glycerol tetraether.

The constrasting TEX_{86} behaviors compared to other SST proxies during Heinrich-like events (Figures 8b–8e) suggest that TEX_{86} does not only reflect SST changes. Following several previous studies (e.g., Huguet et al., 2007; Kim et al., 2012; Lee et al., 2008; Lopes dos Santos et al., 2010; McClymont et al., 2012; Wang et al., 2019; Xing et al., 2015), we also consider the hypothesis that TEX_{86} records subsurface to deepwater temperature rather than SST changes during Heinrich-like events, which we further discuss in Section 6.3.4. Under the working hypotheses introduced above, we can describe the following scenario for each studied Heinrich-like event.

Heinrich-like events are characterized by peaks in coarse grain abundance (Figure 8m) and drastic decreases in thermohaline circulation strength (Figure 8n) and Greenland temperatures, Iberian Margin SSTs, and primary productivity (Figures 8a–8d and 8f–8k). When Heinrich-like events end, thermohaline circulation strength (Figure 8n) and Greenland temperatures, Iberian Margin SSTs, and primary productivity increase drastically (Figures 8a–8d and 8f–8k). Conversely, Antarctic and Iberian Margin subsurface to deepwater temperatures tend to decrease before Heinrich-like events, then increase progressively during Heinrich-like events before decreasing smoothly again when Heinrich-like events end (Figures 8e, 8o, and 8p).

Based on time offsets between organic proxy minima (time offsets between blue and red dashed lines in Figure 8), TEX_{86} leads RI-OH′ and $U^{K'}_{37}$ by roughly 500 years during GS25 and H5 and by roughly 1,000 years during GS24 and GS22. These time offsets are larger than the averaged temporal resolution of biomarker-based core MD95-2042 records (360 years).

6.3.4. Different Export Depths for iGDGTs and OH-GDGTs in the Iberian Margin?

The scenario depicted in Section 6.3.3 suggests a warming of North Atlantic subsurface to deep waters—broadly defined as being between 150 and 3,000 m water depth in this section—during Heinrich events, which would further support the idea that GS25, GS24, and GS22 are Heinrich-like events (Eynaud et al., 2000). Indeed, several modeling studies simulated a warming of North Atlantic subsurface to deep waters during cold climatic events with or without freshwater forcing, with different latitude domains and contrasting depth boundaries between surface and deep waters (e.g., Brady & Otto-Bliesner, 2011; Liu et al., 2009; Mignot et al., 2007; Pedro et al., 2018; Shaffer et al., 2004; Vettoretti & Peltier, 2015). Similarly, several foraminifer-based and biomarker-based records suggest a warming of North Atlantic subsurface to deep waters (Hernández-Almeida et al., 2015; Kim et al., 2012; Marcott et al., 2011; Rasmussen & Thomsen, 2004; Schmidt et al., 2012). Previous sediment core studies followed the working hypothesis that TEX_{86}^{H}, as well as TEX_{86}, records subsurface temperature rather than SST changes (Kim et al., 2012; Lopes dos Santos et al., 2010; McClymont et al., 2012), which seems reasonable for the Iberian Margin as well during Heinrich-like events, given the occurrence of Mediterranean deepwater *Thaumarchaeota* (Kim et al., 2016). Despite the Mediterranean deepwater *Thaumarchaeota* contributions to iGDGT signals, Kim et al. (2015) and Darfeuil et al. (2016) found good correlations between TEX_{86}^{H} and modern SST in Mediterranean Sea surface sediments at water depths >1,000 m and between TEX_{86} and $U^{K'}_{37}$ in core MD95-2042 sediments, respectively. However, the reasons for such SST-like TEX_{86} and TEX_{86}^{H} signals remain unclear. Indeed, we found better correlations between RI-OH′ and $U^{K'}_{37}$ than between RI-OH′ and TEX_{86} (Section 6.1.1) without clear evidence of OH-GDGTs from the Mediterranean Outflow Waters in Iberian Margin downcore sediments (Section 6.2.3).

Under the subsurface to deepwater warming hypothesis, we can tentatively explain why TEX_{86} leads RI-OH′ and $U^{K'}_{37}$ during Heinrich-like events. TEX_{86} (Figure 8e) and benthic foraminifer $\delta^{18}O$ (Figure 8o; Shackleton et al., 2000) resemble Antarctic temperatures (Figure 8p; Jouzel et al., 2007). Shackleton et al. (2000) proposed an inter-hemispheric relationship between their benthic foraminifer $\delta^{18}O$ record and Antarctic ice core records by suggesting that their isotopic record is a surrogate of Antarctic temperatures as a function of ice volume. Given that TEX_{86} also resembles benthic foraminifer $\delta^{18}O$ (Figures 8e, 8o, and 8p), these proxies suggest a relationship between core MD95-2042 subsurface and bottom water temperature records and Antarctic ice core records.

To assess deepwater *Thaumarchaeota* contributions to iGDGT signals, we use the GDGT-2/GDGT-3—herein (2)/(3)—ratio (Figure 8l, see also Data Set S3) following several previous studies (Dong et al., 2019; Hernández-Sánchez et al., 2014; Hertzberg et al., 2016; Jia et al., 2017; Kim et al., 2015; Taylor et al., 2013; Villanueva et al., 2015; Wei et al., 2020; Y. Wu et al., 2020). Indeed, we observe weak correlations between

(2)/(3) ratios and TEX_{86} values (r values between −0.33 and 0.13, with p values between 0.04 and 0.35 when taking serial correlation into account following Ebisuzaki, 1997) for the three Iberian Margin sediment cores (Figures S14a and S14b). In addition, the correlation between the (2)/(3) ratio and water depth ($r = 0.96$, $n = 31$, $p < 0.001$; Kim et al., 2016) is stronger than the one between the (2)/(3) ratio and annual SST ($r = 0.60$, $n = 31$, $p < 0.001$; Kim et al., 2016) for Iberian Margin surface sediments (Figures S14c and S14d). The correlation between the (2)/(3) ratio and water depth is linked to the occurrence of two *Thaumarchaeota* ecotypes, the "shallow water" one (roughly 200–500 m water depth) with low (2)/(3) ratios and the "deepwater" one (>1,000 m water depth) with high (2)/(3) ratios (Kim et al., 2016; Villanueva et al., 2015). During Heinrich-like events, (2)/(3) ratios increase from 7–8 to 10–11 (Figure 8l) synchronously with decreases in Iberian Margin SSTs (Figures 8b–8d) and in primary productivity (Figures 8f–8j), the (2)/(3) ratio increases being roughly 10 times larger than the 1σ analytical uncertainty of 0.263 determined as described in section 4.4. Higher (2)/(3) ratios are attributable to increased relative contributions of deepwater *Thaumarchaeota* to iGDGT signals (Dong et al., 2019; Hernández-Sánchez et al., 2014; Hertzberg et al., 2016; Jia et al., 2017; Taylor et al., 2013; Villanueva et al., 2015; Wei et al., 2020; Y. Wu et al., 2020), including iGDGT production by endemic archaea within the Mediterranean Outflow Waters and the deep Mediterranean Sea (Besseling et al., 2019; Kim et al., 2015, 2016). Before Heinrich-like events, our (2)/(3) ratios are close to those measured from core lipids in Iberian Margin surface sediments at water depths >1,800 m (mean of 8.6, SD of 0.8, $n = 4$; Kim et al., 2016). During Heinrich-like events, our (2)/(3) ratios get closer to those measured from intact polar lipids in Iberian Margin suspended matter between 500 and 1,600 m water depth (mean of 13.0, SD of 2.2, $n = 6$; Kim et al., 2016), which carries iGDGTs within the Mediterranean Outflow Waters. Therefore, our (2)/(3) ratios further suggest that TEX_{86} records subsurface to deepwater temperature rather than SST changes in the Iberian Margin, especially during Heinrich-like events.

Assuming subsurface to deepwater warming and primary productivity reduction during Heinrich-like events, one hypothetical mechanism behind TEX_{86} signals could be a superposition of two fluxes from different water depths with two contrasting temperature signals (Figure 9). On one hand, a background flux from deep waters would generate Antarctic-like temperature signals (horizontal line and sinusoidal curve in Figure 9) for TEX_{86} but not RI-OH′ and $U^{K'}_{37}$. On the other hand, primary productivity dependent fluxes from surface waters would generate Greenland-like temperature signals (on-off curves in Figure 9) for all organic paleothermometers, notably RI-OH′ and $U^{K'}_{37}$. During Heinrich-like events, the background flux from deep waters would have an increased contribution to TEX_{86} signals, in relative terms, so that they better resemble Antarctic temperatures (Figure 9). Several studies support our idealized phase relationship between Greenland and Antarctic temperatures at the millennial scale (e.g., Barker et al., 2011; Schmittner et al., 2003). Higher (2)/(3) ratios related to increased deepwater *Thaumarchaeota* contributions to TEX_{86} signals during Heinrich-like events (Figure 8l) strengthen our hypothetical model, which should be further supported with regional model simulations in the future.

One shortcoming for the subsurface to deepwater warming scenario is that TEX_{86} does not lead RI-OH′ and $U^{K'}_{37}$ during all Heinrich-like events in the Iberian Margin, which suggests complicated TEX_{86} signals (Figures 7a–7c). Indeed, TEX_{86} seems to lead $U^{K'}_{37}$ during only a few MIS 3 Heinrich events at the Iberian Margin MD95-2042 site (Darfeuil et al., 2016). Conversely, Kim et al. (2012) observed an anti-phase relationship between Greenland $\delta^{18}O$ ice core records and their TEX_{86}^{H}-derived subsurface temperature record in the tropical Northeast Atlantic during MIS 3. Such contrasting results have several possible explanations. First, subsurface to deepwater warming concerns waters deeper than roughly 400–1,000 m at latitudes between 20°N and 40°N and waters deeper than roughly 100–400 m at latitudes >40°N in the North Atlantic (Brady & Otto-Bliesner, 2011; Liu et al., 2009; Vettoretti & Peltier, 2015). Based on the cited studies, subsurface to deepwater warming would not systematically affect TEX_{86} in the southern Iberian Margin, where core MD95-2042 is located. Second, climatic responses to freshwater forcing depend on climatic background (Dome Fuji Ice Core Project Members, 2017; Kageyama et al., 2010; Swingedouw et al., 2009; Zhang & Prange, 2020), which is warmer for MIS 5 than for MIS 3 (e.g., Jouzel et al., 2007; Kindler et al., 2014; Martrat et al., 2007; Pailler & Bard, 2002). Third, decreased duration of non-Heinrich stadials during MIS 3 compared to MIS 5 (Buizert & Schmittner, 2015) is associated with increased fluxes and sedimentation rates (Pailler & Bard, 2002), and thus weakened bioturbation effects (Bard, Arnold, Duprat, et al., 1987; Bard, 2001). The shorter non-Heinrich stadials may thus complicate the detection of any phase difference between $U^{K'}_{37}$ and TEX_{86} during MIS 3 at the MD95-2042 site. Whatever the reason(s) for the variable phase

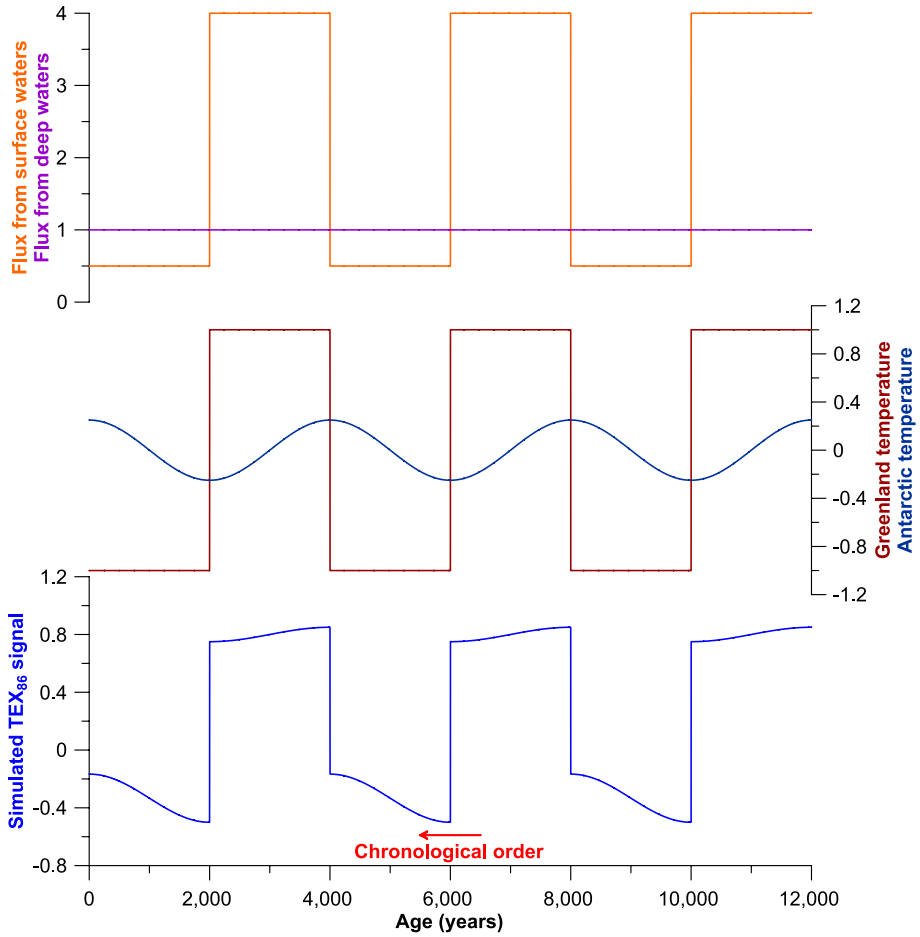

Figure 9. Hypothetic schematic of TEX_{86} signals generated with background fluxes from deep waters associated with primary productivity dependent fluxes from surface waters. TEX_{86} signals (blue curve) are simulated with a convolution of Greenland (dark red on-off curve) and Antarctic temperature (dark blue sinusoidal curve) with fluxes from surface (orange on-off curve) and deep waters (purple horizontal line). Observations of positive correlations for a lead of Antarctic over Greenland temperatures by roughly 1,000 years at the millennial scale support the assumed phase relationships between synthetic temperature records (e.g., Barker et al., 2011; Schmittner et al., 2003).

relationships, we cannot exclude the hypothesis that TEX_{86} reflects subsurface to deepwater temperature during Heinrich-like events, as millennial decreases in TEX_{86}^{H}-SSTs are limited compared to those in RI-OH′-SSTs and $U^{K'}_{37}$-SSTs (Figure 5).

Alternatively, TEX_{86} would resemble Antarctic temperatures only when Mediterranean waters containing iGDGTs mix with Antarctic waters, which is the case for the present time (Cabeçadas et al., 2002, 2003, 2010; Louarn & Morin, 2011). The Antarctic Intermediate Waters (presently between 500–600 and 1,500 m water depth; Figure 1c) advanced into the Gulf of Cadiz, and thus potentially into the Iberian Margin as well, during MIS 3 Heinrich events (Dubois-Dauphin et al., 2016; Montero-Serrano et al., 2011). In addition, the upper Mediterranean Outflow Waters (presently at 500–700 m water depth) had the strongest influence during MIS 5e and MIS 1, strengthened during MIS 5 Heinrich-like events but either weakened or disappeared during MIS 3 in the Gulf of Cadiz (Kaboth et al., 2016). However, the findings of Montero-Serrano et al. (2011) and Dubois-Dauphin et al. (2016) for MIS 3 Heinrich events are not necessarily generalizable to MIS 5 Heinrich-like events. In addition, relationships between TEX_{86} and Antarctic signals could be fortuitous despite transit times at water depths of 2–3 km of roughly 200–400 years (Gebbie & Huybers, 2012; Holzer & Primeau, 2010), which is similar to the averaged temporal resolutions of foraminifer-based and biomarker-based core MD95-2042 records. Despite the complicated TEX_{86} signals, all the most parsimonious scenarios rely on different export depths for iGDGTs and OH-GDGTs in the Iberian Margin.

7. Conclusions and Perspectives

Our new high-resolution temperature records over the 160-45 ka BP period from three deep sea sediment cores located in a north-south transect along the Iberian Margin validate the novel RI-OH′ paleothermometer based on several arguments. First, RI-OH′ records characteristic North Atlantic climatic events in the same way as does the established $U^{K'}_{37}$ SST proxy, whereas TEX_{86} leads RI-OH′ and $U^{K'}_{37}$ during four Heinrich-like events. Second, RI-OH′ gives realistic SSTs and latitudinal gradients consistent with those from independent paleothermometers. Third, relationships with Greenland temperatures and the hypothesis that background subsurface fluxes drive TEX_{86} but not RI-OH′ and $U^{K'}_{37}$ during Heinrich-like events further validate the use of RI-OH′ as an SST proxy. Overall, our study suggests that RI-OH′ may nicely complement $U^{K'}_{37}$ to investigate North Atlantic paleoclimates.

While our findings are promising for RI-OH′, they also highlight the need for a more extensive RI-OH′-SST core top calibration for the North Atlantic. To better explain why RI-OH′ better resembles $U^{K'}_{37}$ than TEX_{86} and why Mediterranean deep water-derived OH-GDGTs seem absent in the Iberian Margin, one possibility could be to extend previous lipidomic and genetic investigations in the Iberian Margin and the Mediterranean Sea to OH-GDGTs. Our findings thus support further scrutiny of OH-GDGT-based paleothermometry with multiproxy core top, downcore, and sediment trap studies, source to sink investigations, culture experiments, and further constraints on OH-GDGT biological producers.

Data Availability Statement

Cores MD99–2331, MD95–2040, and MD95–2042 biomarker data generated for this study (Data Sets S1–S3) are available at Zenodo (https://doi.org/10.5281/zenodo.4279890; Davtian et al., 2020) and in the public repository PANGAEA® (https://doi.pangaea.de/10.1594/PANGAEA.927657). Core MD95-2042 cross-correlation results are provided in Data Set S4.

Acknowledgments
Work at CEREGE is supported by the Collège de France and BNP-Paribas Foundation (project CPATEMP). N. Davtian expresses her thanks to the Collège de France for providing postdoctoral salary support. S. Darfeuil thanks the Ecole Normale Supérieure de Lyon for providing PhD salary support. The authors thank Yoann Fagault for analytical support in the laboratory. The authors thank Kazuyo Tachikawa and Marta Garcia for their help with the XRF analyses. The authors are grateful to the Associate Editor and two anonymous reviewers for their comments which contributed to improve this study. This work was supported by the IMAGES program that funded the coring of the studied sedimentary archives.

References

Allaart, L., Müller, J., Schomacker, A., Rydningen, T. A., Håkansson, L., Kjellman, S. E., et al. (2020). Late Quaternary glacier and sea-ice history of northern Wijdefjorden, Svalbard. *Boreas*, *49*(3), 417–437. https://doi.org/10.1111/bor.12435

Ambar, I. (1983). A shallow core of Mediterranean water off western Portugal. Deep sea research part A. *Oceanographic Research Papers*, *30*(6), 677–680. https://doi.org/10.1016/0198-0149(83)90045-6

Ambar, I., Serra, N., Brogueira, M. J., Cabeçadas, G., Abrantes, F., Freitas, P., et al. (2002). Physical, chemical and sedimentological aspects of the Mediterranean outflow off Iberia. *Deep Sea Research Part II: Topical Studies in Oceanography*, *49*(19), 4163–4177. https://doi.org/10.1016/S0967-0645(02)00148-0

Arístegui, J., Barton, E. D., Álvarez-Salgado, X. A., Santos, A. M. P., Figueiras, F. G., Kifani, S., et al. (2009). Sub-regional ecosystem variability in the Canary Current upwelling. *Progress in Oceanography*, *83*(1), 33–48. https://doi.org/10.1016/j.pocean.2009.07.031

Ausín, B., Hodell, D. A., Cutmore, A., & Eglinton, T. I. (2020). The impact of abrupt deglacial climate variability on productivity and upwelling on the southwestern Iberian margin. *Quaternary Science Reviews*, *230*, 106139. https://doi.org/10.1016/j.quascirev.2019.106139

Ausín, B., Magill, C., Haghipour, N., Fernández, Á., Wacker, L., Hodell, D., et al. (2019). (In)coherent multiproxy signals in marine sediments: Implications for high-resolution paleoclimate reconstruction. *Earth and Planetary Science Letters*, *515*, 38–46. https://doi.org/10.1016/j.epsl.2019.03.003

Baddouh, M., Meyers, S. R., Carroll, A. R., Beard, B. L., & Johnson, C. M. (2016). Lacustrine $^{87}Sr/^{86}Sr$ as a tracer to reconstruct Milankovitch forcing of the Eocene hydrologic cycle. *Earth and Planetary Science Letters*, *448*, 62–68. https://doi.org/10.1016/j.epsl.2016.05.007

Bard, E. (2001). Paleoceanographic implications of the difference in deep-sea sediment mixing between large and fine particles. *Paleoceanography*, *16*(3), 235–239. https://doi.org/10.1029/2000PA000537

Bard, E., Arnold, M., Duprat, J., Moyes, J., & Duplessy, J.-C. (1987). Reconstruction of the last deglaciation: Deconvolved records of $\delta^{18}O$ profiles, micropaleontological variations and accelerator mass spectrometric ^{14}C dating. *Climate Dynamics*, *1*(2), 101–112. https://doi.org/10.1007/BF01054479

Bard, E., Arnold, M., Maurice, P., Duprat, J., Moyes, J., & Duplessy, J.-C. (1987). Retreat velocity of the north Atlantic polar front during the last deglaciation determined by ^{14}C accelerator mass spectrometry. *Nature*, *328*(6133), 791–794. https://doi.org/10.1038/328791a0

Bard, E., Rostek, F., Turon, J.-L., & Gendreau, S. (2000). Hydrological impact of Heinrich events in the subtropical northeast Atlantic. *Science*, *289*(5483), 1321–1324. https://doi.org/10.1126/science.289.5483.1321

Baringer, M. O., & Price, J. F. (1997). Mixing and spreading of the Mediterranean outflow. *Journal of Physical Oceanography*, *27*(8), 1654–1677. https://doi.org/10.1175/1520-0485(1997)027<1654:MASOTM>2.0.CO;2

Barker, S., Knorr, G., Edwards, R. L., Parrenin, F., Putnam, A. E., Skinner, L. C., et al. (2011). 800,000 years of abrupt climate variability. *Science*, *334*(6054), 347–351. https://doi.org/10.1126/science.1203580

Basse, A., Zhu, C., Versteegh, G. J. M., Fischer, G., Hinrichs, K.-U., & Mollenhauer, G. (2014). Distribution of intact and core tetraether lipids in water column profiles of suspended particulate matter off Cape Blanc, NW Africa. *Organic Geochemistry*, *72*, 1–13. https://doi.org/10.1016/j.orggeochem.2014.04.007

Bassinot, F. C., & Labeyrie, L. D. (1996). *Images I, MD101: A coring cruise of the R/V marion Dufresne in the north Atlantic Ocean and Norwegian sea (PANGAEA documentation)*. PANGAEA. Retrieved from https://epic.awi.de/id/eprint/29874/

Bazin, L., Landais, A., Lemieux-Dudon, B., Toyé Mahamadou Kele, H., Veres, D., Parrenin, F., et al. (2013). An optimized multi-proxy, multi-site Antarctic ice and gas orbital chronology (AICC2012): 120–800 ka. *Climate of the Past*, *9*(4), 1715–1731. https://doi.org/10.5194/cp-9-1715-2013

Benthien, A., & Müller, P. J. (2000). Anomalously low alkenone temperatures caused by lateral particle and sediment transport in the Malvinas Current region, western Argentine Basin. *Deep Sea Research Part I: Oceanographic Research Papers*, *47*(12), 2369–2393. https://doi.org/10.1016/S0967-0637(00)00030-3

Besseling, M. A., Hopmans, E. C., Bale, N. J., Schouten, S., Sinninghe Damsté, J. S., & Villanueva, L. (2020). The absence of intact polar lipid-derived GDGTs in marine waters dominated by Marine Group II: Implications for lipid biosynthesis in Archaea. *Scientific Reports*, *10*, 294. https://doi.org/10.1038/s41598-019-57035-0

Besseling, M. A., Hopmans, E. C., Koenen, M., van der Meer, M. T. J., Vreugdenhil, S., Schouten, S., et al. (2019). Depth-related differences in archaeal populations impact the isoprenoid tetraether lipid composition of the Mediterranean Sea water column. *Organic Geochemistry*, *135*, 16–31. https://doi.org/10.1016/j.orggeochem.2019.06.008

Blaga, C. I., Reichart, G.-J., Heiri, O., & Sinninghe Damsté, J. S. (2009). Tetraether membrane lipid distributions in water-column particulate matter and sediments: A study of 47 European lakes along a north-south transect. *Journal of Paleolimnology*, *41*(3), 523–540. https://doi.org/10.1007/s10933-008-9242-2

Bond, G. C., Heinrich, H., Broecker, W., Labeyrie, L. D., McManus, J., Andrews, J., et al. (1992). Evidence for massive discharges of icebergs into the North Atlantic Ocean during the last glacial period. *Nature*, *360*(6401), 245–249. https://doi.org/10.1038/360245a0

Bond, G. C., & Lotti, R. (1995). Iceberg discharges into the North Atlantic on millennial time scales during the last glaciation. *Science*, *267*(5200), 1005–1010. https://doi.org/10.1126/science.267.5200.1005

Brady, E. C., & Otto-Bliesner, B. L. (2011). The role of meltwater-induced subsurface ocean warming in regulating the Atlantic meridional overturning in glacial climate simulations. *Climate Dynamics*, *37*(7), 1517–1532. https://doi.org/10.1007/s00382-010-0925-9

Brassell, S. C., Eglinton, G., Marlowe, I. T., Pflaumann, U., & Sarnthein, M. (1986). Molecular stratigraphy: A new tool for climatic assessment. *Nature*, *320*(6058), 129–133. https://doi.org/10.1038/320129a0

Buizert, C., Cuffey, K. M., Severinghaus, J. P., Baggenstos, D., Fudge, T. J., Steig, E. J., et al. (2015). The WAIS Divide deep ice core WD2014 chronology—Part 1: Methane synchronization (68–31 ka BP) and the gas age-ice age difference. *Climate of the Past*, *11*(2), 153–173. https://doi.org/10.5194/cp-11-153-2015

Buizert, C., & Schmittner, A. (2015). Southern Ocean control of glacial AMOC stability and Dansgaard-Oeschger interstadial duration. *Paleoceanography*, *30*(12), 1595–1612. https://doi.org/10.1002/2015PA002795@10.1002/(ISSN)1944-9186.WAISDIV

Cabeçadas, G., Brogueira, M. J., & Gonçalves, C. (2003). Intermediate water masses off south-southwest Portugal: Chemical tracers. *Journal of Marine Research*, *61*(4), 539–552. https://doi.org/10.1357/002224003322384924

Cabeçadas, G., José Brogueira, M., & Gonçalves, C. (2002). The chemistry of Mediterranean outflow and its interactions with surrounding waters. *Deep Sea Research Part II: Topical Studies in Oceanography*, *49*(19), 4263–4270. https://doi.org/10.1016/S0967-0645(02)00154-6

Cabeçadas, G., José Brogueira, M., Gelena Cavaco, M., & Gonçalves, C. (2010). Chemical signature of intermediate water masses along western Portuguese margin. *Journal of Oceanography*, *66*(2), 201–210. https://doi.org/10.1007/s10872-010-0018-8

Casey, K. S., Brandon, T. B., Cornillon, P., & Evans, R. (2010). The past, present, and future of the AVHRR Pathfinder SST program. In V. Barale, J. F. R. Gower, & L. Alberotanza (Eds.), *Oceanography from space: Revisited* (pp. 273–287). Springer. https://doi.org/10.1007/978-90-481-8681-5_16

Castañeda, I. S., Schefuß, E., Pätzold, J., Sinninghe Damsté, J. S., Weldeab, S., & Schouten, S. (2010). Millennial-scale sea surface temperature changes in the eastern Mediterranean (Nile River Delta region) over the last 27,000 years. *Paleoceanography*, *25*(1), PA1208. https://doi.org/10.1029/2009PA001740

Cayre, O., Lancelot, Y., Vincent, E., & Hall, M. A. (1999). Paleoceanographic reconstructions from planktonic foraminifera off the Iberian Margin: Temperature, salinity, and Heinrich events. *Paleoceanography*, *14*(3), 384–396. https://doi.org/10.1029/1998PA900027

Ceccopieri, M., Carreira, R. S., Wagener, A. L. R., Hefter, J. H., & Mollenhauer, G. (2018). On the application of alkenone- and GDGT-based temperature proxies in the south-eastern Brazilian continental margin. *Organic Geochemistry*, *126*, 43–56. https://doi.org/10.1016/j.orggeochem.2018.10.009

Chen, W., Mohtadi, M., Schefuß, E., & Mollenhauer, G. (2014). Organic-geochemical proxies of sea surface temperature in surface sediments of the tropical eastern Indian Ocean. *Deep Sea Research Part I: Oceanographic Research Papers*, *88*, 17–29. https://doi.org/10.1016/j.dsr.2014.03.005

Chen, W., Mohtadi, M., Schefuß, E., & Mollenhauer, G. (2016). Concentrations and abundance ratios of long-chain alkenones and glycerol dialkyl glycerol tetraethers in sinking particles south of Java. *Deep Sea Research Part I: Oceanographic Research Papers*, *112*, 14–24. https://doi.org/10.1016/j.dsr.2016.02.010

Chen, Z., Li, J., Li, X., Chen, S., Dasgupta, S., Bai, S., et al. (2020). Characteristics and implications of isoprenoid and hydroxy tetraether lipids in hadal sediments of Mariana and Yap Trenches. *Chemical Geology*, *551*, 119742. https://doi.org/10.1016/j.chemgeo.2020.119742

Cheng, H., Edwards, R. L., Sinha, A., Spötl, C., Yi, L., Chen, S., et al. (2016). The Asian monsoon over the past 640,000 years and ice age terminations. *Nature*, *534*(7609), 640–646. https://doi.org/10.1038/nature18591

Conte, M. H., Sicre, M.-A., Rühlemann, C., Weber, J. C., Schulte, S., Schulz-Bull, D., & Blanz, T. (2006). Global temperature calibration of the alkenone unsaturation index ($U^{K'}_{37}$) in surface waters and comparison with surface sediments. *Geochemistry, Geophysics, Geosystems*, *7*(2), Q02005. https://doi.org/10.1029/2005GC001054

Crameri, F. (2018a). Geodynamic diagnostics, scientific visualisation and StagLab 3.0. *Geoscientific Model Development*, *11*(6), 2541–2562. https://doi.org/10.5194/gmd-11-2541-2018

Crameri, F. (2018b). *Scientific colour-maps*. Zenodo. Retrieved from https://doi.org/10.5281/zenodo.1287763

Cuffey, K. M., Clow, G. D., Alley, R. B., Stuiver, M., Waddington, E. D., & Saltus, R. W. (1995). Large Arctic temperature change at the Wisconsin-Holocene glacial transition. *Science*, *270*(5235), 455–458. https://doi.org/10.1126/science.270.5235.455

Dansgaard, W., Johnsen, S. J., Clausen, H. B., Dahl-Jensen, D., Gundestrup, N. S., Hammer, C. U., et al. (1993). Evidence for general instability of past climate from a 250-kyr ice-core record. *Nature*, *364*(6434), 218–220. https://doi.org/10.1038/364218a0

Darfeuil, S., Ménot, G., Giraud, X., Rostek, F., Tachikawa, K., Garcia, M., & Bard, E. (2016). Sea surface temperature reconstructions over the last 70 kyr off Portugal: Biomarker data and regional modeling. *Paleoceanography*, *31*(1), 40–65. https://doi.org/10.1002/2015PA002831

Datema, M., Sangiorgi, F., Vernal, A., deReichart, G.-J., Lourens, L. J., & Sluijs, A. (2019). Millennial-scale climate variability and dinoflagellate-cyst-based seasonality changes over the last 150 kyrs at "Shackleton Site" U1385. *Paleoceanography and Paleoclimatology*, *34*(7), 1139–1156. https://doi.org/10.1029/2018PA003497

Davtian, N., Bard, E., Darfeuil, S., Ménot, G., & Rostek, F. (2020). *Biomarker indices and concentrations and biomarker-based temperature estimates from Iberian Margin cores MD99-2331, MD95-2040 and MD95-2042 (160–45 ka BP) [Data set]*. Zenodo. Retrieved from https://doi.org/10.5281/zenodo.4279890

Davtian, N., Bard, E., Ménot, G., & Fagault, Y. (2018). The importance of mass accuracy in selected ion monitoring analysis of branched and isoprenoid tetraethers. *Organic Geochemistry*, *118*, 58–62. https://doi.org/10.1016/j.orggeochem.2018.01.007

Davtian, N., Ménot, G., Fagault, Y., & Bard, E. (2019). Western Mediterranean Sea paleothermometry over the last glacial cycle based on the novel RI-OH Index. *Paleoceanography and Paleoclimatology*, *34*(4), 616–634. https://doi.org/10.1029/2018PA003452

de Abreu, L., Shackleton, N. J., Schönfeld, J., Hall, M. A., & Chapman, M. R. (2003). Millennial-scale oceanic climate variability off the Western Iberian margin during the last two glacial periods. *Marine Geology*, *196*(1–2), 1–20. https://doi.org/10.1016/S0025-3227(03)00046-X

de Bar, M. W., Rampen, S. W., Hopmans, E. C., Sinninghe Damsté, J. S., & Schouten, S. (2019). Constraining the applicability of organic paleotemperature proxies for the last 90 Myrs. *Organic Geochemistry*, *128*, 122–136. https://doi.org/10.1016/j.orggeochem.2018.12.005

de Bar, M. W., Stolwijk, D. J., McManus, J. F., Sinninghe Damsté, J. S., & Schouten, S. (2018). A Late Quaternary climate record based on long-chain diol proxies from the Chilean margin. *Climate of the Past*, *14*(11), 1783–1803. https://doi.org/10.5194/cp-14-1783-2018

Dome Fuji Ice Core Project Members (2017). State dependence of climatic instability over the past 720,000 years from Antarctic ice cores and climate modeling. *Science Advances*, *3*(2), e1600446. https://doi.org/10.1126/sciadv.1600446

Dong, L., Li, Z., & Jia, G. (2019). Archaeal ammonia oxidation plays a part in late Quaternary nitrogen cycling in the south China Sea. *Earth and Planetary Science Letters*, *509*, 38–46. https://doi.org/10.1016/j.epsl.2018.12.023

Dubois-Dauphin, Q., Bonneau, L., Colin, C., Montero-Serrano, J.-C., Montagna, P., Blamart, D., et al. (2016). South Atlantic intermediate water advances into the North-east Atlantic with reduced Atlantic meridional overturning circulation during the last glacial period. *Geochemistry, Geophysics, Geosystems*, *17*(6), 2336–2353. https://doi.org/10.1002/2016GC006281

Ebisuzaki, W. (1997). A method to estimate the statistical significance of a correlation when the data are serially correlated. *Journal of Climate*, *10*(9), 2147–2153. https://doi.org/10.1175/1520-0442(1997)010<2147:AMTETS>2.0.CO;2

Elling, F. J., Gottschalk, J., Doeana, K. D., Kusch, S., Hurley, S. J., & Pearson, A. (2019). Archaeal lipid biomarker constraints on the Paleocene-Eocene carbon isotope excursion. *Nature Communications*, *10*(1), 4519. https://doi.org/10.1038/s41467-019-12553-3

Elling, F. J., Könneke, M., Lipp, J. S., Becker, K. W., Gagen, E. J., & Hinrichs, K.-U. (2014). Effects of growth phase on the membrane lipid composition of the thaumarchaeon *Nitrosopumilus maritimus* and their implications for archaeal lipid distributions in the marine environment. *Geochimica et Cosmochimica Acta*, *141*, 579–597. https://doi.org/10.1016/j.gca.2014.07.005

Elling, F. J., Könneke, M., Mußmann, M., Greve, A., & Hinrichs, K.-U. (2015). Influence of temperature, pH, and salinity on membrane lipid composition and TEX_{86} of marine planktonic thaumarchaeal isolates. *Geochimica et Cosmochimica Acta*, *171*, 238–255. https://doi.org/10.1016/j.gca.2015.09.004

Elling, F. J., Könneke, M., Nicol, G. W., Stieglmeier, M., Bayer, B., Spieck, E., et al. (2017). Chemotaxonomic characterisation of the thaumarchaeal lipidome. *Environmental Microbiology*, *19*(7), 2681–2700. https://doi.org/10.1111/1462-2920.13759

Emiliani, C. (1957). Temperature and age analysis of deep-sea cores. *Science*, *125*(3244), 383–387. https://doi.org/10.1126/science.125.3244.383

Emiliani, C. (1966). Isotopic paleotemperatures. *Science*, *154*(3751), 851–857. https://doi.org/10.1126/science.154.3751.851

EPICA Community Members (2004). Eight glacial cycles from an Antarctic ice core. *Nature*, *429*(6992), 623–628. https://doi.org/10.1038/nature02599

Epstein, B. L., D'Hondt, S., Quinn, J. G., Zhang, J., & Hargraves, P. E. (1998). An effect of dissolved nutrient concentrations on alkenone-based temperature estimates. *Paleoceanography*, *13*(2), 122–126. https://doi.org/10.1029/97PA03358

Evans, T. W., Könneke, M., Lipp, J. S., Adhikari, R. R., Taubner, H., Elvert, M., & Hinrichs, K.-U. (2018). Lipid biosynthesis of *Nitrosopumilus maritimus* dissected by lipid specific radioisotope probing (lipid-RIP) under contrasting ammonium supply. *Geochimica et Cosmochimica Acta*, *242*, 51–63. https://doi.org/10.1016/j.gca.2018.09.001

Eynaud, F., de Abreu, L., Voelker, A., Schönfeld, J., Salgueiro, E., Turon, J.-L., et al. (2009). Position of the polar front along the western Iberian margin during key cold episodes of the last 45 ka. *Geochemistry, Geophysics, Geosystems*, *10*(7). https://doi.org/10.1029/2009GC002398

Eynaud, F., Turon, J. L., Sánchez-Goñi, M. F., & Gendreau, S. (2000). Dinoflagellate cyst evidence of "Heinrich-like events" off Portugal during the marine isotopic stage 5. *Marine Micropaleontology*, *40*(1), 9–21. https://doi.org/10.1016/S0377-8398(99)00045-6

Fietz, S., Ho, S. L., & Huguet, C. (2020). Archaeal membrane lipid-based paleothermometry for applications in polar oceans. *Oceanography*, *33*(2), 104–114. https://doi.org/10.5670/oceanog.2020.207

Fietz, S., Ho, S. L., Huguet, C., Rosell-Melé, A., & Martínez-García, A. (2016). Appraising GDGT-based seawater temperature indices in the Southern Ocean. *Organic Geochemistry*, *102*, 93–105. https://doi.org/10.1016/j.orggeochem.2016.10.003

Fietz, S., Huguet, C., Rueda, G., Hambach, B., & Rosell-Melé, A. (2013). Hydroxylated isoprenoidal GDGTs in the Nordic Seas. *Marine Chemistry*, *152*, 1–10. https://doi.org/10.1016/j.marchem.2013.02.007

Fiúza, A. F. G., de Macedo, M. E., & Guerreiro, M. R. (1982). Climatological space and time-variation of the portuguese coastal upwelling. *Oceanologica Acta*, *5*(1), 31–40.

Fiúza, A. F. G., Hamann, M., Ambar, I., Diaz del Rio, G., González, N., & Cabanas, J. M. (1998). Water masses and their circulation off western Iberia during May 1993. *Deep Sea Research Part I: Oceanographic Research Papers*, *45*(7), 1127–1160. https://doi.org/10.1016/S0967-0637(98)00008-9

Galand, P. E., Gutiérrez-Provecho, C., Massana, R., Gasol, J. M., & Casamayor, E. O. (2010). Inter-annual recurrence of archaeal assemblages in the coastal NW Mediterranean Sea (Blanes bay microbial observatory). *Limnology & Oceanography*, *55*(5), 2117–2125. https://doi.org/10.4319/lo.2010.55.5.2117

Gebbie, G., & Huybers, P. (2012). The mean age of ocean waters inferred from radiocarbon observations: Sensitivity to surface sources and accounting for mixing histories. *Journal of Physical Oceanography*, *42*(2), 291–305. https://doi.org/10.1175/JPO-D-11-043.1

Gouzy, A., Malaizé, B., Pujol, C., & Charlier, K. (2004). Climatic "pause" during Termination II identified in shallow and intermediate waters off the Iberian margin. *Quaternary Science Reviews*, *23*(14), 1523–1528. https://doi.org/10.1016/j.quascirev.2004.03.002

Grootes, P. M., Stuiver, M., White, J. W. C., Johnsen, S., & Jouzel, J. (1993). Comparison of oxygen isotope records from the GISP2 and GRIP Greenland ice cores. *Nature*, *366*(6455), 552–554. https://doi.org/10.1038/366552a0

Haynes, R., & Barton, E. D. (1990). A poleward flow along the Atlantic coast of the Iberian Peninsula. *Journal of Geophysical Research*, *95*(C7), 11425–11441. https://doi.org/10.1029/JC095iC07p11425

Heinrich, H. (1988). Origin and consequences of cyclic ice rafting in the northeast Atlantic Ocean during the past 130,000 years. *Quaternary Research*, *29*(2), 142–152. https://doi.org/10.1016/0033-5894(88)90057-9

Herfort, L., Schouten, S., Abbas, B., Veldhuis, M. J. W., Coolen, M. J. L., Wuchter, C., et al. (2007). Variations in spatial and temporal distribution of Archaea in the North Sea in relation to environmental variables. *FEMS Microbiology Ecology*, *62*(3), 242–257. https://doi.org/10.1111/j.1574-6941.2007.00397.x

Herfort, L., Schouten, S., Boon, J. P., & Sinninghe Damsté, J. S. (2006). Application of the TEX_{86} temperature proxy to the southern North Sea. *Organic Geochemistry*, *37*(12), 1715–1726. https://doi.org/10.1016/j.orggeochem.2006.07.021

Hernández-Almeida, I., Sierro, F.-J., Cacho, I., & Flores, J.-A. (2015). Subsurface North Atlantic warming as a trigger of rapid cooling events: Evidence from the early Pleistocene (MIS 31–19). *Climate of the Past*, *11*(4), 687–696. https://doi.org/10.5194/cp-11-687-2015

Hernández-Sánchez, M. T., Woodward, E. M. S., Taylor, K. W. R., Henderson, G. M., & Pancost, R. D. (2014). Variations in GDGT distributions through the water column in the South East Atlantic Ocean. *Geochimica et Cosmochimica Acta*, *132*, 337–348. https://doi.org/10.1016/j.gca.2014.02.009

Herndl, G. J., Reinthaler, T., Teira, E., van Aken, H., Veth, C., Pernthaler, A., & Pernthaler, J. (2005). Contribution of Archaea to total prokaryotic production in the deep Atlantic Ocean. *Applied and Environmental Microbiology*, *71*(5), 2303–2309. https://doi.org/10.1128/AEM.71.5.2303-2309.2005

Hertzberg, J. E., Schmidt, M. W., Bianchi, T. S., Smith, R. W., Shields, M. R., & Marcantonio, F. (2016). Comparison of eastern tropical Pacific TEX_{86} and *Globigerinoides ruber* Mg/Ca derived sea surface temperatures: Insights from the Holocene and last glacial maximum. *Earth and Planetary Science Letters*, *434*, 320–332. https://doi.org/10.1016/j.epsl.2015.11.050

Hodell, D. A., Crowhurst, S., Skinner, L., Tzedakis, P. C., Margari, V., Channell, J. E. T., et al. (2013). Response of Iberian Margin sediments to orbital and suborbital forcing over the past 420 ka. *Paleoceanography*, *28*(1), 185–199. https://doi.org/10.1002/palo.20017

Hollis, C. J., Dunkley Jones, T., Anagnostou, E., Bijl, P. K., Cramwinckel, M. J., Cui, Y., et al. (2019). The DeepMIP contribution to PMIP4: Methodologies for selection, compilation and analysis of latest Paleocene and early Eocene climate proxy data, incorporating version 0.1 of the DeepMIP database. *Geoscientific Model Development*, *12*(7), 3149–3206. https://doi.org/10.5194/gmd-12-3149-2019

Holzer, M., & Primeau, F. W. (2010). Improved constraints on transit time distributions from argon 39: A maximum entropy approach. *Journal of Geophysical Research*, *115*(C12). https://doi.org/10.1029/2010JC006410

Hopmans, E. C., Schouten, S., & Sinninghe Damsté, J. S. (2016). The effect of improved chromatography on GDGT-based palaeoproxies. *Organic Geochemistry*, *93*, 1–6. https://doi.org/10.1016/j.orggeochem.2015.12.006

Huguet, C., Fietz, S., & Rosell-Melé, A. (2013). Global distribution patterns of hydroxy glycerol dialkyl glycerol tetraethers. *Organic Geochemistry*, *57*, 107–118. https://doi.org/10.1016/j.orggeochem.2013.01.010

Huguet, C., Hopmans, E. C., Febo-Ayala, W., Thompson, D. H., Sinninghe Damsté, J. S., & Schouten, S. (2006). An improved method to determine the absolute abundance of glycerol dibiphytanyl glycerol tetraether lipids. *Organic Geochemistry*, *37*(9), 1036–1041. https://doi.org/10.1016/j.orggeochem.2006.05.008

Huguet, C., Kim, J.-H., Sinninghe Damsté, J. S., & Schouten, S. (2006). Reconstruction of sea surface temperature variations in the Arabian Sea over the last 23 kyr using organic proxies (TEX_{86} and $U_{37}^{K'}$). *Paleoceanography*, *21*(3), PA3003. https://doi.org/10.1029/2005PA001215

Huguet, C., Schimmelmann, A., Thunell, R., Lourens, L. J., Sinninghe Damsté, J. S., & Schouten, S. (2007). A study of the TEX_{86} paleothermometer in the water column and sediments of the Santa Barbara Basin, California. *Paleoceanography*, *22*(3), PA3203. https://doi.org/10.1029/2006PA001310

Hurley, S. J., Elling, F. J., Könneke, M., Buchwald, C., Wankel, S. D., Santoro, A. E., et al. (2016). Influence of ammonia oxidation rate on thaumarchaeal lipid composition and the TEX_{86} temperature proxy. *Proceedings of the National Academy of Sciences*, *113*(28), 7762–7767. https://doi.org/10.1073/pnas.1518534113

Hurley, S. J., Lipp, J. S., Close, H. G., Hinrichs, K.-U., & Pearson, A. (2018). Distribution and export of isoprenoid tetraether lipids in suspended particulate matter from the water column of the western Atlantic Ocean. *Organic Geochemistry*, *116*, 90–102. https://doi.org/10.1016/j.orggeochem.2017.11.010

Incarbona, A., Martrat, B., Stefano, E. D., Grimalt, J. O., Pelosi, N., Patti, B., & Tranchida, G. (2010). Primary productivity variability on the Atlantic Iberian Margin over the last 70,000 years: Evidence from coccolithophores and fossil organic compounds. *Paleoceanography*, *25*(2). https://doi.org/10.1029/2008PA001709

Ingalls, A. E., Shah, S. R., Hansman, R. L., Aluwihare, L. I., Santos, G. M., Druffel, E. R. M., & Pearson, A. (2006). Quantifying archaeal community autotrophy in the mesopelagic ocean using natural radiocarbon. *Proceedings of the National Academy of Sciences*, *103*(17), 6442–6447. https://doi.org/10.1073/pnas.0510157103

Jenkins, W. J., Smethie, W. M., Boyle, E. A., & Cutter, G. A. (2015). Water mass analysis for the U.S. GEOTRACES (GA03) north Atlantic sections. *Deep Sea Research Part II: Topical Studies in Oceanography*, *116*, 6–20. https://doi.org/10.1016/j.dsr2.2014.11.018

Jia, G., Wang, X., Guo, W., & Dong, L. (2017). Seasonal distribution of archaeal lipids in surface water and its constraint on their sources and the TEX_{86} temperature proxy in sediments of the South China Sea. *Journal of Geophysical Research: Biogeosciences*, *122*(3), 592–606. https://doi.org/10.1002/2016JG003732

Johnsen, S. J., Dahl-Jensen, D., Dansgaard, W., & Gundestrup, N. (1995). Greenland palaeotemperatures derived from GRIP bore hole temperature and ice core isotope profiles. *Tellus B: Chemical and Physical Meteorology*, *47*(5), 624–629. https://doi.org/10.3402/tellusb.v47i5.16077

Jonas, A.-S., Schwark, L., & Bauersachs, T. (2017). Late Quaternary water temperature variations of the Northwest Pacific based on the lipid paleothermometers TEX_{86}^{H}, $U^{K'}_{37}$ and LDI. *Deep Sea Research Part I: Oceanographic Research Papers*, *125*, 81–93. https://doi.org/10.1016/j.dsr.2017.04.018

Jouzel, J., Masson-Delmotte, V., Cattani, O., Dreyfus, G., Falourd, S., Hoffmann, G., et al. (2007). Orbital and millennial Antarctic climate variability over the past 800,000 years. *Science*, *317*(5839), 793–796. https://doi.org/10.1126/science.1141038

Junium, C. K., Meyers, S. R., & Arthur, M. A. (2018). Nitrogen cycle dynamics in the late cretaceous greenhouse. *Earth and Planetary Science Letters*, *481*, 404–411. https://doi.org/10.1016/j.epsl.2017.10.006

Kaboth, S., Bahr, A., Reichart, G.-J., Jacobs, B., & Lourens, L. J. (2016). New insights into upper MOW variability over the last 150 kyr from IODP 339 Site U1386 in the Gulf of Cadiz. *Marine Geology*, *377*, 136–145. https://doi.org/10.1016/j.margeo.2015.08.014

Kageyama, M., Paul, A., Roche, D. M., van Meerbeeck, V. C. J. (2010). Modelling glacial climatic millennial-scale variability related to changes in the Atlantic meridional overturning circulation: A review. *Quaternary Science Reviews*, *29*(21), 2931–2956. https://doi.org/10.1016/j.quascirev.2010.05.029

Kang, S., Shin, K.-H., & Kim, J.-H. (2017). Occurrence and distribution of hydroxylated isoprenoid glycerol dialkyl glycerol tetraethers (OH-GDGTs) in the Han River system, South Korea. *Acta Geochimica*, *36*(3), 367–369. https://doi.org/10.1007/s11631-017-0165-3

Karner, M. B., DeLong, E. F., & Karl, D. M. (2001). Archaeal dominance in the mesopelagic zone of the Pacific Ocean. *Nature*, *409*(6819), 507–510. https://doi.org/10.1038/35054051

Kim, J.-H., Crosta, X., Michel, E., Schouten, S., Duprat, J. M., & Sinninghe Damsté, J. S. (2009). Impact of lateral transport on organic proxies in the Southern Ocean. *Quaternary Research*, *71*(2), 246–250. https://doi.org/10.1016/j.yqres.2008.10.005

Kim, J.-H., Romero, O. E., Lohmann, G., Donner, B., Laepple, T., Haam, E., & Sinninghe Damsté, J. S. (2012). Pronounced subsurface cooling of north Atlantic waters off northwest Africa during Dansgaard-Oeschger interstadials. *Earth and Planetary Science Letters*, *339–340*, 95–102. https://doi.org/10.1016/j.epsl.2012.05.018

Kim, J.-H., Schouten, S., Hopmans, E. C., Donner, B., & Sinninghe Damsté, J. S. (2008). Global sediment core-top calibration of the TEX_{86} paleothermometer in the ocean. *Geochimica et Cosmochimica Acta*, *72*(4), 1154–1173. https://doi.org/10.1016/j.gca.2007.12.010

Kim, J.-H., Schouten, S., Rodrigo-Gámiz, M., Rampen, S., Marino, G., Huguet, C., et al. (2015). Influence of deep-water derived isoprenoid tetraether lipids on the TEX_{86}^{H} paleothermometer in the Mediterranean Sea. *Geochimica et Cosmochimica Acta*, *150*, 125–141. https://doi.org/10.1016/j.gca.2014.11.017

Kim, J.-H., van der Meer, J., Schouten, S., Helmke, P., Willmott, V., Sangiorgi, F., et al. (2010). New indices and calibrations derived from the distribution of crenarchaeal isoprenoid tetraether lipids: Implications for past sea surface temperature reconstructions. *Geochimica et Cosmochimica Acta*, *74*(16), 4639–4654. https://doi.org/10.1016/j.gca.2010.05.027

Kim, J.-H., Villanueva, L., Zell, C., & Sinninghe Damsté, J. S. (2016). Biological source and provenance of deep-water derived isoprenoid tetraether lipids along the Portuguese continental margin. *Geochimica et Cosmochimica Acta*, *172*, 177–204. https://doi.org/10.1016/j.gca.2015.09.010

Kinder, T. H., & Parrilla, G. (1987). Yes, some of the Mediterranean outflow does come from great depth. *Journal of Geophysical Research*, *92*(C3), 2901–2906. https://doi.org/10.1029/JC092iC03p02901

Kindler, P., Guillevic, M., Baumgartner, M., Schwander, J., Landais, A., & Leuenberger, M. (2014). Temperature reconstruction from 10 to 120 kyr b2k from the NGRIP ice core. *Climate of the Past*, *10*(2), 887–902. https://doi.org/10.5194/cp-10-887-2014

Könneke, M., Bernhard, A. E., de la Torre, J. R., Walker, C. B., Waterbury, J. B., & Stahl, D. A. (2005). Isolation of an autotrophic ammonia-oxidizing marine archaeon. *Nature*, *437*(7058), 543–546. https://doi.org/10.1038/nature03911

Kotov, S., & Pälike, H. (2018). QAnalySeries—A cross-platform time series tuning and analysis tool. In AGU 2018 Fall Meeting, Washington DC. https://doi.org/10.1002/essoar.10500226.1

Kremer, A., Stein, R., Fahl, K., Ji, Z., Yang, Z., Wiers, S., et al. (2018). Changes in sea ice cover and ice sheet extent at the Yermak Plateau during the last 160 ka—Reconstructions from biomarker records. *Quaternary Science Reviews*, *182*, 93–108. https://doi.org/10.1016/j.quascirev.2017.12.016

Labeyrie, L. D. (1999). *CAMPAGNE INTERPOLE MD99–114/IMAGES V (PANGAEA documentation)*. Gif/Yvette cedex France: IPEV-Dept-Océanographique. Retrieved from https://epic.awi.de/id/eprint/34699/

Lattaud, J., Lo, L., Huang, J.-J., Chou, Y.-M., Gorbarenko, S. A., Sinninghe Damsté, J. S, et al. (2018). A comparison of late Quaternary organic proxy-based paleotemperature records of the central Sea of Okhotsk. *Paleoceanography and Paleoclimatology*, *33*(7), 732–744. https://doi.org/10.1029/2018PA003388

Lawrence, K. T., Pearson, A., Castañeda, I. S., Ladlow, C., Peterson, L. C., & Lawrence, C. E. (2020). Comparison of Late Neogene $U^{K'}_{37}$ and TEX_{86} paleotemperature records from the eastern equatorial Pacific at orbital resolution. *Paleoceanography and Paleoclimatology*, *35*(7), e2020PA003858. https://doi.org/10.1029/2020PA003858

Lee, K. E., Kim, J.-H., Wilke, I., Helmke, P., & Schouten, S. (2008). A study of the alkenone, TEX_{86}, and planktonic foraminifera in the Benguela Upwelling System: Implications for past sea surface temperature estimates. *Geochemistry, Geophysics, Geosystems*, *9*(10), Q10019. https://doi.org/10.1029/2008GC002056

Leider, A., Hinrichs, K.-U., Mollenhauer, G., & Versteegh, G. J. M. (2010). Core-top calibration of the lipid-based $U^{K'}_{37}$ and TEX_{86} temperature proxies on the southern Italian shelf (SW Adriatic Sea, Gulf of Taranto). *Earth and Planetary Science Letters*, *300*(1), 112–124. https://doi.org/10.1016/j.epsl.2010.09.042

Liu, R., Han, Z., Zhao, J., Zhang, H., Li, D., Ren, J., et al. (2020). Distribution and source of glycerol dialkyl glycerol tetraethers (GDGTs) and the applicability of GDGT-based temperature proxies in surface sediments of Prydz Bay, East Antarctica. *Polar Research*, *39*, 3557. https://doi.org/10.33265/polar.v39.3557

Liu, X.-L., Lipp, J. S., Simpson, J. H., Lin, Y.-S., Summons, R. E., & Hinrichs, K.-U. (2012). Mono- and dihydroxyl glycerol dibiphytanyl glycerol tetraethers in marine sediments: Identification of both core and intact polar lipid forms. *Geochimica et Cosmochimica Acta*, *89*, 102–115. https://doi.org/10.1016/j.gca.2012.04.053

Liu, Z., Otto-Bliesner, B. L., He, F., Brady, E. C., Tomas, R., Clark, P. U., et al. (2009). Transient simulation of last deglaciation with a new mechanism for Bølling-Allerød warming. *Science*, *325*(5938), 310–314. https://doi.org/10.1126/science.1171041

Llave, E., Schönfeld, J., Hernández-Molina, F. J., Mulder, T., Somoza, L., Díaz del Río, V., & Sánchez-Almazo, I. (2006). High-resolution stratigraphy of the Mediterranean outflow contourite system in the Gulf of Cadiz during the late Pleistocene: The impact of Heinrich events. *Marine Geology*, *227*(3), 241–262. https://doi.org/10.1016/j.margeo.2005.11.015

Locarnini, R. A., Mishonov, A. V., Baranova, O. K., Boyer, T. P., Zweng, M. M., Garcia, H. E., et al. (2019). World ocean atlas 2018, Volume 1: Temperature. In A. Mishonov (Ed.), *NOAA Atlas NESDIS 81* (p. 52). National Oceanographic Data Center. Retrieved from https://www.nodc.noaa.gov/OC5/indprod.html

Lopes dos Santos, R. A., Prange, M., Castañeda, I. S., Schefuß, E., Mulitza, S., Schulz, M., et al. (2010). Glacial-interglacial variability in Atlantic meridional overturning circulation and thermocline adjustments in the tropical north Atlantic. *Earth and Planetary Science Letters*, *300*(3), 407–414. https://doi.org/10.1016/j.epsl.2010.10.030

Lopes dos Santos, R. A., Spooner, M. I, Barrows, T. T., De Deckker, P., Sinninghe Damsté, J. S., & Schouten, S. (2013). Comparison of organic ($U_{37}^{K'}$, TEX_{86}^{H}, LDI) and faunal proxies (foraminiferal assemblages) for reconstruction of late Quaternary sea surface temperature variability from offshore southeastern Australia. *Paleoceanography*, *28*(3), 377–387. https://doi.org/10.1002/palo.20035

Louarn, E., & Morin, P. (2011). Antarctic intermediate water influence on Mediterranean Sea water outflow. *Deep Sea Research Part I: Oceanographic Research Papers*, *58*(9), 932–942. https://doi.org/10.1016/j.dsr.2011.05.009

Lü, X., Chen, J., Han, T., Yang, H., Wu, W., Ding, W., & Hinrichs, K.-U. (2019). Origin of hydroxyl GDGTs and regular isoprenoid GDGTs in suspended particulate matter of Yangtze River Estuary. *Organic Geochemistry*, *128*, 78–85. https://doi.org/10.1016/j.orggeochem.2018.12.010

Lü, X., Liu, X.-L., Elling, F. J., Yang, H., Xie, S., Song, J., et al. (2015). Hydroxylated isoprenoid GDGTs in Chinese coastal seas and their potential as a paleotemperature proxy for mid-to-low latitude marginal seas. *Organic Geochemistry*, *89–90*, 31–43. https://doi.org/10.1016/j.orggeochem.2015.10.004

Lü, X., Yang, H., Song, J., Versteegh, G. J. M., Li, X., Yuan, H., et al. (2014). Sources and distribution of isoprenoid glycerol dialkyl glycerol tetraethers (GDGTs) in sediments from the east coastal sea of China: Application of GDGT-based paleothermometry to a shallow marginal sea. *Organic Geochemistry*, *75*, 24–35. https://doi.org/10.1016/j.orggeochem.2014.06.007

Lynch-Stieglitz, J. (2017). The Atlantic meridional overturning circulation and abrupt climate change. *Annual Review of Marine Science*, *9*(1), 83–104. https://doi.org/10.1146/annurev-marine-010816-060415

Lynch-Stieglitz, J., Adkins, J. F., Curry, W. B., Dokken, T., Hall, I. R., Herguera, J. C., et al. (2007). Atlantic meridional overturning circulation during the last glacial maximum. *Science*, *316*(5821), 66–69. https://doi.org/10.1126/science.1137127

Ma, C., Coffinet, S., Lipp, J. S., Hinrichs, K.-U., & Zhang, C. (2020). Marine group II Euryarchaeota contribute to the archaeal lipid pool in northwestern Pacific Ocean surface waters. *Frontiers in Microbiology*, *11*, 1034. https://doi.org/10.3389/fmicb.2020.01034

Magill, C. R., Ausín, B., Wenk, P., McIntyre, C., Skinner, L., Martínez-García, A., et al. (2018). Transient hydrodynamic effects influence organic carbon signatures in marine sediments. *Nature Communications*, *9*, 4690. https://doi.org/10.1038/s41467-018-06973-w

Malevich, S. B., Vetter, L., & Tierney, J. E. (2019). Global core top calibration of $\delta^{18}O$ in planktic foraminifera to sea surface temperature. *Paleoceanography and Paleoclimatology*, *34*(8), 1292–1315. https://doi.org/10.1029/2019PA003576

Marcott, S. A., Clark, P. U., Padman, L., Klinkhammer, G. P., Springer, S. R., Liu, Z., et al. (2011). Ice-shelf collapse from subsurface warming as a trigger for Heinrich events. *Proceedings of the National Academy of Sciences*, *108*(33), 13415–13419. https://doi.org/10.1073/pnas.1104772108

Marlowe, I. T., Brassell, S. C., Eglinton, G., & Green, J. C. (1984). Long chain unsaturated ketones and esters in living algae and marine sediments. *Organic Geochemistry*, *6*, 135–141. https://doi.org/10.1016/0146-6380(84)90034-2

Martins, C. S., Hamann, M., & Fiúza, A. F. G. (2002). Surface circulation in the eastern north Atlantic, from drifters and altimetry. *Journal of Geophysical Research*, *107*(C12), 10–11–10–22. https://doi.org/10.1029/2000JC000345

Martins, M. V. A., Perretti, A. R., Salgueiro, E., Frontalini, F., Moreno, J., Soares, A. M., et al. (2015). Atlantic sea surface temperatures estimated from planktonic foraminifera off the Iberian Margin over the last 40 Ka BP. *Marine Geology*, *367*, 191–201. https://doi.org/10.1016/j.margeo.2015.06.001

Martrat, B., Grimalt, J. O., Shackleton, N. J., de Abreu, L., Hutterli, M. A., & Stocker, T. F. (2007). Four climate cycles of recurring deep and surface water destabilizations on the Iberian Margin. *Science*, *317*(5837), 502–507. https://doi.org/10.1126/science.1139994

Martrat, B., Jiménez-Amat, P., Zahn, R., & Grimalt, J. O. (2014). Similarities and dissimilarities between the last two deglaciations and interglaciations in the North Atlantic region. *Quaternary Science Reviews*, *99*, 122–134. https://doi.org/10.1016/j.quascirev.2014.06.016

Mazé, J. P., Arhan, M., & Mercier, H. (1997). Volume budget of the eastern boundary layer off the Iberian Peninsula. *Deep Sea Research Part I: Oceanographic Research Papers*, *44*(9), 1543–1574. https://doi.org/10.1016/S0967-0637(97)00038-1

McClymont, E. L., Ganeshram, R. S., Pichevin, L. E., Talbot, H. M., Dongen, B. E., van, Thunell, R. C., et al. (2012). Sea-surface temperature records of Termination 1 in the Gulf of California: Challenges for seasonal and interannual analogues of tropical Pacific climate change. *Paleoceanography*, *27*(2), PA2202. https://doi.org/10.1029/2011PA002226

Meyers, S. R. (2014). *Astrochron: An R package for astrochronology*. Retrieved from CRAN (Comprehensive R Archive Network). https://cran.r-project.org/package=astrochron

Mignot, J., Ganopolski, A., & Levermann, A. (2007). Atlantic subsurface temperatures: Response to a shutdown of the overturning circulation and consequences for its recovery. *Journal of Climate*, *20*(19), 4884–4898. https://doi.org/10.1175/JCLI4280.1

Mollenhauer, G., Basse, A., Kim, J.-H., Sinninghe Damsté, J. S., & Fischer, G. (2015). A four-year record of $U^{K'}_{37}$- and TEX_{86}-derived sea surface temperature estimates from sinking particles in the filamentous upwelling region off Cape Blanc, Mauritania. *Deep Sea Research Part I: Oceanographic Research Papers*, *97*, 67–79. https://doi.org/10.1016/j.dsr.2014.11.015

Mollenhauer, G., Eglinton, T. I., Hopmans, E. C., & Sinninghe Damsté, J. S. (2008). A radiocarbon-based assessment of the preservation characteristics of crenarchaeol and alkenones from continental margin sediments. *Organic Geochemistry*, *39*(8), 1039–1045. https://doi.org/10.1016/j.orggeochem.2008.02.006

Mollenhauer, G., Inthorn, M., Vogt, T., Zabel, M., Sinninghe Damsté, J. S., & Eglinton, T. I. (2007). Aging of marine organic matter during cross-shelf lateral transport in the Benguela upwelling system revealed by compound-specific radiocarbon dating. *Geochemistry, Geophysics, Geosystems*, *8*(9), Q09004. https://doi.org/10.1029/2007GC001603

Mollenhauer, G., McManus, J. F., Benthien, A., Müller, P. J., & Eglinton, T. I. (2006). Rapid lateral particle transport in the Argentine basin: Molecular ^{14}C and $^{230}Th_{xs}$ evidence. *Deep Sea Research Part I: Oceanographic Research Papers*, *53*(7), 1224–1243. https://doi.org/10.1016/j.dsr.2006.05.005

Montero-Serrano, J.-C., Frank, N., Colin, C., Wienberg, C., & Eisele, M. (2011). The climate influence on the mid-depth Northeast Atlantic gyres viewed by cold-water corals. *Geophysical Research Letters*, *38*(19). https://doi.org/10.1029/2011GL048733

Moseley, G. E., Spötl, C., Brandstätter, S., Erhardt, T., Luetscher, M., & Edwards, R. L. (2020). NALPS19: Sub-orbital-scale climate variability recorded in northern Alpine speleothems during the last glacial period. *Climate of the Past*, *16*(1), 29–50. https://doi.org/10.5194/cp-16-29-2020

Müller, P. J., Kirst, G., Ruhland, G., von Storch, I., & Rosell-Melé, A. (1998). Calibration of the alkenone paleotemperature index $U_{37}^{K'}$ based on core-tops from the eastern South Atlantic and the global ocean (60°N-60°S). *Geochimica et Cosmochimica Acta*, *62*(10), 1757–1772. https://doi.org/10.1016/S0016-7037(98)00097-0

Navarro, G., & Ruiz, J. (2006). Spatial and temporal variability of phytoplankton in the Gulf of Cádiz through remote sensing images. *Deep Sea Research Part II: Topical Studies in Oceanography*, *53*(11), 1241–1260. https://doi.org/10.1016/j.dsr2.2006.04.014

NEEM community members. (2013). Eemian interglacial reconstructed from a Greenland folded ice core. *Nature*, *493*(7433), 489–494. https://doi.org/10.1038/nature11789

NGRIP Members. (2004). High-resolution record of Northern Hemisphere climate extending into the last interglacial period. *Nature*, *431*(7005), 147–151. https://doi.org/10.1038/nature02805

Paillard, D., Labeyrie, L. D., & Yiou, P. (1996). Macintosh Program performs time-series analysis. *Eos, Transactions American Geophysical Union*, *77*(39), 379. https://doi.org/10.1029/96EO00259

Pailler, D., & Bard, E. (2002). High frequency palaeoceanographic changes during the past 140 000 yr recorded by the organic matter in sediments of the Iberian Margin. *Palaeogeography, Palaeoclimatology, Palaeoecology*, *181*(4), 431–452. https://doi.org/10.1016/S0031-0182(01)00444-8

Park, E., Hefter, J., Fischer, G., Iversen, M. H., Ramondenc, S., Nöthig, E.-M., & Mollenhauer, G. (2019). Seasonality of archaeal lipid flux and GDGT-based thermometry in sinking particles of high-latitude oceans: Fram Strait (79°N) and Antarctic Polar Front (50°S). *Biogeosciences*, *16*(11), 2247–2268. https://doi.org/10.5194/bg-16-2247-2019

Park, E., Hefter, J., Fischer, G., & Mollenhauer, G. (2018). TEX_{86} in sinking particles in three eastern Atlantic upwelling regimes. *Organic Geochemistry*, *124*, 151–163. https://doi.org/10.1016/j.orggeochem.2018.07.015

Park, Y.-H., Yamamoto, M., Nam, S.-I., Irino, T., Polyak, L., Harada, N., et al. (2014). Distribution, source and transportation of glycerol dialkyl glycerol tetraethers in surface sediments from the western Arctic Ocean and the northern Bering Sea. *Marine Chemistry*, *165*, 10–24. https://doi.org/10.1016/j.marchem.2014.07.001

Pedro, J. B., Jochum, M., Buizert, C., He, F., Barker, S., & Rasmussen, S. O. (2018). Beyond the bipolar seesaw: Toward a process understanding of interhemispheric coupling. *Quaternary Science Reviews*, *192*, 27–46. https://doi.org/10.1016/j.quascirev.2018.05.005

Pedrosa-Pàmies, R., Parinos, C., Sanchez-Vidal, A., Gogou, A., Calafat, A., Canals, M., et al. (2015). Composition and sources of sedimentary organic matter in the deep eastern Mediterranean Sea. *Biogeosciences*, *12*(24), 7379–7402. https://doi.org/10.5194/bg-12-7379-2015

Peliz, Á., Dubert, J., Haidvogel, D. B., & Cann, B. L. (2003). Generation and unstable evolution of a density-driven Eastern Poleward Current: The Iberian Poleward Current. *Journal of Geophysical Research*, *108*(C8). https://doi.org/10.1029/2002JC001443

Peliz, Á., Dubert, J., Santos, A. M. P., Oliveira, P. B., & Le Cann, B. (2005). Winter upper ocean circulation in the western Iberian basin—Fronts, eddies and poleward flows: An overview. *Deep Sea Research Part I: Oceanographic Research Papers*, *52*(4), 621–646. https://doi.org/10.1016/j.dsr.2004.11.005

Pérez, F. F., Castro, C. G., Álvarez–Salgado, X. A., & Ríos, A. F. (2001). Coupling between the Iberian basin—scale circulation and the Portugal boundary current system: A chemical study. *Deep Sea Research Part I: Oceanographic Research Papers*, *48*(6), 1519–1533. https://doi.org/10.1016/S0967-0637(00)00101-1

Pitcher, A., Wuchter, C., Siedenberg, K., Schouten, S., & Sinninghe Damsté, J. S. (2011). Crenarchaeol tracks winter blooms of ammonia-oxidizing *Thaumarchaeota* in the coastal North Sea. *Limnology & Oceanography*, *56*(6), 2308–2318. https://doi.org/10.4319/lo.2011.56.6.2308

Polik, C. A., Elling, F. J., & Pearson, A. (2018). Impacts of paleoecology on the TEX_{86} sea surface temperature proxy in the Pliocene-Pleistocene Mediterranean Sea. *Paleoceanography and Paleoclimatology*, *33*(12), 1472–1489. https://doi.org/10.1029/2018PA003494

Prahl, F. G., Collier, R. B., Dymond, J., Lyle, M., & Sparrow, M. A. (1993). A biomarker perspective on prymnesiophyte productivity in the northeast Pacific Ocean. *Deep Sea Research Part I: Oceanographic Research Papers*, *40*(10), 2061–2076. https://doi.org/10.1016/0967-0637(93)90045-5

Prahl, F. G., Muehlhausen, L. A., & Zahnle, D. L. (1988). Further evaluation of long-chain alkenones as indicators of paleoceanographic conditions. *Geochimica et Cosmochimica Acta*, *52*(9), 2303–2310. https://doi.org/10.1016/0016-7037(88)90132-9

Prahl, F. G., Pilskaln, C. H., & Sparrow, M. A. (2001). Seasonal record for alkenones in sedimentary particles from the Gulf of Maine. *Deep Sea Research Part I: Oceanographic Research Papers*, *48*(2), 515–528. https://doi.org/10.1016/S0967-0637(00)00057-1

Prahl, F. G., Popp, B. N., Karl, D. M., & Sparrow, M. A. (2005). Ecology and biogeochemistry of alkenone production at Station ALOHA. *Deep Sea Research Part I: Oceanographic Research Papers*, *52*(5), 699–719. https://doi.org/10.1016/j.dsr.2004.12.001

Prahl, F. G., Rontani, J.-F., Zabeti, N., Walinsky, S. E., & Sparrow, M. A. (2010). Systematic pattern in $U^{K'}_{37}$—temperature residuals for surface sediments from high latitude and other oceanographic settings. *Geochimica et Cosmochimica Acta*, *74*(1), 131–143. https://doi.org/10.1016/j.gca.2009.09.027

Prahl, F. G., Sparrow, M. A., & Wolfe, G. V. (2003). Physiological impacts on alkenone paleothermometry. *Paleoceanography*, *181025*(2). https://doi.org/10.1029/2002PA000803

Prahl, F. G., & Wakeham, S. G. (1987). Calibration of unsaturation patterns in long-chain ketone compositions for palaeotemperature assessment. *Nature*, *330*(6146), 367–369. https://doi.org/10.1038/330367a0

Qin, W., Carlson, L. T., Armbrust, E. V., Devol, A. H., Moffett, J. W., Stahl, D. A., & Ingalls, A. E. (2015). Confounding effects of oxygen and temperature on the TEX_{86} signature of marine *Thaumarchaeota Proceedings of the National Academy of Sciences*, *112*(35), 10979–10984. https://doi.org/10.1073/pnas.1501568112

R Core Team. (2020). *R: A Language and Environment for Statistical Computing*. R foundation for statistical computing. Retrieved from https://www.R-project.org

Rahmstorf, S. (2002). Ocean circulation and climate during the past 120,000 years. *Nature*, *419*(6903), 207–214. https://doi.org/10.1038/nature01090

Railsback, L. B., Gibbard, P. L., Head, M. J., Voarintsoa, N. R. G., & Toucanne, S. (2015). An optimized scheme of lettered marine isotope substages for the last 1.0 million years, and the climatostratigraphic nature of isotope stages and substages. *Quaternary Science Reviews*, *111*, 94–106. https://doi.org/10.1016/j.quascirev.2015.01.012

Rasmussen, T. L., & Thomsen, E. (2004). The role of the north Atlantic drift in the millennial timescale glacial climate fluctuations. *Palaeogeography, Palaeoclimatology, Palaeoecology*, *210*(1), 101–116. https://doi.org/10.1016/j.palaeo.2004.04.005

Relvas, P., Barton, E. D., Dubert, J., Oliveira, P. B., Peliz, Á., da Silva, J. C. B., & Santos, A. M. P. (2007). Physical oceanography of the western Iberia ecosystem: Latest views and challenges. *Progress in Oceanography*, *74*(2), 149–173. https://doi.org/10.1016/j.pocean.2007.04.021

Richey, J. N., & Tierney, J. E. (2016). GDGT and alkenone flux in the northern Gulf of Mexico: Implications for the TEX_{86} and $U^{K'}_{37}$ paleothermometers. *Paleoceanography*, *31*(12), 1547–1561. https://doi.org/10.1002/2016PA003032

Rontani, J.-F., Volkman, J. K., Prahl, F. G., & Wakeham, S. G. (2013). Biotic and abiotic degradation of alkenones and implications for TEX_{86} and $U^{K'}_{37}$ paleoproxy applications: A review. *Organic Geochemistry*, *59*, 95–113. https://doi.org/10.1016/j.orggeochem.2013.04.005

Rosell-Melé, A., Bard, E., Emeis, K.-C., Grimalt, J. O., Müller, P., Schneider, R., et al. (2001). Precision of the current methods to measure the alkenone proxy $U^{K'}_{37}$ and absolute alkenone abundance in sediments: Results of an interlaboratory comparison study. *Geochemistry, Geophysics, Geosystems*, *2*(7), 2000GC000141. https://doi.org/10.1029/2000GC000141

Rühlemann, C., & Butzin, M. (2006). Alkenone temperature anomalies in the Brazil-Malvinas Confluence area caused by lateral advection of suspended particulate material. *Geochemistry Geophysics, Geosystems*, *7*(10). https://doi.org/10.1029/2006GC001251

Salgueiro, E., Naughton, F., Voelker, A. H. L., de Abreu, L., Alberto, A., Rossignol, L., et al. (2014). Past circulation along the western Iberian margin: A time slice vision from the last glacial to the Holocene. *Quaternary Science Reviews*, *106*, 316–329. https://doi.org/10.1016/j.quascirev.2014.09.001

Salgueiro, E., Voelker, A. H. L., de Abreu, L., Abrantes, F., Meggers, H., & Wefer, G. (2010). Temperature and productivity changes off the western Iberian margin during the last 150 ky. *Quaternary Science Reviews*, *29*(5), 680–695. https://doi.org/10.1016/j.quascirev.2009.11.013

Sánchez, R. F., & Relvas, P. (2003). Spring-summer climatological circulation in the upper layer in the region of Cape St. Vincent, Southwest Portugal. *ICES Journal of Marine Science*, *60*(6), 1232–1250. https://doi.org/10.1016/S1054-3139(03)00137-1

Sanchi, L., Ménot, G., & Bard, E. (2013). An automated purification method for archaeal and bacterial tetraethers in soils and sediments. *Organic Geochemistry*, *54*, 83–90. https://doi.org/10.1016/j.orggeochem.2012.10.005

Saunders, P. M. (1987). Flow through discovery gap. *Journal of Physical Oceanography*, *17*(5), 631–643. https://doi.org/10.1175/1520-0485(1987)017<0631:FTDG>2.0.CO;2

Schmidt, M. W., Chang, P., Hertzberg, J. E., Them, T. R., Ji, L., & Otto-Bliesner, B. L. (2012). Impact of abrupt deglacial climate change on tropical Atlantic subsurface temperatures. *Proceedings of the National Academy of Sciences*, *109*(36), 14348–14352. https://doi.org/10.1073/pnas.1207806109

Schmittner, A., Saenko, O. A., & Weaver, A. J. (2003). Coupling of the hemispheres in observations and simulations of glacial climate change. *Quaternary Science Reviews*, *22*(5), 659–671. https://doi.org/10.1016/S0277-3791(02)00184-1

Schönfeld, J., & Zahn, R. (2000). Late glacial to Holocene history of the Mediterranean outflow. Evidence from benthic foraminiferal assemblages and stable isotopes at the Portuguese margin. *Palaeogeography, Palaeoclimatology, Palaeoecology*, *159*(1), 85–111. https://doi.org/10.1016/S0031-0182(00)00035-3

Schouten, S., Forster, A., Panoto, F. E., & Sinninghe Damsté, J. S. (2007). Toward calibration of the TEX_{86} palaeothermometer for tropical sea surface temperatures in ancient greenhouse worlds. *Organic Geochemistry*, *38*(9), 1537–1546. https://doi.org/10.1016/j.orggeochem.2007.05.014

Schouten, S., Hopmans, E. C., Forster, A., Breugelvan, Y., Kuypers, M. M. M., & Sinninghe Damsté, J. S. (2003). Extremely high sea-surface temperatures at low latitudes during the middle Cretaceous as revealed by archaeal membrane lipids. *Geology*, *31*(12), 1069–1072. https://doi.org/10.1130/G19876.1

Schouten, S., Hopmans, E. C., Rosell-Melé, A., Pearson, A., Adam, P., Bauersachs, T., et al. (2013). An interlaboratory study of TEX_{86} and BIT analysis of sediments, extracts, and standard mixtures. *Geochemistry, Geophysics, Geosystems*, *14*(12), 5263–5285. https://doi.org/10.1002/2013GC004904

Schouten, S., Hopmans, E. C., Schefuß, E., & Sinninghe Damsté, J. S. (2002). Distributional variations in marine crenarchaeotal membrane lipids: A new tool for reconstructing ancient sea water temperatures?. *Earth and Planetary Science Letters*, *204*(1–2), 265–274. https://doi.org/10.1016/S0012-821X(02)00979-2

Schouten, S., Hopmans, E. C., & Sinninghe Damsté, J. S. (2013). The organic geochemistry of glycerol dialkyl glycerol tetraether lipids: A review. *Organic Geochemistry*, *54*, 19–61. https://doi.org/10.1016/j.orggeochem.2012.09.006

Seki, O., Sakamoto, T., Sakai, S., Schouten, S., Hopmans, E. C., Sinninghe Damsté, J. S., et al. (2009). Large changes in seasonal sea ice distribution and productivity in the Sea of Okhotsk during the deglaciations. *Geochemistry, Geophysics, Geosystems*, *10*(10), Q10007. https://doi.org/10.1029/2009GC002613

Shackleton, N. J. (1967). Oxygen isotope analyses and Pleistocene temperatures re-assessed. *Nature*, *215*(5096), 15–17. https://doi.org/10.1038/215015a0

Shackleton, N. J., Chapman, M., Sánchez-Goñi, M. F., Pailler, D., & Lancelot, Y. (2002). The classic marine isotope substage 5e. *Quaternary Research*, *58*(1), 14–16. https://doi.org/10.1006/qres.2001.2312

Shackleton, N. J., Hall, M. A., & Vincent, E. (2000). Phase relationships between millennial-scale events 64,000–24,000 years ago. *Paleoceanography*, *15*(6), 565–569. https://doi.org/10.1029/2000PA000513

Shaffer, G., Olsen, S. M., & Bjerrum, C. J. (2004). Ocean subsurface warming as a mechanism for coupling Dansgaard-Oeschger climate cycles and ice-rafting events. *Geophysical Research Letters*, *31*(24). https://doi.org/10.1029/2004GL020968

Shah, S. R., Mollenhauer, G., Ohkouchi, N., Eglinton, T. I., & Pearson, A. (2008). Origins of archaeal tetraether lipids in sediments: Insights from radiocarbon analysis. *Geochimica et Cosmochimica Acta*, *72*(18), 4577–4594. https://doi.org/10.1016/j.gca.2008.06.021

Sicre, M.-A., Ternois, Y., Miquel, J.-C., & Marty, J.-C. (1999). Alkenones in the northwestern Mediterranean Sea: Interannual variability and vertical transfer. *Geophysical Research Letters*, *26*(12), 1735–1738. https://doi.org/10.1029/1999GL900353

Sikes, E. L., O'Leary, T., Nodder, S. D., & Volkman, J. K. (2005). Alkenone temperature records and biomarker flux at the subtropical front on the Chatham Rise, SW Pacific Ocean. *Deep Sea Research Part I: Oceanographic Research Papers*, *52*(5), 721–748. https://doi.org/10.1016/j.dsr.2004.12.003

Sikes, E. L., Volkman, J. K., Robertson, L. G., & Pichon, J.-J. (1997). Alkenones and alkenes in surface waters and sediments of the Southern Ocean: Implications for paleotemperature estimation in polar regions. *Geochimica et Cosmochimica Acta*, *61*(7), 1495–1505. https://doi.org/10.1016/S0016-7037(97)00017-3

Sinninghe Damsté, J. S., Rijpstra, W. I. C., Hopmans, E. C., Jung, M.-Y., Kim, J.-G., et al. (2012). Intact polar and core glycerol dibiphytanyl glycerol tetraether lipids of Group I.1a and I.1b *Thaumarchaeota* in soil. *Applied and Environmental Microbiology*, *78*(19), 6866–6874. https://doi.org/10.1128/AEM.01681-12

Sinninghe Damsté, J. S., Schouten, S., Hopmans, E. C., Duinvan, A. C. T., & Geenevasen, J. A. J. (2002). Crenarchaeol: The characteristic core glycerol dibiphytanyl glycerol tetraether membrane lipid of cosmopolitan pelagic crenarchaeota. *Journal of Lipid Research*, *43*(10), 1641–1651. https://doi.org/10.1194/jlr.M200148-JLR200

Smith, R. A., Castañeda, I. S., Groeneveld, J., De Vleeschouwer, D., Henderiks, J., Christensen, B. A., et al. (2020). Plio-Pleistocene Indonesian Throughflow variability drove eastern Indian Ocean sea surface temperatures. *Paleoceanography and Paleoclimatology*, *35*(10), e2020PA003872. https://doi.org/10.1029/2020PA003872

Sollai, M., Villanueva, L., Hopmans, E. C., Reichart, G.-J., & Sinninghe Damsté, J. S. (2019). A combined lipidomic and 16S rRNA gene amplicon sequencing approach reveals archaeal sources of intact polar lipids in the stratified Black Sea water column. *Geobiology*, *17*(1), 91–109. https://doi.org/10.1111/gbi.12316

Sonzogni, C., Bard, E., Rostek, F., Lafont, R., Rosell-Melé, A., & Eglinton, G. (1997). Core-top calibration of the alkenone index vs sea surface temperature in the Indian Ocean. *Deep Sea Research Part II: Topical Studies in Oceanography*, *44*(6), 1445–1460. https://doi.org/10.1016/S0967-0645(97)00010-6

Stenni, B., Masson-Delmotte, V., Selmo, E., Oerter, H., Meyer, H., Röthlisberger, R., et al. (2010). The deuterium excess records of EPICA Dome C and Dronning Maud land ice cores (East Antarctica). *Quaternary Science Reviews*, *29*(1), 146–159. https://doi.org/10.1016/j.quascirev.2009.10.009

Swingedouw, D., Mignot, J., Braconnot, P., Mosquet, E., Kageyama, M., & Alkama, R. (2009). Impact of freshwater release in the North Atlantic under different climate conditions in an OAGCM. *Journal of Climate*, *22*(23), 6377–6403. https://doi.org/10.1175/2009JCLI3028.1

Taylor, K. W. R., Huber, M., Hollis, C. J., Hernandez-Sanchez, M. T., & Pancost, R. D. (2013). Re-evaluating modern and Palaeogene GDGT distributions: Implications for SST reconstructions. *Global and Planetary Change*, *108*, 158–174. https://doi.org/10.1016/j.gloplacha.2013.06.011

Ternois, Y., Sicre, M.-A., Boireau, A., Conte, M. H., & Eglinton, G. (1997). Evaluation of long-chain alkenones as paleo-temperature indicators in the Mediterranean Sea. *Deep Sea Research Part I: Oceanographic Research Papers*, *44*(2), 271–286. https://doi.org/10.1016/S0967-0637(97)89915-3

Thomson, J., Nixon, S., Summerhayes, C. P., Rohling, E. J., Schönfeld, J., Zahn, R., et al. (2000). Enhanced productivity on the Iberian margin during glacial/interglacial transitions revealed by barium and diatoms. *Journal of the Geological Society*, *157*(3), 667–677. https://doi.org/10.1144/jgs.157.3.667

Thomson, J., Nixon, S., Summerhayes, C. P., Schönfeld, J., Zahn, R., & Grootes, P. (1999). Implications for sedimentation changes on the Iberian margin over the last two glacial/interglacial transitions from $(^{230}Th_{excess})_0$ systematics. *Earth and Planetary Science Letters*, *165*(3), 255–270. https://doi.org/10.1016/S0012-821X(98)00265-9

Thouveny, N., Moreno, E., Delanghe, D., Candon, L., Lancelot, Y., & Shackleton, N. J. (2000). Rock magnetic detection of distal ice-rafted debries: Clue for the identification of Heinrich layers on the Portuguese margin. *Earth and Planetary Science Letters*, *180*(1), 61–75. https://doi.org/10.1016/S0012-821X(00)00155-2

Tierney, J. E., & Tingley, M. P. (2014). A Bayesian, spatially-varying calibration model for the TEX_{86}. *Geochimica et Cosmochimica Acta*, *127*, 83–106. https://doi.org/10.1016/j.gca.2013.11.026

Tierney, J. E., & Tingley, M. P. (2015). A TEX_{86} surface sediment database and extended Bayesian calibration. *Scientific Data*, *2*, 150029. https://doi.org/10.1038/sdata.2015.29

Tierney, J. E., & Tingley, M. P. (2018). BAYSPLINE: A new calibration for the alkenone paleothermometer. *Paleoceanography and Paleoclimatology*, *33*(3), 281–301. https://doi.org/10.1002/2017PA003201

van Aken, H. M. (2000a). The hydrography of the mid-latitude northeast Atlantic Ocean: I: The deep water masses. *Deep Sea Research Part I: Oceanographic Research Papers*, *47*(5), 757–788. https://doi.org/10.1016/S0967-0637(99)00092-8

van Aken, H. M. (2000b). The hydrography of the mid-latitude northeast Atlantic Ocean: II: The intermediate water masses. *Deep Sea Research Part I: Oceanographic Research Papers*, *47*(5), 789–824. https://doi.org/10.1016/S0967-0637(99)00112-0

Veres, D., Bazin, L., Landais, A., Toyé Mahamadou Kele, H., Lemieux-Dudon, B., Parrenin, F., et al. (2013). The Antarctic ice core chronology (AICC2012): An optimized multi-parameter and multi-site dating approach for the last 120 thousand years. *Climate of the Past*, *9*(4), 1733–1748. https://doi.org/10.5194/cp-9-1733-2013

Versteegh, G. J. M., Riegman, R., de Leeuw, J. W., & Jansen, J. H. F. (2001). $FredU_{37}^{K'}$ values for *Isochrysis galbana* as a function of culture temperature, light intensity and nutrient concentrations. *Organic Geochemistry*, *32*(6), 785–794. https://doi.org/10.1016/S0146-6380(01)00041-9

Vettoretti, G., & Peltier, W. R. (2015). Interhemispheric air temperature phase relationships in the nonlinear Dansgaard-Oeschger oscillation. *Geophysical Research Letters*, *42*(4), 1180–1189. https://doi.org/10.1002/2014GL062898

Villanueva, L., Schouten, S., & Sinninghe Damsté, J. S. (2015). Depth-related distribution of a key gene of the tetraether lipid biosynthetic pathway in marine Thaumarchaeota. *Environmental Microbiology*, *17*(10), 3527–3539. https://doi.org/10.1111/1462-2920.12508

Voelker, A. H. L., & de Abreude, L. (2011). *A review of Abrupt climate change events in the northeastern Atlantic Ocean (Iberian Margin): Latitudinal, longitudinal, and vertical gradients*. In Abrupt climate change: Mechanisms, patterns, and impacts (pp. 15–37). American Geophysical Union (AGU). Retrieved from https://doi.org/10.1029/2010GM001021

Voelker, A. H. L., de Abreu, L., Schönfeld, J., Erlenkeuser, H., & Abrantes, F. (2009). Hydrographic conditions along the western Iberian margin during marine isotope stage 2. *Geochemistry Geophysics, Geosystems*, *10*(12). https://doi.org/10.1029/2009GC002605

Voelker, A. H. L., Lebreiro, S. M., Schönfeld, J., Cacho, I., Erlenkeuser, H., & Abrantes, F. (2006). Mediterranean outflow strengthening during northern hemisphere coolings: A salt source for the glacial Atlantic?. *Earth and Planetary Science Letters*, *245*(1), 39–55. https://doi.org/10.1016/j.epsl.2006.03.014

Volkman, J. K., Barrerr, S. M., Blackburn, S. I., & Sikes, E. L. (1995). Alkenones in *Gephyrocapsa oceanica*: Implications for studies of paleoclimate. *Geochimica et Cosmochimica Acta*, *59*(3), 513–520. https://doi.org/10.1016/0016-7037(95)00325-T

Volkman, J. K., Eglinton, G., Corner, E. D. S., & Forsberg, T. E. V. (1980). Long-chain alkenes and alkenones in the marine coccolithophorid *Emiliania huxleyi*. *Phytochemistry*, *19*(12), 2619–2622. https://doi.org/10.1016/S0031-9422(00)83930-8

Vorrath, M.-E., Müller, J., Rebolledo, L., Cárdenas, P., Shi, X., Esper, O., et al. (2020). Sea ice dynamics in the Bransfield Strait, Antarctic Peninsula, during the past 240 years: A multi-proxy intercomparison study. *Climate of the Past*, *16*(6), 2459–2483. https://doi.org/10.5194/cp-16-2459-2020

Wang, Y., Li, D.-W., Sachs, J. P., Hu, J., Cao, Y., Li, L., et al. (2019). Vertical distribution of isoprenoid GDGTs in suspended particles from the east China Sea shelf and implications for sedimentary TEX_{86}^{H} records. *Organic Geochemistry*, *136*, 103895. https://doi.org/10.1016/j.orggeochem.2019.07.004

Wei, B., Jia, G., Hefter, J., Kang, M., Park, E., Wang, S., & Mollenhauer, G. (2020). Comparison of the $U_{37}^{K'}$, LDI, $TEXH_{86}$, and RI-OH temperature proxies in sediments from the northern shelf of the South China Sea. *Biogeosciences*, *17*(17), 4489–4508. https://doi.org/10.5194/bg-17-4489-2020

Weijers, J. W. H., Lim, K. L. H., Aquilina, A., Sinninghe Damsté, J. S., & Pancost, R. D. (2011). Biogeochemical controls on glycerol dialkyl glycerol tetraether lipid distributions in sediments characterized by diffusive methane flux. *Geochemistry, Geophysics, Geosystems*, *12*(10), Q10010. https://doi.org/10.1029/2011GC003724

Weijers, J. W. H., Schouten, S., Spaargaren, O. C., & Sinninghe Damsté, J. S. (2006). Occurrence and distribution of tetraether membrane lipids in soils: Implications for the use of the TEX_{86} proxy and the BIT index. *Organic Geochemistry*, *37*(12), 1680–1693. https://doi.org/10.1016/j.orggeochem.2006.07.018

Wolff, E. W., Chappellaz, J., Blunier, T., Rasmussen, S. O., & Svensson, A. (2010). Millennial-scale variability during the last glacial: the ice core record. *Quaternary Science Reviews*, *29*(21), 2828–2838. https://doi.org/10.1016/j.quascirev.2009.10.013

Woodward, W. A. (2016). *Applied time series analysis*. Retrieved from CRAN (Comprehensive R Archive Network). Retrieved from https://CRAN.R-project.org/package=tswge

Woodward, W. A., Gray, H. L., & Elliott, A. C. (2017). *Applied time series analysis with R* (2nd ed.). Chapman & Hall/CRC. Retrieved from https://www.routledge.com/Applied-Time-Series-Analysis-with-R-Second-Edition/Woodward-Gray-Elliott/p/book/9781498734226

Wu, J., Stein, R., Fahl, K., Syring, N., Nam, S.-I., Hefter, J., et al. (2020). Deglacial to Holocene variability in surface water characteristics and major floods in the Beaufort Sea. *Communications Earth & Environment*, *1*, 27. https://doi.org/10.1038/s43247-020-00028-z

Wu, Y., Shi, X., Gong, X., Jian, Z., Zou, J., Liu, Y., et al. (2020). Evolution of the upper ocean stratification in the Japan Sea since the last glacial. *Geophysical Research Letters*, *47*(16), e2020GL088255. https://doi.org/10.1029/2020GL088255

Wuchter, C., Abbas, B., Coolen, M. J. L., Herfort, L., Bleijswijk, J., van, Timmers, P., et al. (2006). Archaeal nitrification in the ocean. *Proceedings of the National Academy of Sciences*, *103*(33), 12317–12322. https://doi.org/10.1073/pnas.0600756103

Wuchter, C., Schouten, S., Coolen, M. J. L., & Sinninghe Damsté, J. S. (2004). Temperature-dependent variation in the distribution of tetraether membrane lipids of marine Crenarchaeota: Implications for TEX86 paleothermometry. *Paleoceanography*, *19*(4), PA4028. https://doi.org/10.1029/2004PA001041

Xie, S., Liu, X.-L., Schubotz, F., Wakeham, S. G., & Hinrichs, K.-U. (2014). Distribution of glycerol ether lipids in the oxygen minimum zone of the eastern tropical North Pacific Ocean. *Organic Geochemistry*, *71*, 60–71. https://doi.org/10.1016/j.orggeochem.2014.04.006

Xing, L., Sachs, J. P., Gao, W., Tao, S., Zhao, X., Li, L., et al. (2015). TEX_{86} paleothermometer as an indication of bottom water temperature in the Yellow Sea. *Organic Geochemistry*, *86*, 19–31. https://doi.org/10.1016/j.orggeochem.2015.05.007

Xu, Y., Wu, W., Xiao, W., Ge, H., Wei, Y., Yin, X., et al. (2020). Intact ether lipids in trench sediments related to archaeal community and environmental conditions in the deepest ocean. *Journal of Geophysical Research: Biogeosciences*, *125*(7), e2019JG005431. https://doi.org/10.1029/2019JG005431

Yang, H., Xiao, W., Słowakiewicz, M., Ding, W., Ayari, A., Dang, X., & Pei, H. (2019). Depth-dependent variation of archaeal ether lipids along soil and peat profiles from southern China: Implications for the use of isoprenoidal GDGTs as environmental tracers. *Organic Geochemistry*, *128*, 42–56. https://doi.org/10.1016/j.orggeochem.2018.12.009

Zahn, R., Sarnthein, M., & Erlenkeuser, H. (1987). Benthic isotope evidence for changes of the Mediterranean outflow during the Late Quaternary. *Paleoceanography*, *2*(6), 543–559. https://doi.org/10.1029/PA002i006p00543

Zeng, Z., Liu, X.-L., Farley, K. R., Wei, J. H., Metcalf, W. W., Summons, R. E., & Welander, P. V. (2019). GDGT cyclization proteins identify the dominant archaeal sources of tetraether lipids in the ocean. *Proceedings of the National Academy of Sciences*, *116*(45), 22505–22511. https://doi.org/10.1073/pnas.1909306116

Zhang, J., Bai, Y., Xu, S., Lei, F., & Jia, G. (2013). Alkenone and tetraether lipids reflect different seasonal seawater temperatures in the coastal northern South China Sea. *Organic Geochemistry*, *58*, 115–120. https://doi.org/10.1016/j.orggeochem.2013.02.012

Zhang, X., & Prange, M. (2020). Stability of the Atlantic overturning circulation under intermediate (MIS3) and full glacial (LGM) conditions and its relationship with Dansgaard-Oeschger climate variability. *Quaternary Science Reviews*, *242*, 106443. https://doi.org/10.1016/j.quascirev.2020.106443

Zhang, Y. G., & Liu, X. (2018). Export depth of the TEX_{86} signal. *Paleoceanography and Paleoclimatology*, *33*(7), 666–671. https://doi.org/10.1029/2018PA003337

Zhang, Y. G., Zhang, C. L., Liu, X.-L., Li, L., Hinrichs, K.-U., & Noakes, J. E. (2011). Methane Index: A tetraether archaeal lipid biomarker indicator for detecting the instability of marine gas hydrates. *Earth and Planetary Science Letters*, *307*(3–4), 525–534. https://doi.org/10.1016/j.epsl.2011.05.031

Zhu, C., Wakeham, S. G., Elling, F. J., Basse, A., Mollenhauer, G., Versteegh, G. J. M., et al. (2016). Stratification of archaeal membrane lipids in the ocean and implications for adaptation and chemotaxonomy of planktonic archaea. *Environmental Microbiology*, *18*(12), 4324–4336. https://doi.org/10.1111/1462-2920.13289